Modeling, Analysis and Control of Underwater Vehicle SROV

Olle Ferling

LUND
UNIVERSITY

Department of Automatic Control

MSc Thesis
TFRT-6049
ISSN 0280-5316

Department of Automatic Control
Lund University
Box 118
SE-221 00 LUND
Sweden

Printed in Sweden by Tryckeriet i E-huset
Lund 2018

Abstract

A new type of Remotely Operated Vehicle (ROV) has been designed by Marin Mätteknik (MMT) in cooperation with Reach Subsea and Kystdesign AS; the Surveyor ROV. Although MMT is successfully using the SROV in day-to-day operations, no mathematical model describing the system has previously been derived. In this thesis project, a mathematical model describing the SROV is developed through system identification techniques. Experiments to facilitate parameter estimation of the model are designed and consequently performed. The gathered data sets are investigated to determine how well they are suited for parameter estimation. Estimation of the continuous-time model parameters are carried out using a Kalman filter running on the input-output data obtained through the experiments. Comparisons between this method and results obtained through a subspace-based identification Matlab method are performed. Model validation is carried out using numerous performance measures. The thesis has shown that a coupled LPV model may be a feasible approach to the modeling problem, and also makes suggestions that could possibly improve on the results.

As an alternative to the current control system, simulations of closed-loop responses of the identified system model using a Model Predictive Control (MPC) structure are undertaken and presented. The simulations show that good performance is achievable using the MPC algorithm. Noticeably, the current control system has difficulties attenuating deviations from angular velocity set points. The MPC scheme has been shown to effectively suppress such control errors in simulations.

Acknowledgements

Throughout this thesis project, I have received help from my advisors. I would first of all like do direct my sincerest thanks to professor Rolf Johansson, who has provided me with invaluable guidance and input on all parts of the research project.

I would also like to thank Jonas Andersson, MMT, for all his help with the technical aspects of the SROV. I am also grateful that he suggested the thesis subject to me.

Contents

1

Introduction

A Remotely Operated Vehicle (ROV) is a class of subsea vehicles designed to carry out different tasks, such as construction or inspection work. Previously, ROVs have been designed with a focus on station keeping to allow for construction work. Inspection has been carried out using the same type of ROV. Although this approach is possible, it is far from optimal in a time consumption sense.

MMT has, in cooperation with Reach Subsea and Kystdesign AS, developed a new type of ROV. The new model is called Surveyor ROV (SROV). An image of the SROV can be seen in Fig. 1.1. The new model differs from the previous standard in a number of ways. Most prominently, the SROV is used for survey work only. Typically, the SROV is used for surveying cable routes. This task is usually carried out at forward velocities that are large compared to lateral and vertical velocities. The physical design of the SROV differs from that of other ROVs. It is more streamlined than common ROVs, which allows for larger operational velocities. The SROV is about 5 m long, 2 m wide, and 1.4 m high. The weight of the vehicle is about 5 metric tons. The actuation of the SROV is performed using 9 hydraulic thrusters, powered by a hydraulic power unit (HPU) capable of supplying 200 HP. Using the thrusters, it is possible to actuate forward, lateral and vertical velocity, as well as roll, pitch, and yaw angular velocity. The thruster configuration of the SROV can be seen in Fig. 1.2. All SROV subsea activities are undertaken using a surface vessel, from which launch, recovery, and operation is performed. Communication and power transmission to the SROV is performed through a tether, which is connected to the vessel. Numerous sensors are fitted to the SROV. These include (but are not limited to) Inertial Navigation Systems (INS), multi-beam echo-sounders, HD cameras, light rigs, sub-bottom profilers and sound velocity profilers. Of particular interest to this thesis research are the INS units, as these will provide measurements of the SROV velocities, positions and orientations. The accuracies of the primary INS system used on-board the SROV are given in table 1.1. A special software running on a computer will also make it possible to record the control actions put out to the SROV.

The current control system is having some issues with deviations from set-points (typically zero rad/s) in angular velocities. As can be seen in Fig. 1.3, the control

Table 1.1 INS accuracies as reported by the INS data sheet.

Parameter	Accuracy
Forward velocity	$5 \cdot 10^{-3}$m/s
Lateral velocity	$5 \cdot 10^{-3}$m/s
Vertical velocity	10^{-3}m/s
Roll velocity	10^{-2}deg/s
Pitch velocity	10^{-2}deg/s
Yaw velocity	10^{-1}secant latitude / s
Roll	10^{-2}deg
Pitch	10^{-2}deg
Heading	10^{-1}secant latitude

Figure 1.1 Photography of the SROV used for the trials on Stril Explorer.

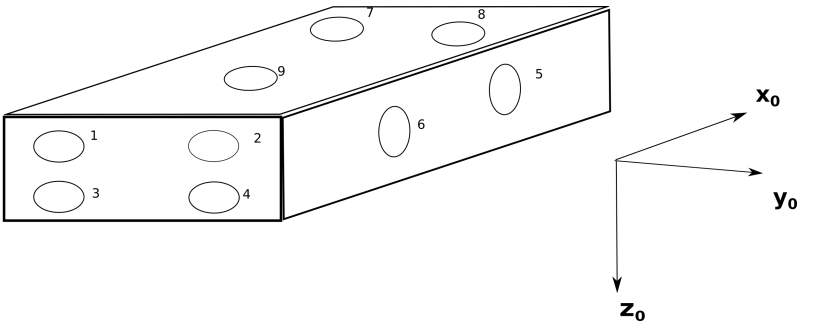

Figure 1.2 The thruster configuration of the SROV used in the trials. As can be seen in the sketch, nine thrusters are available and located according to the figure. There are four thrusters in the aft, two lateral thrusters, and three thrusters in the vertical plane of the SROV.

system is unable to remove oscillations in the angular velocity states. This is something that is not desired by MMT, as such oscillations affect survey data quality in a negative way.

Although the SROV is successfully being used in the day-to-day operations of MMT, no mathematical model describing the system has been developed. The control system of the SROV is based on older ROV standards. Many approaches to the problem of controlling underwater vehicles have been evaluated in the past. In [Fossen, 1994], many methods are described. Advantages and shortcomings of linearization techniques and non-linear controllers are discussed. In [Sangrok et al., 2015], a back-stepping strategy is used to control an underwater robot with tilting thrusters in simulations. Adaptive control schemes have been shown to work on a small-scale ROV in [Hayatolgheibi and Mazinan, 2017]. H-infinity control has been applied to an Autonomous Underwater Vehicle (AUV), as described in Feng and Allen [2010].

1.1 Goal

The goal of this thesis project is to develop a mathematical model suitable to describe the SROV. Further on, a model-based control system is to be identified and shown to work in simulations. The controller should ultimately be able to follow reference changes in linear velocities, while deviations from angular velocities (especially in yaw) should be attenuated. To facilitate the modeling procedure, experiments will be carried out on the SROV. The experiments have to be designed such that consistent parameter estimates can be made.

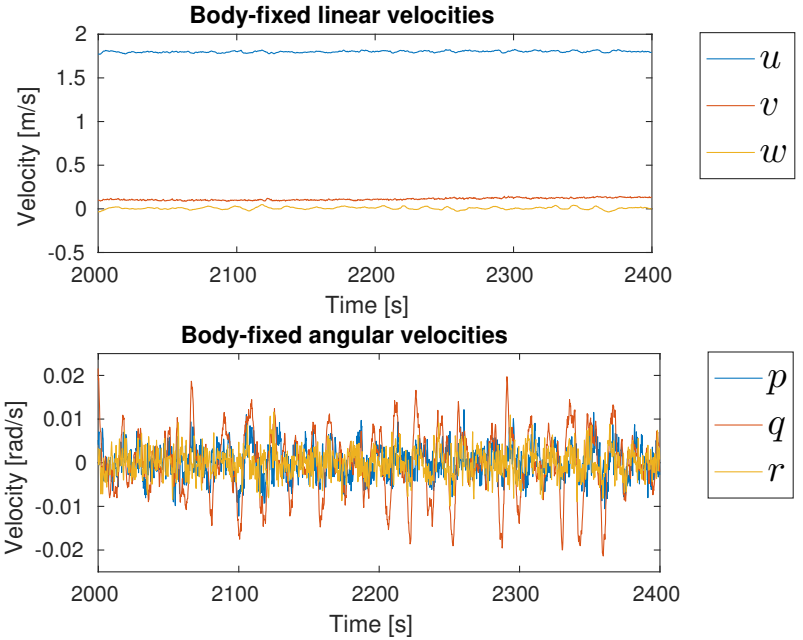

Figure 1.3 System velocities acquired during normal operations. Oscillations are present in the angular velocity states.

1.2 Reference Frames

It will be convenient to use two different coordinate systems to describe the dynamics of the SROV [Fossen, 1994]. One coordinate system will be inertial and used to describe the position and orientation of the SROV. Six states are needed to fully describe an object in the inertial reference frame; three describe position and three describe orientation. The states expressed in the inertial reference frame will be denoted η, and we have that

$$\eta = (x, y, z, \phi, \theta, \psi)^T \tag{1.1}$$

where the first three coordinates describe the position of an object, and the last three the rotations around the coordinate axes. In the context of this report, ϕ is the roll and describes rotation around the x-axis, θ is the roll and describes rotation around the y-axis, and ψ describes the rotation around the z-axis. It is customary to define the coordinate system as a right-handed Cartesian coordinate system, with z pointing downwards (towards the center of the earth).

The second coordinate system will be fixed to the SROV itself. The body-fixed reference frame is used to describe the speeds and angular velocities of the SROV. By choosing the origin of the body-fixed reference at the Center Of Gravity (COG)

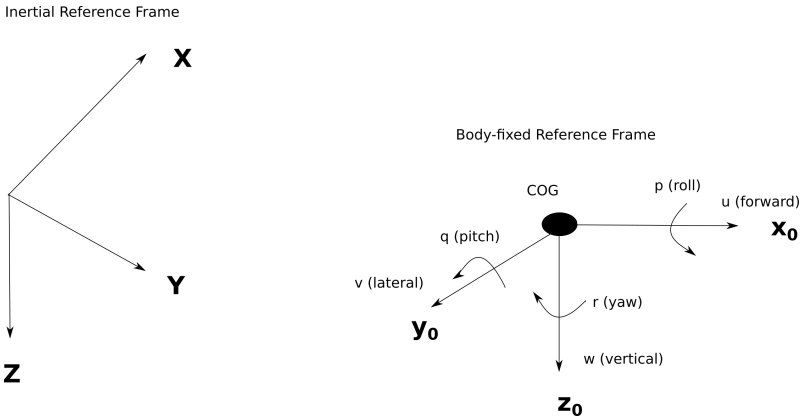

Figure 1.4 The two different reference frames used in this project. Transformation between the two coordinate systems may be performed using the rotation matrices J_1 and J_2.

of the SROV, symmetries can be exploited to get a simpler model expression [Fossen, 1994]. The body-fixed reference frame is denoted ν, and the states describing the body-fixed velocities is given by

$$\nu = (u, v, w, p, q, r)^T \tag{1.2}$$

where the first three entries describe linear velocities and the last three entries give the angular velocities of the object, expressed in the body-fixed reference frame. A depiction of the different reference frames may be seen in Fig. 1.4.

To be useful for modeling purposes, it must be possible to move between the two coordinate systems. This can be done [Fossen, 1994] by using the fact that

$$\begin{pmatrix} \dot{\eta}_1 \\ \dot{\eta}_2 \end{pmatrix} = \begin{pmatrix} J_1(\eta_2) & 0_{3\times 3} \\ 0_{3\times 3} & J_2(\eta_2) \end{pmatrix} \begin{pmatrix} \nu_1 \\ \nu_2 \end{pmatrix}$$

where J_1 and J_2 are rotation matrices given by

$$J_1(\eta_2) = \begin{pmatrix} c_\psi c_\theta & -s_\psi c_\phi + c_\psi s_\theta s_\phi & s_\psi s_\phi + c_\psi c_\phi s_\theta \\ s_\psi c_\theta & c_\psi c_\phi + s_\phi s_\theta s_\psi & -c_\psi s_\phi + s_\theta c_\phi s_\psi \\ -s_\theta & s_\phi c_\theta & c_\theta c_\phi \end{pmatrix}$$

and

$$J_2(\eta_2) = \begin{pmatrix} 1 & s_\phi t_\theta & c_\phi t_\theta \\ 0 & c_\phi & -s_\phi \\ 0 & s_\phi / c_\theta & c_\phi / c_\theta \end{pmatrix}$$

Here, $s.$ denotes $\sin(\cdot)$, $c.$ denotes $\cos(\cdot)$, and $t.$ denotes $\tan(\cdot)$. This representation of the rotation matrices is based on Euler angles, and exhibits singularities for $\theta =$

± 90 deg. This is not considered an issue in this project, as the SROV is usually stabilized around $\theta = 0$ rad, and should never operate close to the singularity.

1.3 System Identification

Modeling

In order to accurately describe the properties of any plant, it is necessary to have a mathematical framework describing the dynamics of the system. Typically, a set of differential equations are used to model continuous-time systems, and difference equations are used for discrete-time systems [Ljung, 1987]. The structure of the model can be derived in many different ways. One way to do it, is to use only theoretical arguments. Model parameters are calculated based purely on theoretical data. This approach is called *white box models* and is often insufficient due to the idealizations that have to be made in many physical equations.

Another way to build models is to only consider relations in input-output data. The identification is then concerned with finding proper model orders and parametric values that relate the inputs to the outputs. This approach is referred to as *black box modeling*. An obvious drawback with this approach is that physical information that may be present, can not be included in the identification process. By mixing theoretical arguments, and the use of input-output data in the identification process, a third approach is obtained, called *gray box modeling*. By using a gray box approach, theoretical information and derivations may be used to obtain a model of the process. This model may have parametric values that can be found through estimation techniques. Different estimation techniques are described in this section.

The ultimate goal of a mathematical model is to describe the evolution of the states being modeled. In other words, we want to find a model that can predict future states of the process as accurately as possible [Ljung, 1987]. Once a model that can feasibly well describe the physical process is obtained, it is possible to find model-based controller structures such as the Model Predictive Control (MPC) [Johansson, 2015] algorithm. It is also possible to run simulations, and thus minimize the time needed in field running costly experiments on the real process.

A lot of work has been done in the modeling of underwater vehicles. Fossen [1994] suggested a model of the dynamics that resembles that of a robotic system [Johansson, 2017]. The proposed model is

$$M\dot{\nu} + (C(\nu) + D(\nu))\nu + g(\eta) = \tau \tag{1.3}$$

This model is quite general as it allows for cross-coupling, non-linearities and is time-varying (state dependent). The different matrices in Eq. (1.3) describe different physical representations. M is describing the *added mass* of the system. As mentioned in Sec. 1.2, the structure of M depends on different design choices. If the process being modeled has three symmetry planes, it can be shown that M is positive definite and diagonal.

$C(\nu)$ is a matrix describing the Coriolis effect and can be shown to be skew symmetric (i.e., $C^T(\nu) = -C(\nu)$).

$D(\nu)$ describes the damping effects due to the speed of the ROV. This matrix is state dependent, as the damping effect is larger for larger speeds through water. As discussed in [Fossen, 1994], $D(\nu)$ may be highly non-linear and contain coupling terms, and can thus be hard to identify. However, a rough approximation is that $D(\nu)$ is diagonal and contains only linear and quadratic terms.

The term $g(\eta)$ is a vector describing the restoring forces and moments of the system. The entries of $g(\eta)$ depend on several parameters, and in its most general form looks like

$$g(\eta) = \begin{pmatrix} (W-B)s_\theta \\ -(W-B)c_\theta s_\phi \\ -(W-B)c_\theta c_\phi \\ -(y_G W - y_B B)c_\theta c_\phi + (z_G W - z_B B)c_\theta s_\phi \\ (z_G W - z_B B)s_\theta + (x_G W - x_B B)c_\theta c_\phi \\ -(x_G W - x_B B)c_\theta s_\phi - (y_G W - y_B B)s_\theta \end{pmatrix} \tag{1.4}$$

where W describes the weight of the system, and B denotes the buoyancy forces. $(z_G W - z_B B)$ is a term where z_G denotes the z-coordinate of the (COG), and where z_B is the z-coordinate of the center of buoyancy (COB) (all coordinates expressed in the body-fixed reference frame). As described in Sec. 1.2, the origin of the body-fixed reference frame may be arbitrarily placed. A common choice is to place the origin of the body-fixed reference frame at the COG. Drawings and a discussion with the mechanical engineer of the SROV manufacturer, suggest that the COB is located in $COB = (0, 0, z_B)$ with $z_B < 0$. The term $g(\eta)$ thus simplifies to

$$g(\eta) = \begin{pmatrix} (W-B)s_\theta \\ -(W-B)c_\theta s_\phi \\ -(W-B)c_\theta c_\phi \\ (z_G W - z_B B)c_\theta s_\phi \\ (z_G W - z_B B)s_\theta \\ 0 \end{pmatrix} \tag{1.5}$$

As discussed in Sec. 1.5, the tether is affecting the dynamics of the SROV. Using the assumption that the effect of the tether may be modeled as additive, $g(\eta)$ may be augmented to include the torque τ_θ exerted by the tether as

$$g(\eta) = \begin{pmatrix} (W-B)s_\theta \\ -(W-B)c_\theta s_\phi \\ -(W-B)c_\theta c_\phi \\ (z_G W - z_B B)c_\theta s_\phi \\ (z_G W - z_B B)s_\theta + \tau_\theta \\ 0 \end{pmatrix} \tag{1.6}$$

The term τ is a vector describing the exogenous input in each degree of freedom that may be used to affect the system. Since the reference frame has six coordinates, it holds that $\tau \in \mathbb{R}^{6\times 1}$. The SROV has nine thrusters to generate an input u_c. A thruster map T is needed to move from the force generated by each thruster to the total thrust in each degree of freedom:

$$T:\ \mathbb{R}^{9\times 1} \rightarrow \mathbb{R}^{6\times 1}\ : \tau = uT \tag{1.7}$$

T should take into consideration how different thrusters may be used to actuate different degrees of freedom. The thruster map T must generally be estimated in some way. However, the control system logger software records τ, meaning there is no need to estimate it explicitly. A static stability and maneuverability analysis based on the thruster configuration in Fig. 1.2 and the dimensions of the SROV, gave similar values of τ as the ones recorded by the logger software.

LPV Models

ROVs are highly non-linear processes [Fossen, 1994]. Identification of a non-linear process is difficult, and an approach often used to handle non-linear plants is to parameterize the model based on one or more of its states. This technique is called Linear Parameter-Varying (LPV) modeling, and has been successfully used in efforts to model an Autonomous Underwater Vehicle (AUV) [You et al., 2016]. As drag coefficients and Coriolis effects change with the speed through water, it is reasonable that the parametrization is scheduled on the SROV forward speed. This is motivated by the main operation mode of the SROV, which is following a predefined trajectory with $u > v,\ u > w$. By using an LPV model scheduled on forward speed, where the local model used is the one described in Eq. (1.3), one obtains

$$M_x\dot{\nu} + (C_x(\nu) + D_x(\nu))\nu + g_x(\eta) = \tau \tag{1.8}$$

where x is the scheduling variable (the forward speed). For instance, if the model is to cover $u \in [1,2]$, one way to choose the grid is as $x = (1, 1.5, 2)$. For each of the scheduling points in x, one set of parameter values has to be estimated. This implies that one set of experiments has to be carried out for each of the scheduling points, in order to generate the input-output data needed for the parameter estimation. When the LPV model is used for predictions of future system states, one first has to pick a model from the LPV set corresponding to the current scheduling state, after which predictions can be performed. If the system at hand is highly non-linear, one may choose to make the scheduling grid finer, such that the linear approximation has to cover a smaller span of the scheduling state. The down-side of making the grid too fine, is that many experiments have to be carried out for parameter estimation purposes. This takes time and costs money.

Continuous-Time Identification

Many systems operating in the real world are of a continuous-time nature. However, many of the system identification techniques are focused on discrete-time systems.

There are many advantages to be gained if a continuous-time system is modeled using a continuous-time system identification approach. In [Rao and Unbehauen, 2006], which is a survey of the field of continuous-time system identification, some of the advantages are discussed. A continuous-time model may have a physical interpretation, which would inevitably be lost if a discrete-time model is identified. Further on, issues regarding the discretization process are discussed. In order to estimate the parameters of a continuous-time model, there are many available methods. One is through the use of "state-variable filters". The method is discussed in [Rao and Unbehauen, 2006] and [Johansson, 2017]. As an alternative, [Johansson, 1994] suggests a model transformation of the form

$$\lambda(s) = \frac{1}{1+sT},\ T > 0 \tag{1.9}$$

By filtering all signals through this filter, an input-output model may be designed. This takes the form

$$y(t) = -\alpha_1[\lambda y](t) - \cdots - \alpha_n[\lambda^n y](t) + \beta_1[\lambda u](t) + \cdots + \beta_m[\lambda^m u](t) \tag{1.10}$$

where $[\lambda\cdot]$ denotes a signal filtered through Eq. (1.9). The parameters of the model can be estimated using any suitable method, and the original system parameters can be found by using an inverse transform. More information on continuous-time modeling can be found in [Johansson et al., 1999] and [Chou et al., 1999].

Persistence of Excitation

Persistence of excitation is a property of the input signal supplied to the process. If an input signal is persistently exciting *enough*, parameter estimates will be consistent. The concept of persistence of excitation can be viewed as an indicator of how informative the input signal is. One may also check how exciting a pair (x,y) of input-output data obtained from experiments is. The number of non-zero singular values of the regressor matrix

$$\Phi = \begin{pmatrix} \Phi_y & \Phi_x \end{pmatrix} \tag{1.11}$$

give the experimental excitation [Johansson, 2017].

Parameter Estimation

Once a set of input-output data is available, different techniques may be used to obtain a set of parameter values that relates the inputs to the output. The techniques may be recursive or non-recursive. Different estimation techniques have different properties. In this thesis project, a Kalman filter is used to carry out the parameter estimation. This approach has previously been shown to work in the efforts to model an AUV [Tiano et al., 2007].

The Kalman filter is a recursive equation, which makes use of knowledge of a dynamic model to predict future states of a system. Under certain conditions on the

system dynamics and noise processes acting on the system, it can be shown that the Kalman filter is the optimal state estimator in the sense that

$$E[(x_k - \hat{x}_k)^2],\ \mathrm{k} = 1, 2, \cdots \tag{1.12}$$

where x_k is the actual state and $\hat{x}_k$ is the state estimate at time instant k, is minimized [Johansson, 2017]. If a parameter estimation problem is formulated properly, a Kalman filter may be applied to the input-output data in order to estimate the parameter values recursively. The Kalman filter provides tools to handle finite data lengths, as the filter may be initialized using a guess of what the parameter value might be, and how certain this guess is. The initial guess should incorporate available theory and/or past estimation efforts. Further on, measurement noise levels may be incorporated in the filter equations. For more information on the Kalman filter, the reader is referred to [Jakobsson, 2015] and [Johansson, 2017].

Model Validation

To determine what model structure and what parameter set describes a process the best, some sort of measure of performance must be defined. As discussed earlier in this section, the main purpose of a model is to predict future states, given the current states and input signals. A measure that can be used for model validation is the Normalized Root-Mean-Square Error (NRMSE) of the one-step prediction errors. The NRMSE is calculated as [Olofsson et al., 2014]

$$1 - \frac{||x_N - \hat{x}_N||_2}{||x_N - \bar{x}_N||_2} \tag{1.13}$$

where x_N is the sequence of measured validation data, $\hat{x}_N$ is the sequence of 1-step predictions, and where $\bar{x}_N$ is the mean of the measured validation data. As discussed in [Ljung, 2009], a NRMSE value of 100% means that the predicted and measured values coincide. A value of 0% indicate that the model does no better than randomly guessing.

Statistical validation methods include checking the properties of the one-step prediction errors [Johansson, 2017]. Given a hypothesis, one wishes to show that the prediction errors have the same statistical properties as in the hypothesis. For instance, one may want to check the autocorrelation of the prediction errors for a certain number of lags. If the hypothesis is that the noise acting on the system is white, the objective of the model is to produce prediction errors such that this sequence is also white. Further tests include counting the number of zero-crossings of the prediction errors in order to detect offsets in the prediction errors.

It is quite common that all the checks above are performed using the assumption that the underlying disturbances are white, i.e. that the disturbances are uncorrelated in time [Johansson, 2017]. Consequently, the tests try to assert whether the prediction errors are white, and that all the available structure has been captured by the

model. However, it is of course not necessary that the underlying noise distribution is white. An advantage of the Kalman filter, is that noise models are estimated as a natural step of the parameter estimation. These noise models may be used to simulate the statistical properties of the noise. More specifically, one may simulate

$$x_{k+1} = \Phi x_k + K w_k \tag{1.14}$$

$$y_k = C x_k + v_k \tag{1.15}$$

$$\tag{1.16}$$

where Φ is the obtained discrete-time system matrix, K is the noise model, and where w_k are realizations of a normal distributed random process. v_k represent measurement noise and should be selected to correspond to the expected noise levels of the sensors. If the statistical properties of y_k resemble those of the prediction errors, one may more confidently say that the model has successfully captured the dynamics of the system being modeled.

1.4 Controller Structures

Current Controller Design

The current SROV control system is based on multiple gain scheduled SISO PID controllers. In general, a SISO PID will calculate a control signal according to

$$u(t) = K\left(e(t) + \tfrac{1}{T_i}\int e(\tau)d\tau + T_d\tfrac{de(t)}{dt}\right) \tag{1.17}$$

where $e(t)$ denotes the control error $r(t) - y(t)$. The existing field of knowledge on PID control is vast. For a discussion on the properties of PID control, the reader is referred to any elementary text on control theory. The overall control system of the SROV has numerous automatic functions, such as automatic depth/altitude, automatic pitch, and automatic roll. Given an automatic function, the control system calculates a desired action for each thruster. Once all automatic functions have been considered, the sum of all actions for each thruster is calculated, and consequently put out as the control signal. The thrusters operate in open loop, as the current design of the hydraulic system does not admit any measurements of the differential pressure across the thrusters to be made.

Model Predictive Control

Model Predictive Control (MPC) is a model-based control scheme. The idea behind MPC control, is that system responses for different control actions can be predicted (simulated) using an available system model. The predictions can incorporate constraints on the input signals and output states. The costs of different input sequences are evaluated using some sort of performance index. One possible choice of index

is a quadratic cost function, for which convex optimization solvers exist. A typical cost function is

$$J(u) = \sum_{i=0}^{p} (x_{k+i} - x_{k+i}^r)^T Q_x (x_{k+i} - x_{k+i}^r) + \sum_{i=0}^{m} (\Delta u_{k+i})^T Q_u (\Delta u_{k+i}) \tag{1.18}$$

Using the different weight matrices Q_x and Q_u, the user may tell the controller what states are deemed more important than others. All in all, a convex constrained optimization problem has to be solved. Once an optimal control sequence has been found, the first control action is applied to the system, after which all other samples are discarded and the process of predicting system outputs is repeated. A deeper discussion on MPC is given in [Johansson, 2015].

1.5 Limitations

Some limitations to the scope of this project are given in this section of the report.

Depth

The coefficients of Eq. (1.3) will vary with depth. The model is thus limited to a certain depth range. All experiments should be carried out at similar depths.

Tether Angle

A crucial point that was made during an interview with the designer of the SROV control system, was the fact that the angle at which the tether attaches to the SROV (which is variable, hereafter denoted θ_{TA}) has a big impact on the dynamics of the system. A schematic drawing of the tether angle can be seen in Fig. 1.5. If only the dynamics of the SROV were to be modeled, the tether could be neglected. However, the aim of this thesis is to model the entire system comprising the SROV, which includes the effect of the tether. If, for instance, the tether attaches to SROV from straight behind the vehicle, the tether will exert a torque in the pitch degree of freedom. This effect has to be considered. In order to build a functioning model, θ_{TA} has to be taken into account. As this state cannot be measured using any of the SROV sensors, some difficulties arise. In this thesis project, camera feeds available during the trials will be used to estimate θ_{TA}, and to keep it fixed through all experiments. The LPV model identified will be limited to the θ_{TA} used during the experiment session.

Experiment Limitations

The trials were carried out on a campaign with the vessel Stril Explorer from 2018-01-04 to 2018-01-08. Prior to the trials, the experiment plan (refer to Sec. 3.1) was

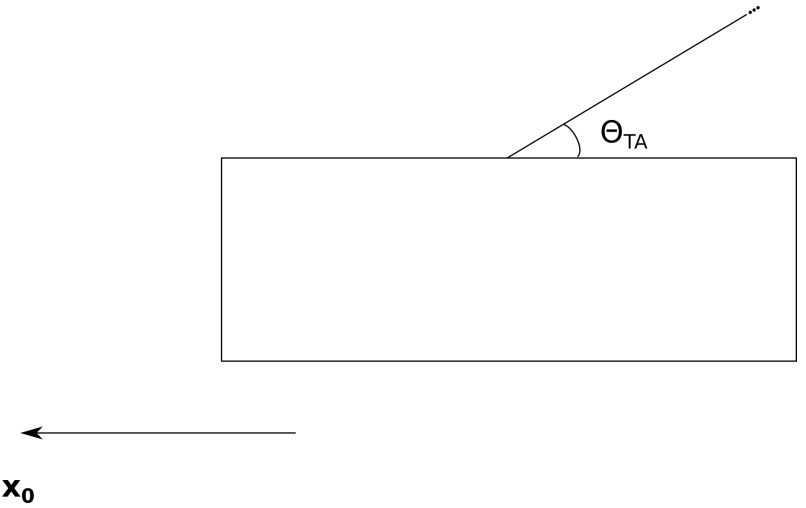

Figure 1.5 The tether angle is defined as the angle at which the tether attaches to the SROV. This angle is variable and affects the dynamics of the SROV.

reviewed together with the ROV supervisor on Stril Explorer. It was concluded that the experiments designed for the recursive estimation scheme were not executable in practice. The ROV pilots were not comfortable with operating the vehicle in all degrees of freedom simultaneously. Instead, it was decided that the recursive and dynamic experiments would coincide. After all, an assumption made early on in the project, was that the system could be considered decoupled at low forward speeds.

The SROV could not be operated in open loop for all freedom degrees. Before any experiments were carried out, the SROV pilot tried to fly the SROV at low velocities without any control systems. It quickly became clear that this was unsafe, and it was thus decided to use control systems when deemed appropriate to make sure that the system would not be damaged in any way.

In the experiment plan, the scheduling points of the LPV model were picked according to Eq. (3.2). During the trials, some of the experiments using $x = 4.0$ knts could not be carried out. In particular, it was deemed unsafe to perform experiments in the vertical degree of freedom. When the SROV was moving at higher forward velocities, the pitch angel grew larger than what was deemed safe. Figure 1.6 depicts some of the problem. During the initial part of the experiment, the resulting pitch angle is moderate. This part of the experiment was carried out at lower forward velocities. In the later part of the experiment, performed at higher forward velocities, the SROV pitch angle grows quite large even for moderate references. Due to this safety concern, no experiments were carried out for $x = 4.0$ knts. The LPV scope thus had to be limited to only the first seven entries of Eq. (3.2).

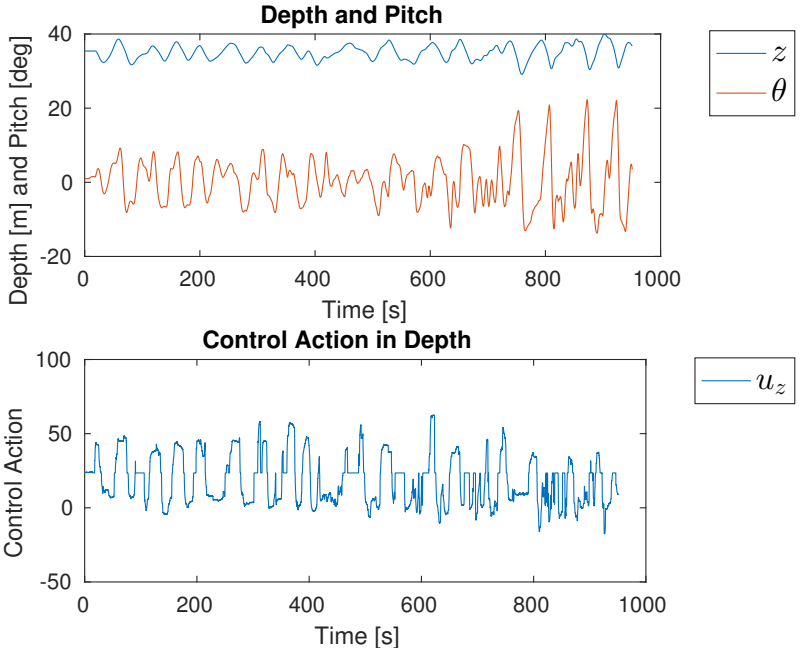

Figure 1.6 Depth and pitch dependency

2

Methodology

2.1 Literature Study

The project work started off with a literature study, in which different modeling approaches were compared. Since there is some knowledge of the physics of ROVs in general, it was decided that a gray-box approach would be preferable to black-box models. As every literature source encountered have successfully been using the model described by Eq. (1.3), it was decided that this model should be used in the thesis research.

2.2 Simulations

Prior to the experiments were designed, simulations were carried out to get an understanding of how the process should be excited to allow the model parameters to converge. Data was simulated using the model described in Eq. (1.3), and parameter values were estimated using a Kalman filter. By choosing different input signals when generating the input-output data through simulations, and evaluating the performance of the found models on a validation set, it could be concluded what input signals were likely to be good and what signals were less likely to be apt. Based on this data, the input signals for the experiments could be chosen.

2.3 Experiment Design

Two different experiments were designed prior to the trials. The experiment design can be reviewed in Sec. 3.1.

2.4 Trials

On top of the input-output data that were collected, a set of validation data was also recorded during the trials. This data contained motions in the entire spectrum of all

signals that the LPV model is expected to cover. Thus, the validation data contained signals satisfying $u \in [0.5, 4]$ knts, $v \in [-1, 1]$ knts, $w \in [-1, 1]$ knts, $r \in [-0.3, 0.3]$ rad/s, $p \in [-0.3, 0.3]$ rad/s, and $q \in [-0.3, 0.3]$ rad/s. These data were not used when building the parameter estimates, but only when validating the identified models.

The data sets were logged using two programs on different computers. The SROV control logger sampled the controller actions at 10 Hz. This sample frequency could not be changed. Thus, the software logging motion data from the SROV INS had to be limited to 10 Hz as well. The output of both data sources were time stamped, but there was no synchronization between the computers running the different pieces of software. To make sure that motion data corresponding to the correct controller inputs would be obtained for the parameter estimation algorithms, a Matlab script was created that automatically found the index that one of the signals needed to be shifted in order to match the other. This script was based on the fact that some of the signals were recorded by both softwares (e.g., depth). By matching these signals, an appropriate number of lags could be found to synchronize the signals. Once a complete set of signals were at hand, it was saved and used as input-output data for the parameter estimation algorithm.

2.5 Parameter Estimation

Kalman Filter Identification

The identification of the full model described in Eq. (1.3) can be carried out in several consecutive steps. The first step is concerned with estimation of the entries of $g(\eta)$ given experiment data. The experiments for the estimation of $g(\eta)$ were designed such that all velocities were constant and equal to zero. Thus, Eq. (1.3) simplifies to

$$g(\eta) = \tau \tag{2.1}$$

Using the known structure of $g(\eta)$ (see Eq. (1.5)) and the recorded values of τ and η, the constant unknowns of $g(\eta)$ were estimated. For clarification, the entries of $g(\eta)$ being estimated were $\hat{W} = W - B$ and $\hat{W}_{zGB} = z_G W - z_B B$. Further on, since the tether is attaching to the SROV from straight behind the vehicle, a constant pitch moment will be exerted on the SROV by the tether. This moment is denoted τ_θ, and was estimated together with the constant entries of $g(\eta)$. The estimators used were

$$\hat{W} = \frac{1}{N} \sum_{k=0}^{N-1} \frac{\tau_w(k)}{cos(\theta(k))cos(\phi(k))} \tag{2.2}$$

$$\hat{W}_{zB} = \frac{1}{N} \sum_{k=0}^{N-1} \frac{\tau_w(k)}{sin(\theta(k))} \tag{2.3}$$

$$\hat{\tau}_\theta = \frac{1}{N} \sum_{k=0}^{N-1} \tau_q(k) \tag{2.4}$$

where τ_w denotes the input signal in the vertical degree of freedom, and where τ_q is the input in the pitch degree of freedom. The estimators were based on experiments designed such that

$$sin(\theta(k)) \neq 0,\ k = 0,1,\cdots N-1 \tag{2.5}$$

and

$$cos(\theta(k))cos(\phi(k)) \neq 0,\ k = 0,1,\cdots N-1 \tag{2.6}$$

to ensure that the estimators defined by Eqs. (2.2-2.3) were well-defined. As the effect of the tether is not modeled (since there are no measurable inputs to use), all further estimations work with the identified pitch moment canceled from τ. The second step of the model parameter estimation is to transform Eq. (1.3) to

$$M\dot{\nu} + (C(\nu) + D(\nu))\nu = \gamma(\eta) \tag{2.7}$$

$$\gamma(\eta) = \tau - g(\eta) \tag{2.8}$$

That is, the part of the input signal needed to cancel the restoring forces and moments is removed from the total input. As a final simplification, it is assumed that the entries of the term $C(\nu) + D(\nu)$ can not be estimated separately. Instead, Eq. (2.7) is written

$$M\dot{\nu} + \bar{D}(\nu)\nu = \gamma(\eta) \tag{2.9}$$

It should here be noted that Eq. (2.9) can be written

$$\dot{\nu} = -M^{-1}\bar{D}\nu + M^{-1}\gamma \tag{2.10}$$

under the condition that M is invertible. This is not a too restrictive assumption, as symmetry implies that M is positive definite. In other words, the system can be written on state-space form with

$$A = -M^{-1}\bar{D} \tag{2.11}$$

$$B = M^{-1} \tag{2.12}$$

As a continuous-time model was wanted, the time series ν and $\gamma(\eta)$ were filtered through known filters given by Eq. (1.9). The resulting signals were used to estimate parameters of the transformed system

$$\dot{x} = A_\lambda x + B_\lambda u \tag{2.13}$$

as discussed in Sec. 1.3. There are many techniques that may be used for the parameter estimation. In this report, a Kalman Filter was used. The filtered time series $x_k = [\lambda\nu]_k$, $u_k = [\lambda\gamma]_k$ were used to estimate the entries of the state-space model matrices. The initial guess in the Kalman Filter algorithm was based on the Rigid Body transformation data of the SROV. Since filtered signals have been used for the estimation, the estimated state-space model is describing a transformed system. It

can be shown that the transformed system matrices $\hat{A}_\lambda$ and $\hat{B}_\lambda$ relates to the real system matrices via

$$\hat{A} = (\hat{A}_\lambda - I)/T \tag{2.14}$$

$$\hat{B} = \hat{B}_\lambda / T \tag{2.15}$$

A derivation is provided in Appendix 7.1. After the transformation back to the continuous-time system is performed, the matrices M and $\bar{D}$ may be calculated from Eqs. (2.11-2.12).

A script for estimation of the full LPV model was implemented in Matlab. Input-output data were supplied to the scripts as input arguments, and a full LPV model was returned by the script. The LPV script implemented the method described above. As an alternative, support for using a Matlab native system identification function was also implemented. The Matlab function n4sid, which is a subspace-based method for estimation of state space models, was intended to be used as a supplement to the Kalman Filter estimation scheme.

2.6 Validation

Define τ as the input signals to the SROV, and ν as the outputs. Before parameter estimation was carried out, the properties of the input-output data were investigated. To evaluate the aptitude of the input-output data for estimation, the following properties were investigated:

- Power spectral density of the input
- Cross spectral density of the input and output
- Estimated coherence spectrum from input to output
- Estimated transfer function magnitude from input to output
- Singular values of the regressor matrix (to determine the number of identifiable parameters).

Verification of the identified models were carried out on validation data collected during the trial campaign. The validation data set was not used for the estimation of parameters. To evaluate how well the models could describe the validation data, the identified LPV models were discretized using a zero order hold approximation. The discretization time $h = 0.1$s was used. Two different methods for making 1-step predictions were implemented. The first implementation was

$$\hat{x}(k+1|k) = \Phi_u x(k) + \Gamma_u u(k) \tag{2.16}$$

where the subscript u indicates that the discretized state-space model satisfying

$$\arg\min_i(u - r(i)),\ x = \{0.5, 1.0, \cdots, 3.5\} \tag{2.17}$$

where the entries of x are the LPV scheduling variables, has been used for the predictions. The second prediction scheme performs the predictions based on a weighted interpolation of the output of the closest matching LPV sub models:

$$\begin{aligned} \hat{x}(k+1|k) = &(\Phi_{u-1}x(k) + \Gamma_{u-1}u(k))w(k) \\ &+ (\Phi_u x(k) + \Gamma_u u(k))(1 - w(k)) \\ w(k) \in &[0, 1] \end{aligned} \tag{2.18}$$

The edge cases (i.e., for $u < 0.5$ knts and $u > 3.5$ knts), only the model closest matching the scheduling variable was used for predictions. Some of the validation was performed on the 1-step prediction errors, defined as

$$e(k+1) = x(k+1) - \hat{x}(k+1|k) \tag{2.19}$$

Several different measures of validity based on 1-step predictions were evaluated. The measures used in this thesis were

- Diagrams of actual and predicted outputs
- Estimated autocorrelation functions of the error sequences
- Estimated cross correlation functions of the input and error sequences
- Normalized root-mean-squared error
- Norm plots of error sequences
- Number of zero-crossings of error sequence
- Qualitative study of simulations of the estimated noise model

Another validation method approached, was to evaluate 10-step predictions. A model capable of generating accurate k-step predictions is desirable, as the model may then be used as a foundation for the MPC algorithm.

Further validation measures were also evaluated. Simulations using the identified LPV model and a known input sequence were performed. The resulting simulated states were then compared to the recorded states. The simulations were performed according to

$$\hat{x}(k+1|k) = \Phi\hat{x}(k|k-1) + \Gamma(k)u(k) \tag{2.20}$$

$$\hat{x}(0) = x(0) \tag{2.21}$$

where Φ and Γ were chosen according to one of the two schemes described previously. Note that the sequence u was pre-processed such that the effect of $g(\eta)$ and θ_{tether} was removed. Obviously, a good fit of the simulated data to the data obtained during the test run is attractive.

2.7 Controller Simulations

Simulations of closed-loop system responses, using the identified model for one forward speed (e.g., 2 knts), were performed to evaluate different controller behaviors. The controllers used for simulations were PID (diagonal to reflect the current system limitations) and a full-state MPC controller. All simulations were carried out in Simulink and using a sampling frequency of 20 Hz, reflecting the sampling frequency of the SORV. To implement the MPC regulator, *MPCtools* [Åkesson, 2018] was used. The MPC structure was initialized using a prediction horizon of $H_p = 20$ samples and a control horizon corresponding to $H_u = 14$ samples. Constraints on the input signals were chosen to reflect the constraints posed by the real system (i.e., limits on thruster actuation and total HPU power supply). The model used by the MPC regulator was perturbed (using an additive perturbation of a magnitude of about 10% of the entries in the system matrices) to account for model uncertainty, and only added on the main diagonal of the state-space matrices (as these terms are dominating in the identified system). The MPC controller was also augmented with integral states to make the system states go to the set points.

The simulations were carried out using measurement noise (normally distributed with zero mean and variance corresponding to that observed in the data records from the campaign on Stril Explorer), and load disturbances of magnitudes similar to what would be expected. In the case of underwater vehicles, load disturbances typically come in the shape of ocean currents which may be modeled as slowly varying random walks [Fossen, 1994]. Different trajectories and set-points, typical for the usage of the SROV, were simulated and qualitatively evaluated.

3

Experiment Plan

The experiments presented in this chapter of the report were designed prior to the trials were to be carried out. Before any experiments were performed, the suggested experiment plan was discussed with the SROV manager on Stril Explorer. It turned out, that some of the experiments were not possible to execute in practice. Some limitations were posed by time constriants, while safety considerations made other experiments infeasible. All dynamic experiments could be executed. Only very few of the static experiments could be performed, and none of the experiments in Sec. 3.3 could be undertaken.

3.1 Experiment Plan

The mathematical model that has been identified in the literature is given in Eq. (1.3). Using the sensors of the SROV, it is possible to measure/estimate the entries of the vector

$$z = \begin{pmatrix} \nu \\ \eta \end{pmatrix} \tag{3.1}$$

hereafter referred to as the measurement vector. We have that $z \in \mathbb{R}^{12\times 1}$. The components of z are discussed in section Sec. 1.2. The input signals to the SROV thrusters, denoted u_c, will be recorded. Since the SROV has 9 thrusters, we have $u_c \in \mathbb{R}^{9\times 1}$. Further on, the command in each degree of freedom will be recorded. This signal is denoted τ, and we have that $\tau \in \mathbb{R}^{6\times 1}$. If this was not the case, a thruster map would also be needed in order to move from the control input to each thruster to a command in each degree of freedom.

Two main approaches to the estimation of the parameters of the mathematical model have been identified:

1. Through the use of a recursive estimation technique (Kalman filter)

2. By performing static and dynamic experiments to identify parameters of Eq. (1.3) consecutively

After all experiments to be used for parameter estimation have been completed, some data have to be gathered for verification purposes. This data will only be used to verify the performance of the obtained model. The validation data set should contain all SROV output signals that the model is expected to cover. That means that all accelerations and speeds in the domain of the model should be contained in the validation set.

3.2 Experimental Setup

During the trials, the following actions should be performed:

- Experiments to allow for recursive estimation
- Experiments to allow for static and dynamic identification
- Collection of validation data

As the dynamics of the SROV are expected to be nonlinear, experiments will be carried out at equally spaced forward speed references according to

$$x = \{0.5,\ 1.0,\ 1.5,\ 2.0,\ 2.5,\ 3.0,\ 3.5,\ 4.0\} \tag{3.2}$$

The unit of the entries in x is knots. This is done in order to build a LPV model scheduled on forward speed, as discussed in Sec. 1.3.

3.3 Recursive Estimation Experiments

It is important that the input signals are sufficiently exciting. This means that a random input or some sort of square wave should be used as reference signal. The input signal cannot be constant or some sort of sinusoid in any degree of freedom. The input should ultimately be a square wave with a sufficiently long period. For every forward speed in the positive longitudinal degree of freedom given by x, the following actions should be taken:

- Movement in the lateral degree of freedom of the SROV. The speed should vary and satisfy $v \in [-1.5, 1.5]$ knots.
- Movement in the vertical degree of freedom of the SROV. The speed should vary and should satisfy $w \in [-1.5, 1.5]$ knots.
- Angular speed in the roll degree of freedom with speeds in the interval $p \in [-0.3, 0.3]$ rad/s.
- Angular speed in the pitch degree of freedom with speeds in the interval $q \in [-0.3, 0.3]$ rad/s.

Table 3.1 Table describing the experiment conditions for recursive estimation of the parameter values, with $a = 1.5$ knts and $b = 0.3$ rad/s.

u	v	w	p	q	r
$\in [0.2, 0.8]$	$\in [-a, a]$	$\in [-a, a]$	$\in [-b, b]$	$\in [-b, b]$	$\in [-b, b]$
$\in [0.7, 1.3]$	$\in [-a, a]$	$\in [-a, a]$	$\in [-b, b]$	$\in [-b, b]$	$\in [-b, b]$
$\in [1.2, 1.8]$	$\in [-a, a]$	$\in [-a, a]$	$\in [-b, b]$	$\in [-b, b]$	$\in [-b, b]$
$\in [1.7, 2.3]$	$\in [-a, a]$	$\in [-a, a]$	$\in [-b, b]$	$\in [-b, b]$	$\in [-b, b]$
$\in [2.2, 2.8]$	$\in [-a, a]$	$\in [-a, a]$	$\in [-b, b]$	$\in [-b, b]$	$\in [-b, b]$
$\in [2.7, 3.3]$	$\in [-a, a]$	$\in [-a, a]$	$\in [-b, b]$	$\in [-b, b]$	$\in [-b, b]$
$\in [3.2, 2.8]$	$\in [-a, a]$	$\in [-a, a]$	$\in [-b, b]$	$\in [-b, b]$	$\in [-b, b]$
$\in [4.7, 4.3]$	$\in [-a, a]$	$\in [-a, a]$	$\in [-b, b]$	$\in [-b, b]$	$\in [-b, b]$

- Angular speed in the yaw degree of freedom with speeds in the interval $r \in [-0.3, 0.3]$ rad/s.

As mentioned earlier, the experiments should be carried out with square wave or random control inputs in all degrees of freedom. It is important that enough time is given for the control action to have a noticeable effect on the system, before the control action is changed again. For each entry of x, an experiment lasting for at least 100 seconds should be run. In Table 3.1, a test schedule for the recursive estimation approach is proposed. Every row describes the setup of one experiment. All in all, 8 tests should be run in this part of the trial. The actions in all degrees of freedom stay in the same interval, except for the speed in the x-direction, which is varied around different mean values.

3.4 Static and Dynamic Experiments

The static and dynamic experiments have been designed to populate the entries of Eq. (1.3) consequtively. In this approach, a constant input signal would first be used to estimate the entries of $C(\nu) + D(\nu)$ using linear regression. The entries of M would not affect the system outputs as $\dot{\nu}$ would be the zero-vector after initial transients have died out. Once the entries of $C(\nu) + D(\nu)$ are known, the speed of the SROV can be varied in order to find the entries of M.

Static Experiments

The following experiments will be run to facilitate static and dynamic identification at the speeds defined in x. It should be noted that the LPV approach is scheduled on forward speed. First, make the SROV move at a constant speed in the positive longitudinal direction. The forward speeds are given by the entries of x. No other movement should be induced. Next, for every forward speed in the positive x-direction given by x, the following actions should be taken in consecutive order:

Table 3.2 Table describing the experiment conditions for static identification of damping and Coriolis coefficients in the y-direction of the SROV. The unit of the first three columns is knots, and the unit of the following three columns is rad/s.

u	v	w	p	q	r
0.5	± 1	0	0	0	0
1.0	± 1	0	0	0	0
1.5	± 1	0	0	0	0
2.0	± 1	0	0	0	0
2.5	± 1	0	0	0	0
3.0	± 1	0	0	0	0
3.5	± 1	0	0	0	0
4.0	± 1	0	0	0	0

- Constant linear speed of ± 1 knot in the lateral degree of freedom of the SROV.
- Constant linear speed of ± 1 knot in the vertical degree of freedom of the SROV.
- Constant angular speed of ± 0.3 rad/s in the roll degree of freedom of the SROV.
- Constant angular speed of ± 0.3 rad/s in the pitch degree of freedom of the SROV.
- Constant angular speed of ± 0.3 rad/s in the yaw degree of freedom of the SROV.

Note that $\pm x$ implies that one experiment should be run for x and one experiment should be run for $-x$. All in all, this gives 88 static experiments to run. Each experiment should be run until the set-point is reached and all transients have died out. After this steady-state is reached, the experiment should continue for at least 20 seconds. It is important that we have no acceleration in any freedom degree at the end of the experiments. Tables 3.2 and 3.3 show the setup for some of the experiments. Each row corresponds to two experiments; one where a positive speed is generated, and one where negative speed is generated in the specified DOF. Please note that these experiments should be performed in all degrees of freedom when applicable, even if only two tables have been presented. It may not be possible to perform the tests for the given angular speeds in the roll and pitch directions, as such inputs could cause the SROV to flip. If this is the case, the experiments should be run for shorter time sequences and using lower angular velocities.

Table 3.3 Table describing the experiment conditions for static identification of damping and Coriolis coefficients in the yaw-direction of the SROV. The unit of the first three columns is knots, and the unit of the following three columns is rad/s.

u	v	w	p	q	r
0.5	0	0	0	0	± 0.3
1.0	0	0	0	0	± 0.3
1.5	0	0	0	0	± 0.3
2.0	0	0	0	0	± 0.3
2.5	0	0	0	0	± 0.3
3.0	0	0	0	0	± 0.3
3.5	0	0	0	0	± 0.3
4.0	0	0	0	0	± 0.3

Dynamic Experiments

Next, dynamic experiments should be performed. In these experiments, it is important that there are accelerations in the different degrees of freedom. First, make the SROV move at an alternating speed in the positive x-direction. The forward speeds should vary around the entries of x. No other movement should be induced. Next, for every forward speed in the positive x-direction given by x, the following actions should be taken (note that the speed in the x-direction should be constant):

- Movement in the lateral degree of freedom of the SROV. The speed in the y-direction should vary and should satisfy $v \in [-1.5, 1.5]$ knots.
- Movement in the vertical degree of freedom of the SROV. The speed in the z-direction should vary and should satisfy $w \in [-1.5, 1.5]$ knots.
- Angular speed in the roll degree of freedom of the SROV, with speeds in the interval $p \in [-0.3, 0.3]$ rad/s.
- Angular speed in the pitch degree of freedom of the SROV, with speeds in the interval $q \in [-0.3, 0.3]$ rad/s.
- Angular speed in the yaw degree of freedom of the SROV, with speeds in the interval $r \in [-0.3, 0.3]$ rad/s.

Every experiment should be run for a sufficient amount of time, but at least 30 seconds as this time allowed for parameter estimate convergence in simulations. Tables 3.4 and 3.5 show the experimental conditions for some of the tests to be carried out.

Table 3.4 Table describing the experiment conditions for estimating the entries of the mass and inertia matrix M in the y-direction of the SROV. The unit of the first three columns is knots, and the unit of the following three columns is rad/s.

u	v	w	p	q	r
0.5	$\in [-1.5, 1.5]$	0	0	0	0
1.0	$\in [-1.5, 1.5]$	0	0	0	0
1.5	$\in [-1.5, 1.5]$	0	0	0	0
2.0	$\in [-1.5, 1.5]$	0	0	0	0
2.5	$\in [-1.5, 1.5]$	0	0	0	0
3.0	$\in [-1.5, 1.5]$	0	0	0	0
3.5	$\in [-1.5, 1.5]$	0	0	0	0
4.0	$\in [-1.5, 1.5]$	0	0	0	0

Table 3.5 Table describing the experiment conditions for estimating the entries of the mass and inertia matrix M in the roll-direction of the SROV. The unit of the first three columns is knots, and the unit of the following three columns is rad/s.

u	v	w	p	q	r
0.5	0	0	$\in [-0.3, 0.3]$	0	0
1.0	0	0	$\in [-0.3, 0.3]$	0	0
1.5	0	0	$\in [-0.3, 0.3]$	0	0
2.0	0	0	$\in [-0.3, 0.3]$	0	0
2.5	0	0	$\in [-0.3, 0.3]$	0	0
3.0	0	0	$\in [-0.3, 0.3]$	0	0
3.5	0	0	$\in [-0.3, 0.3]$	0	0
4.0	0	0	$\in [-0.3, 0.3]$	0	0

3.5 Validation Data

The validation data set is collected to verify the functionality of the mathematical model that is built on the training data sets. The validation data should contain constant speeds in all directions, as well as alternating speeds. All speeds used for the scheduling must be covered by the validation data. This implies that $u \in [0.2, 4.3]$. The following experiments will be run to obtain validation data

- Movement at variable speeds in the xyz-directions with the forward speed in the range specified above. Variations in pitch, roll and yaw must also be obtained. The validation set should contain constant as well as changing velocities.
- Collect at least 300 seconds worth of validation data.

4

Results

4.1 Simulations

Simulations based on the model structure identified in the literature study, showed that a square-wave like input signal would be appropriate. This is also in accordance with the notation of persistence of excitation [Ljung, 1987], [Johansson, 2017]. It was further concluded that the input steps in the different freedom degrees must be applied for a sufficient amount of time, such that a measurable effect on the output signals can be recorded.

The recursive estimation algorithm was implemented and tested on simulated continuous-time model data. Simulations were carried out for N = 4000 samples. The system matrix A was changed at t = 2000. The state-space model used for the first half of the experiment was

$$\dot{x} = Ax + Bu \tag{4.1}$$

with

$$A = \begin{pmatrix} -1 & 3 \\ -1 & -4/3 \end{pmatrix} \tag{4.2}$$

$$B = \begin{pmatrix} 0.0003 & 0.0001 \\ 0.0001 & 0.0003 \end{pmatrix} \tag{4.3}$$

$$C = \begin{pmatrix} 1 & 0 \\ 0 & 1 \end{pmatrix} \tag{4.4}$$

$$D = \begin{pmatrix} 0 & 0 \\ 0 & 0 \end{pmatrix} \tag{4.5}$$

and the system matrix was later changed to

$$A = \begin{pmatrix} -1/2 & -3 \\ 2 & -4/3 \end{pmatrix} \tag{4.6}$$

The resulting parameter estimates using two square wave signals as input can be seen in Fig. 4.1-4.2. In Fig. 4.3-4.4, the parameter estimates using two PRBS inputs can be seen.

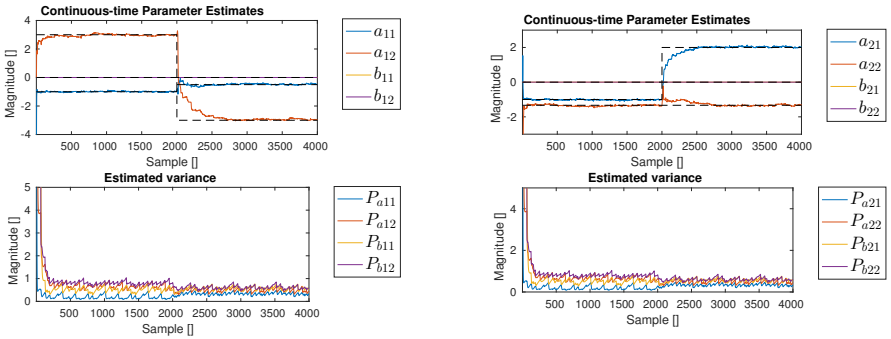

Figure 4.1 Continuous-time parameter estimate evolution using the Kalman filter scheme discussed in Sec. 2.5. The input signal was selected to be two square-wave signals. The plots were created to verify the functionality of the implementation of the Kalman filter scheme for continuous-time model estimation.

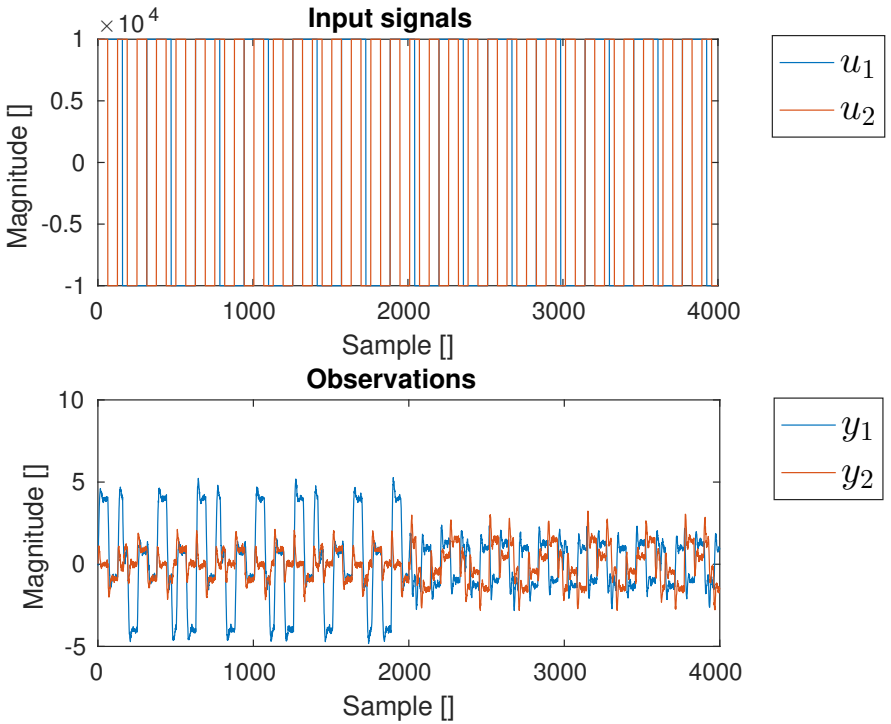

Figure 4.2 Simulated input and output signals of the experiments to verify the functionality of the implemented Kalman filter using a square wave input.

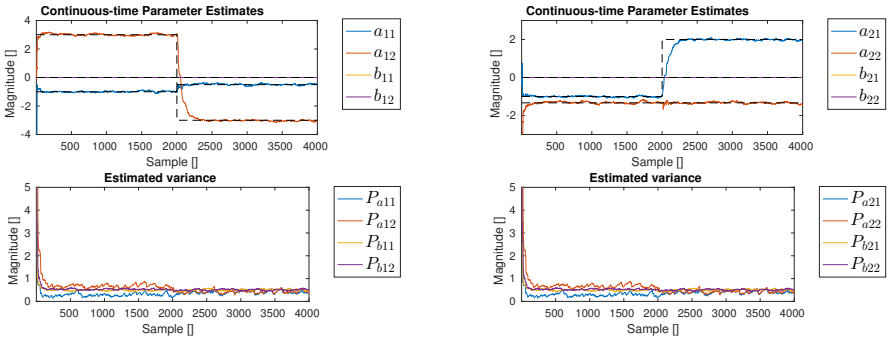

Figure 4.3 Continuous-time parameter estimate evolution using the Kalman filter scheme discussed in Sec. 2.5. The input signal was selected to be two PRBS signals. The plots were created to verify the functionality of the implementation of the Kalman filter scheme for continuous-time model estimation.

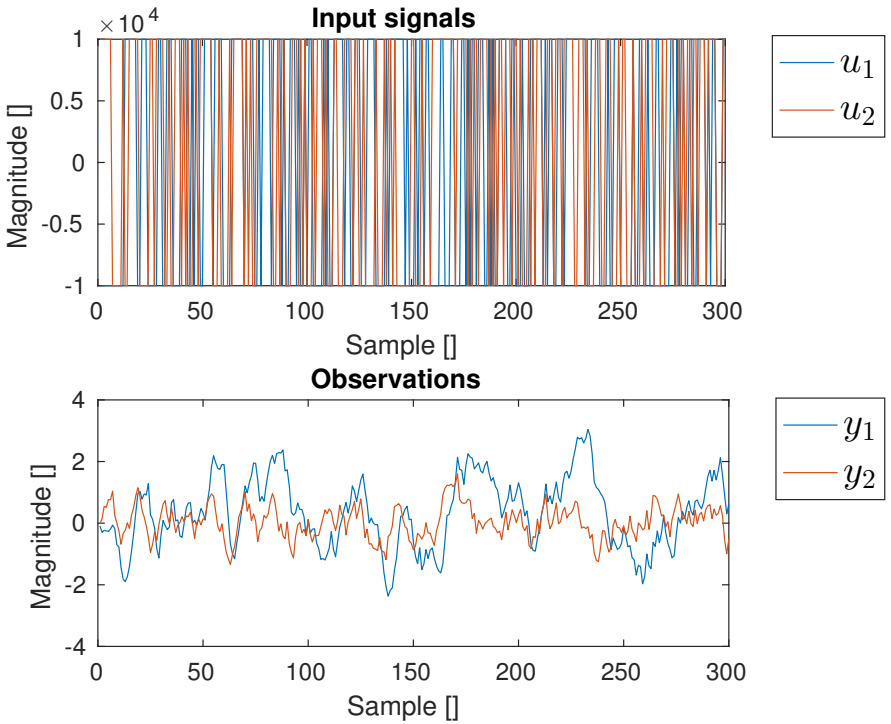

Figure 4.4 Simulated input and output signals of the experiments to verify the functionality of the implemented Kalman filter using a PRBS input.

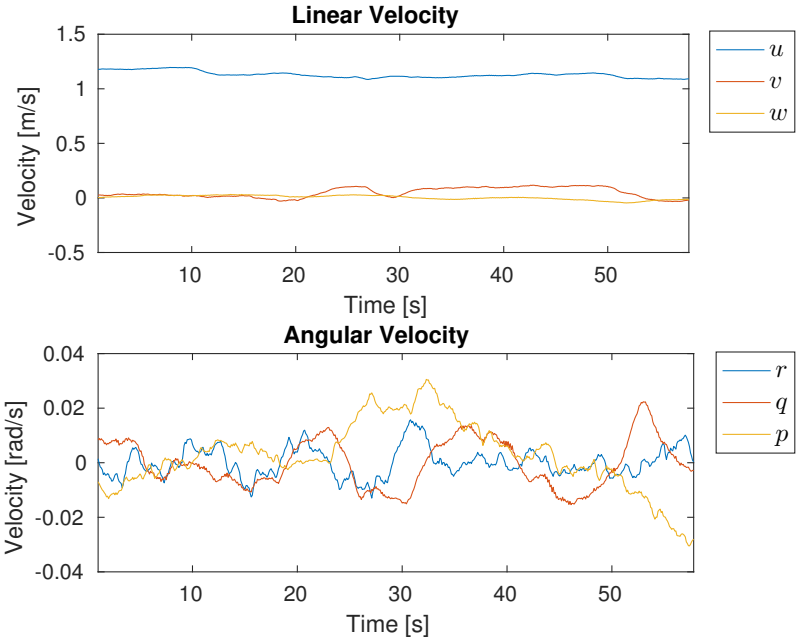

Figure 4.5 Linear and angular velocities recorded during the sea trials on board Stril Explorer. These are considered output signals of the SROV.

4.2 Trials

During the trials, numerous signals were recorded. To give the reader an understanding of what the signals looks like, a small portion of the data is presented in Figs. 4.5-4.7.

During the trial campaign, other tests than the ones needed for this thesis were also carried out. These trials had higher priority than the thesis research. The time consumption estimated for the tests of the thesis were too optimistic, and thus not all of the tests could be carried out. All dynamic/recursive tests were completed, as were the static experiments carried out to identify the vector of restoring forces and moments $g(\eta)$. Of all the tests designed to identify drag coefficients, only tests for a forward speed of 2 knts could be completed before the trials had to be broken off. This will still allow for comparisons between the performance of the static and recursive methods to be carried out, but only for the case when the forward speed of the validation data set is 2 knts. However, this will at least give a hint about the performance of the different models.

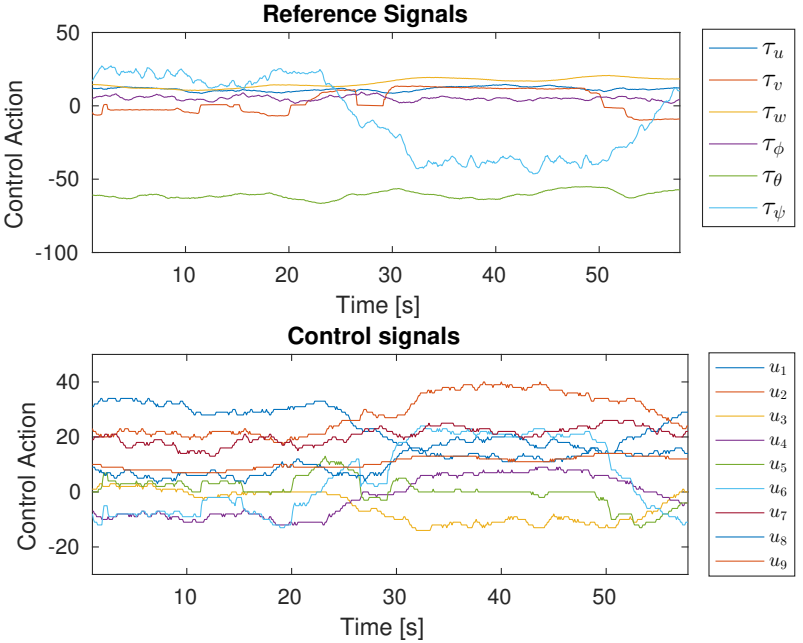

Figure 4.6 References in each freedom degree (as recorded by the SROV control logger software), and the control action for each thruster. Note that the signals are all in % of full positive/negative reference/thrust.

4.3 Signal Properties

The signal investigation was evaluated for all inputs and all outputs, and for all LPV grid variables. It was found that, for low frequencies, there was a coherence of acceptable magnitude between some of the signals, whereas coherence was weak between other signal pairs. Figures 4.8-4.9 show the signal properties for the dynamic experiments carried out in roll for a fixed forward speed $u = 0.5$ knts. All figures depicting the signal properties of the different experiments are shown in Appendix 7.2.

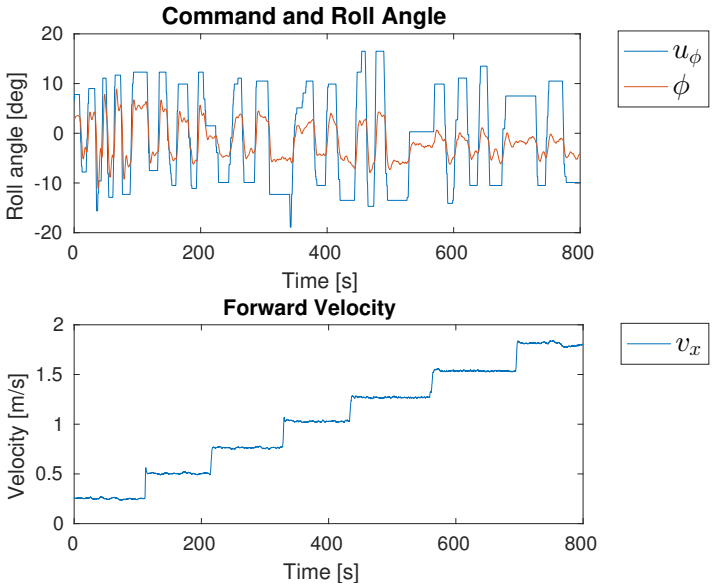

Figure 4.7 Roll and forward velocity dependency.

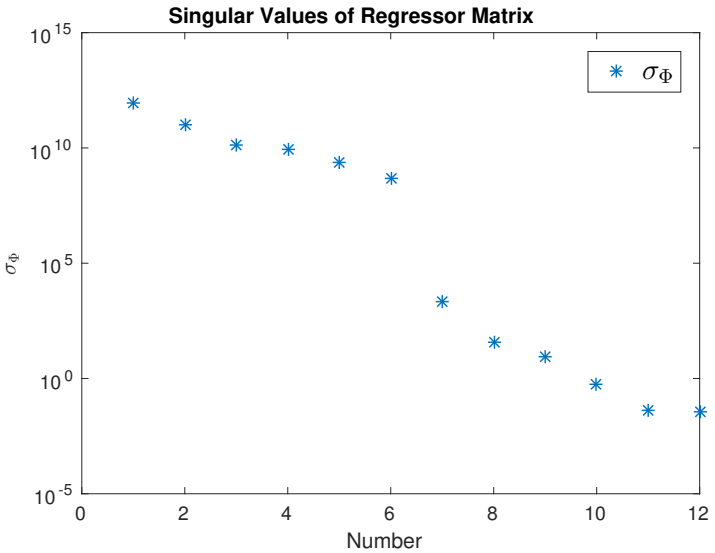

Figure 4.8 Singular values of the regressor matrix $\Phi = \begin{pmatrix}\Phi_y & \Phi_x\end{pmatrix}$ for the dynamic roll experiment when $u = 0.5$ knts.

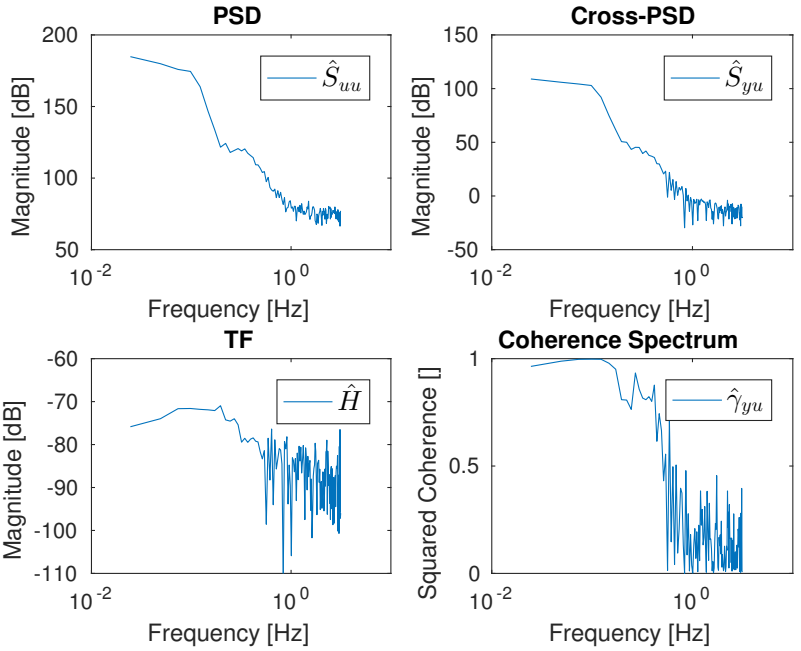

Figure 4.9 Signal properties of one of the dynamic experiments in roll, when the forward speed was fixed to $u = 0.5$ knts. The upper left plot shows the power spectral density of the input signal γ_p. The upper right plot shows the cross PSD of γ_p and p, where p is the resulting roll angular velocity (i.e., the output signal). The lower left plot shows an estimate of the transfer function magnitude from input to output, and the lower right plot shows the coherence spectrum. All functions are plotted versus frequency.

4.4 Uncoupled Dynamics

Parameter Estimation

The matrices presented were obtained for the LPV grid variable $u = 3.0$ knts. The added mass matrix was estimated to be

$$M_{KF} = 1.0 \cdot 10^9 \begin{pmatrix} 0.01 & 0 & 0 & 0 & 0 & 0 \\ 0 & 0.068 & 0 & 0 & 0 & 0 \\ 0 & 0 & 1.3083 & 0 & 0 & 0 \\ 0 & 0 & 0 & 0.5896 & 0 & 0 \\ 0 & 0 & 0 & 0 & 0.1887 & 0 \\ 0 & 0 & 0 & 0 & 0 & 2.8955 \end{pmatrix} \begin{pmatrix} kg \\ kg \\ kg \\ kgm^2 \\ kgm^2 \\ kgm^2 \end{pmatrix}$$

and combined damping and Coriolis matrix

$$D_{KF} = 1.0 \cdot 10^7 \begin{pmatrix} 0.0172 & 0 & 0 & 0 & 0 & 0 \\ 0 & 0.1165 & 0 & 0 & 0 & 0 \\ 0 & 0 & 2.2428 & 0 & 0 & 0 \\ 0 & 0 & 0 & 1.0782 & 0 & 0 \\ 0 & 0 & 0 & 0 & 0.2894 & 0 \\ 0 & 0 & 0 & 0 & 0 & 4.1288 \end{pmatrix} \begin{pmatrix} kg/s \\ kg/s \\ kg/s \\ kgm^2/s \\ kgm^2/s \\ kgm^2/s \end{pmatrix}$$

As a comparison, the Matlab native function n4sid was used to calculate the system matrices. The model matrices obtained for $u = 3.0$ knts were

$$M_{n4} = 1.0 \cdot 10^7 \begin{pmatrix} 0.2699 & 0 & 0 & 0 & 0 & 0 \\ 0 & 0.5232 & 0 & 0 & 0 & 0 \\ 0 & 0 & 0.7646 & 0 & 0 & 0 \\ 0 & 0 & 0 & 0.2146 & 0 & 0 \\ 0 & 0 & 0 & 0 & 1.3751 & 0 \\ 0 & 0 & 0 & 0 & 0 & 0.5830 \end{pmatrix} \begin{pmatrix} kg \\ kg \\ kg \\ kgm^2 \\ kgm^2 \\ kgm^2 \end{pmatrix}$$

and the combined Damping and Coriolis matrix was calculated as

$$D_{n4} = 1.0 \cdot 10^5 \begin{pmatrix} 0.2889 & 0 & 0 & 0 & 0 & 0 \\ 0 & 1.7653 & 0 & 0 & 0 & 0 \\ 0 & 0 & 2.9973 & 0 & 0 & 0 \\ 0 & 0 & 0 & 0.7480 & 0 & 0 \\ 0 & 0 & 0 & 0 & 0.4788 & 0 \\ 0 & 0 & 0 & 0 & 0 & 1.3617 \end{pmatrix} \begin{pmatrix} kg/s \\ kg/s \\ kg/s \\ kgm^2/s \\ kgm^2/s \\ kgm^2/s \end{pmatrix}$$

As can be noted, the magnitude of the system matrices obtained through the use of the different algorithms differ by a factor 100 in magnitude. The reason for this discrepancy is unclear, but one can at least say that the diagonal models are estimated to be very hard to affect using the input signals. As the control system is acting on

Table 4.1 Estimated values of the constant entries of the vector of restoring forces and moments, $g(\eta)$.

Parameter	Value
$(W-B)$	$3.55 \cdot 10^4$ N
$(z_G W - z_B B)$	$1.81 \cdot 10^5$ Nm
τ_{tether}	$-1.57 \cdot 10^4$ Nm

the system though M^{-1}, it will be virtually impossible to change the system states using the input signals. This is an indicator that the diagonal models are not suitable for describing the SROV.

The estimates of the entries of $g(\eta)$ and the effect of the tether are shown in Table 4.1.

Validation

The LPV models were evaluated on the validation set, which was recorded during the trials. In the following, the results of the residual analysis will be presented.

Residual Analysis of Kalman filter Estimated System The model evaluated here is a diagonal system obtained through the method described in Sec. 2.5. One-step predictions of the identified system on 4000 samples of the validation data can be seen in Fig. 4.10. In Figs 4.11-4.13, the estimated autocorrelation functions for some of the prediction error sequences are shown, together with (approximative) 99% confidence interval for a zero mean normal distribution. Norm plots of the innovation sequence are also provided. In Fig. 4.14, the estimated cross correlation functions of input signals and error sequences are provided. The NRMSE of the diagonal Kalman filter on the 4000 sample sequence of validation data are

$$\text{NRMSE}_{KF} = \begin{pmatrix} \text{fit}_u \\ \text{fit}_v \\ \text{fit}_w \\ \text{fit}_p \\ \text{fit}_q \\ \text{fit}_r \end{pmatrix} = \begin{pmatrix} 0.9797 \\ 0.9635 \\ 0.9524 \\ 0.8508 \\ 0.9160 \\ 0.8868 \end{pmatrix} \tag{4.7}$$

As a further measure of the model accuracy, the number of prediction error sequence zero crossings are calculated. These data may be used as a test of normality of the prediction error, but also give a clue about persistent offsets in predictions. For the

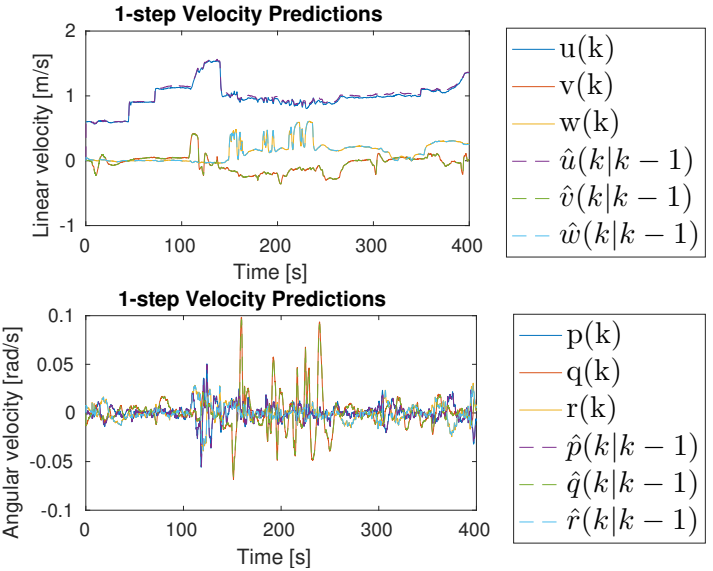

Figure 4.10 One-step predictions for the model estimated from the dynamic tests carried out on the SROV. Parameters estimated using a diagonal Kalman filter, and a discretization time of $0.1s$. The predictions are carried out using the full LPV model using the interpolation scheme described in the method section.

diagonal Kalman filter estimation technique, the number of zero crossings were

$$\text{nz}_{KF} = \begin{pmatrix} 851 \\ 1703 \\ 1796 \\ 1358 \\ 1774 \\ 1357 \end{pmatrix} \tag{4.8}$$

Since the length of the entire validation data set is 4000 samples, the number of zero crossings indicate that there are some offsets in the prediction errors, especially in the longitudinal degree of freedom.

To test whether the estimated model is capable of performing k-step predictions for longer time horizons (which is important for an MPC controller), predictions using $k = 10$ was performed. The resulting predictions and the corresponding auto-correlations of the prediction errors can be reviewed in Figs. 4.15-4.18. Figure 4.19 provide zoomed diagrams of the 10-step predictions carried out using the uncoupled system. Here it can clearly be seen that the produced predictions are basically delayed versions of the output state vectors.

As a further measure of the aptitude of the estimated model, simulations using

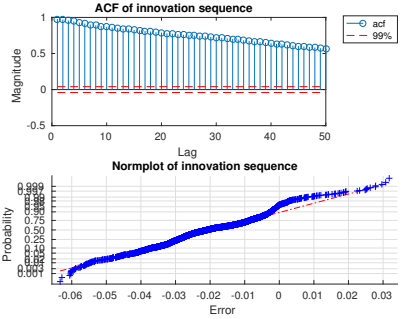

(a) Forward

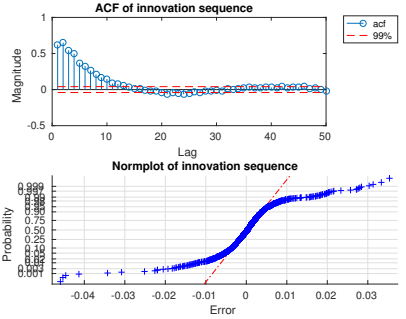

(b) Lateral

Figure 4.11 Estimated autocorrelation functions of the one-step prediction error sequence obtained using a diagonal LPV model estimated using a Kalman filter. The norm plots of the innovation sequences are also provided.

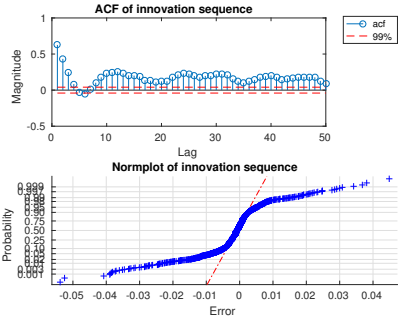

(a) Vertical

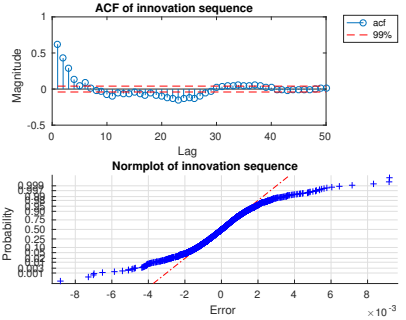

(b) Roll

Figure 4.12 Estimated autocorrelation functions of the one-step prediction error sequence obtained using a diagonal LPV model estimated using a Kalman filter. The norm plots of the innovation sequences are also provided.

a known input-output signal pair were carried out. For the distinction between this approach and k-step predictions, please refer to Sec. 2.6. The results of the simulations are shown in Figs. 4.20-4.21. The diagrams indicate that the uncoupled LPV model estimated using a Kalman filter is struggling in particular concerning the angular velocities. The high-frequency content of the recorded outputs are completely ignored by the simulations. All the results presented in this section indicate that an increase in model order would probably be suitable.

Residual Analysis of n4sid Estimated System As a comparison, the results of a diagonal system estimated through the subspace based Matlab function n4sid are

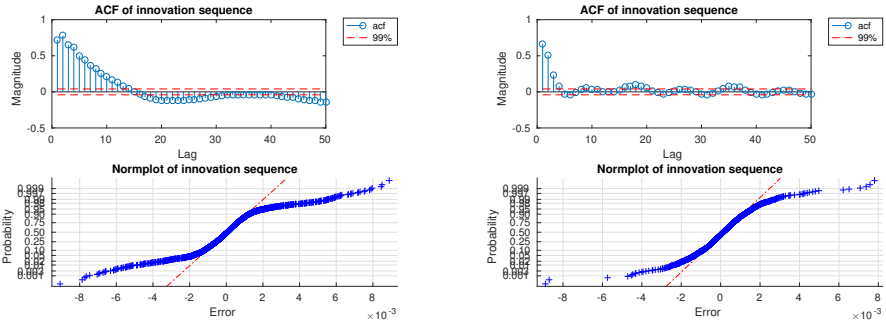

(a) Pitch (b) Yaw

Figure 4.13 Estimated autocorrelation functions of the one-step prediction error sequence obtained using a diagonal LPV model estimated using a Kalman filter. The norm plots of the innovation sequences are also provided.

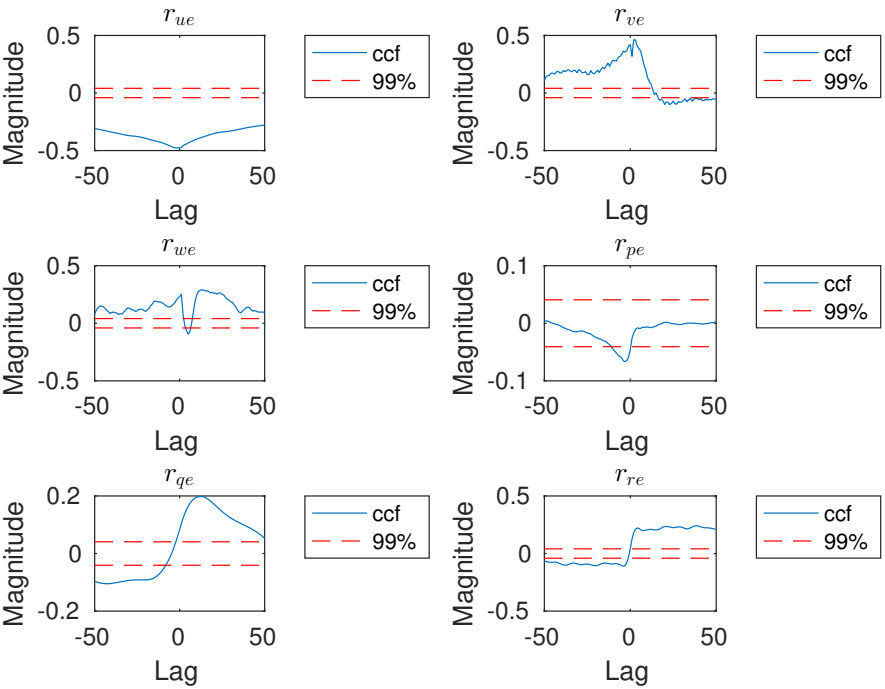

Figure 4.14 Estimated cross correlations between input and error from the different freedom degrees, using predictions based on a diagonal LPV model estimated using a Kalman filter.

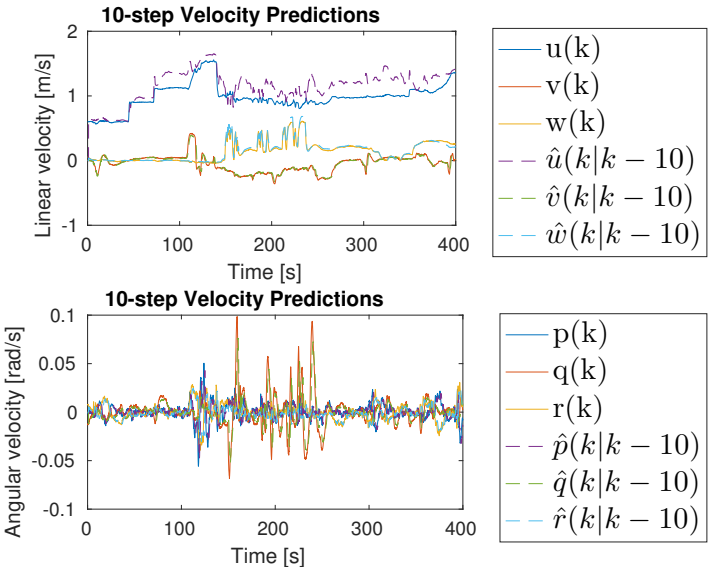

Figure 4.15 10-step predictions for the model estimated from the dynamic tests carried out on the SROV. Parameters estimated using a Kalman filter and uncoupled dynamics, and a discretization time of $0.1s$. The predictions were carried out using the full LPV model and the interpolation scheme described in the method section.

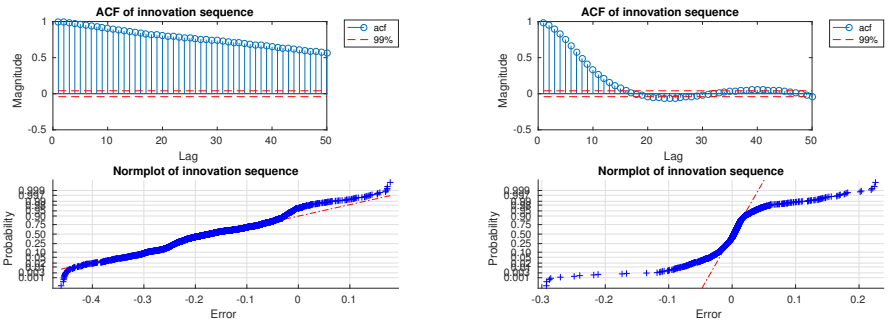

(a) Forward (b) Lateral

Figure 4.16 Estimated autocorrelation functions of innovation sequence in forward and lateral velocity for 10-step predictions using a diagonal LPV model. The entries of the LPV model were estimated using a Kalman filter. The norm plots of the innovation sequences are also provided.

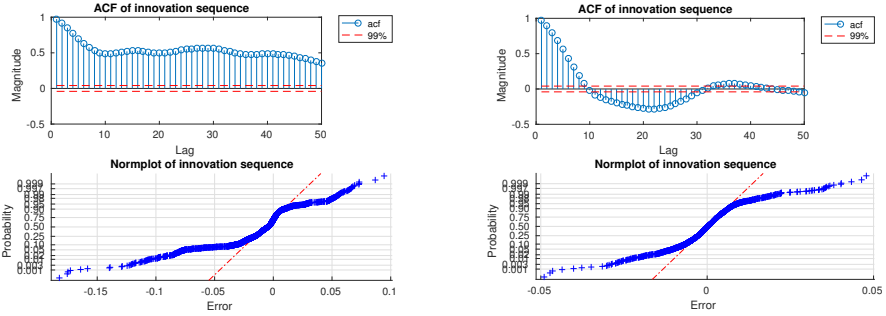

(a) Vertical (b) Roll

Figure 4.17 Estimated autocorrelation functions of innovation sequence in vertical and roll velocity for 10-step predictions using a diagonal LPV model. The entries of the LPV model were estimated using a Kalman filter. The norm plots of the innovation sequences are also provided.

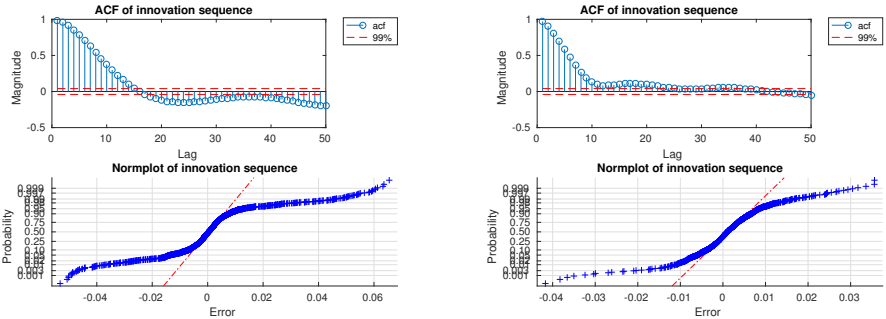

(a) Pitch (b) Yaw

Figure 4.18 Estimated autocorrelation functions of innovation sequence in pitch and yaw velocity for 10-step predictions using a diagonal LPV model. The entries of the LPV model were estimated using a Kalman filter. The norm plots of the innovation sequences are also provided.

presented below. One-step predictions of the identified system on the same 4000 samples of the validation data as in Sec. 4.4 can be seen in Fig. 4.22. In Figs. 4.23-4.25, the estimated autocorrelation functions for some of the prediction error sequences are shown, together with (approximative) 99% confidence interval for a zero mean Normal Distribution. Norm plots of the innovation sequence are also provided. In Fig. 4.26, the estimated cross correlation functions of input signals and error sequences are provided. The NRMSE of the diagonal n4sid on the

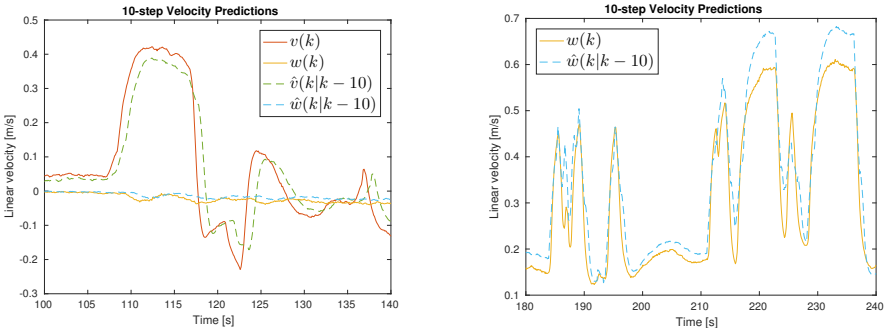

(a) Lateral (b) Vertical

Figure 4.19 Zoomed-in plots of the 10-step predictions carried out using the diagonal LPV model. The entries of the LPV model were estimated using a Kalman filter.

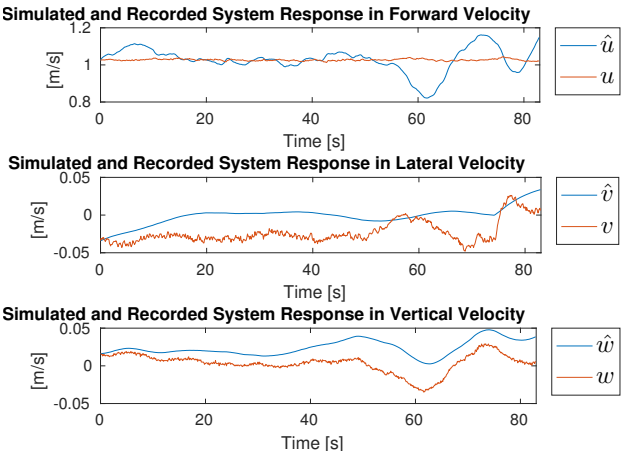

Figure 4.20 Simulated system response using the uncoupled LPV model estimated using a Kalman filter. The simulated linear velocities are presented. The discretization time of the continuous-time models was set to 0.1s. The simulated states were obtained using the interpolation scheme described in the method section. The data record used was collected during the trials, and was not used for the parameter estimations.

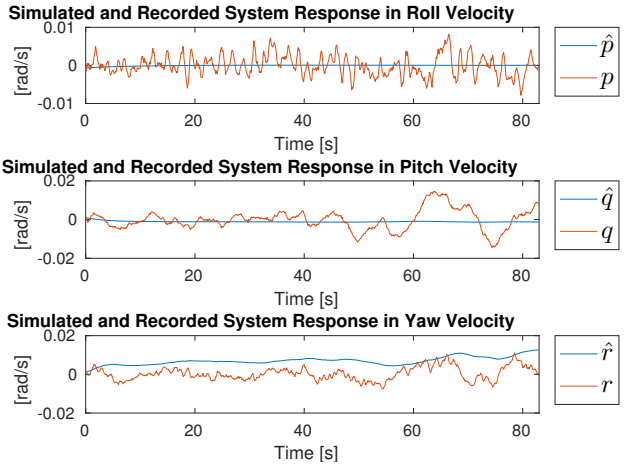

Figure 4.21 Simulated system response using the uncoupled LPV model estimated using a Kalman filter. The simulated angular velocities are presented. The discretization time of the continuous-time models was set to 0.1s. The simulated states were obtained using the interpolation scheme described in the method section. The data record used was collected during the trials, and was not used for the parameter estimations.

4000 sample sequence of validation data is

$$\text{NRMSE}_{n4} = \begin{pmatrix} \text{fit}_u \\ \text{fit}_v \\ \text{fit}_w \\ \text{fit}_p \\ \text{fit}_q \\ \text{fit}_r \end{pmatrix} = \begin{pmatrix} 0.9816 \\ 0.9636 \\ 0.9528 \\ 0.8509 \\ 0.9159 \\ 0.8868 \end{pmatrix} \tag{4.9}$$

For the diagonal n4sid estimation, the number of zero crossings were

$$\text{nz}_{n4} = \begin{pmatrix} 1599 \\ 1710 \\ 1910 \\ 1368 \\ 1762 \\ 1349 \end{pmatrix} \tag{4.10}$$

Notably, there are almost twice as many zero crossings in the longitudinal degree of freedom using the n4sid algorithm than when using the diagonal LPV model estimated using a Kalman filter.

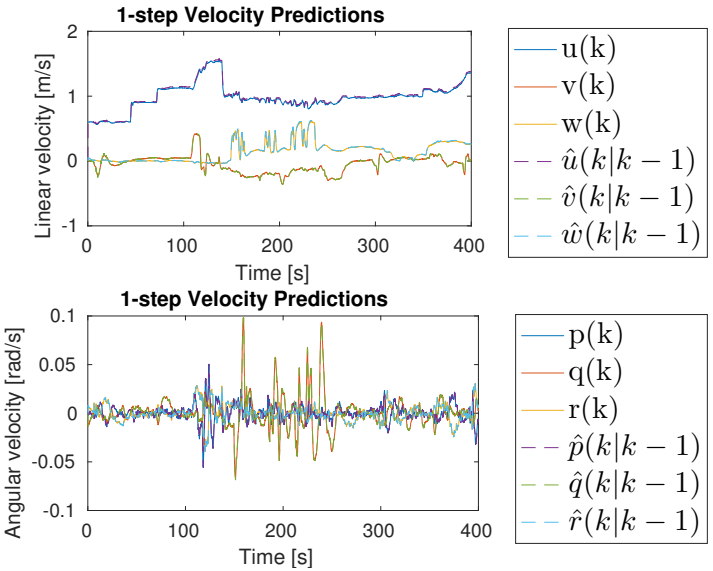

Figure 4.22 One-step predictions for the model estimated from the dynamic tests carried out on the SROV. Parameters estimated using a diagonal n4sid, and a discretization time of 0.1 s. The predictions are carried out using the full LPV model using the interpolation scheme described in the method section.

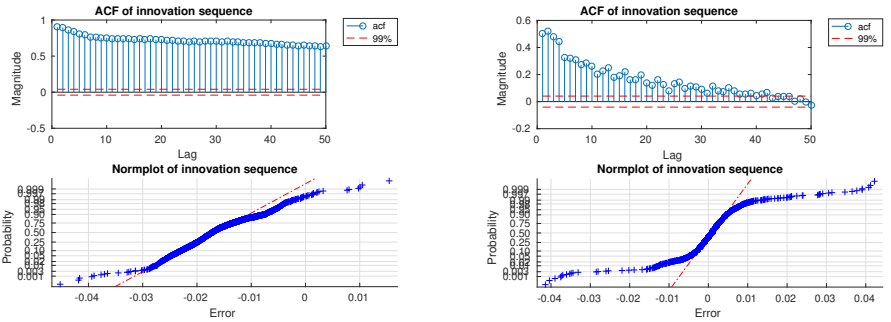

(a) Longitudinal (b) Lateral

Figure 4.23 Estimated autocorrelation function of innovation sequence in forward velocity. The entries of the LPV model were estimated using the subspace-based n4sid algorithm. The norm plot of the innovation sequence is also provided.

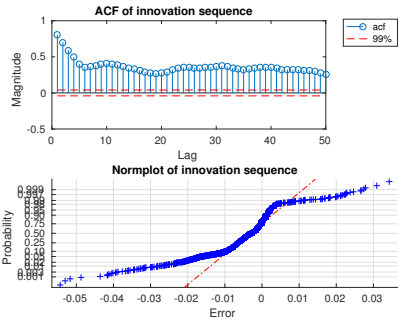

(a) Vertical

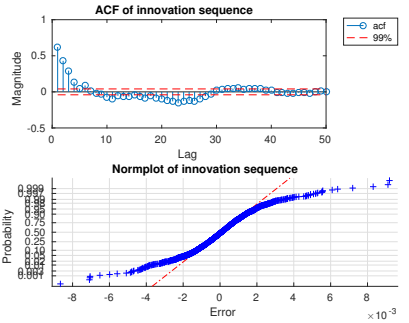

(b) Roll

Figure 4.24 Estimated autocorrelation functions of innovation sequence in vertical and roll velocity. The entries of the LPV model were estimated using the subspace-based n4sid algorithm. The norm plots of the innovation sequences are also provided.

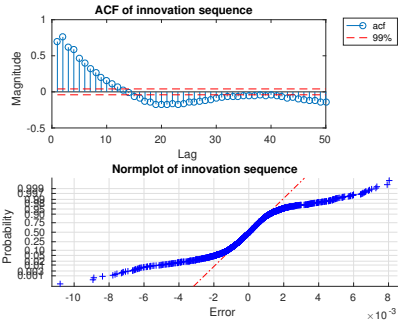

(a) Pitch

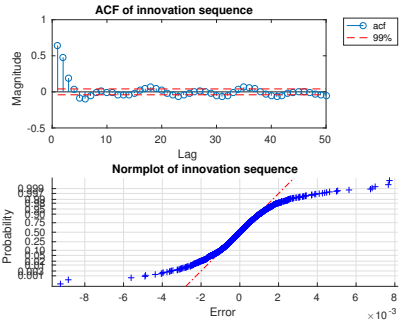

(b) Yaw

Figure 4.25 Estimated autocorrelation functions of innovation sequence in pitch and yaw velocity. The entries of the LPV model were estimated using the subspace-based n4sid algorithm. The norm plots of the innovation sequences are also provided.

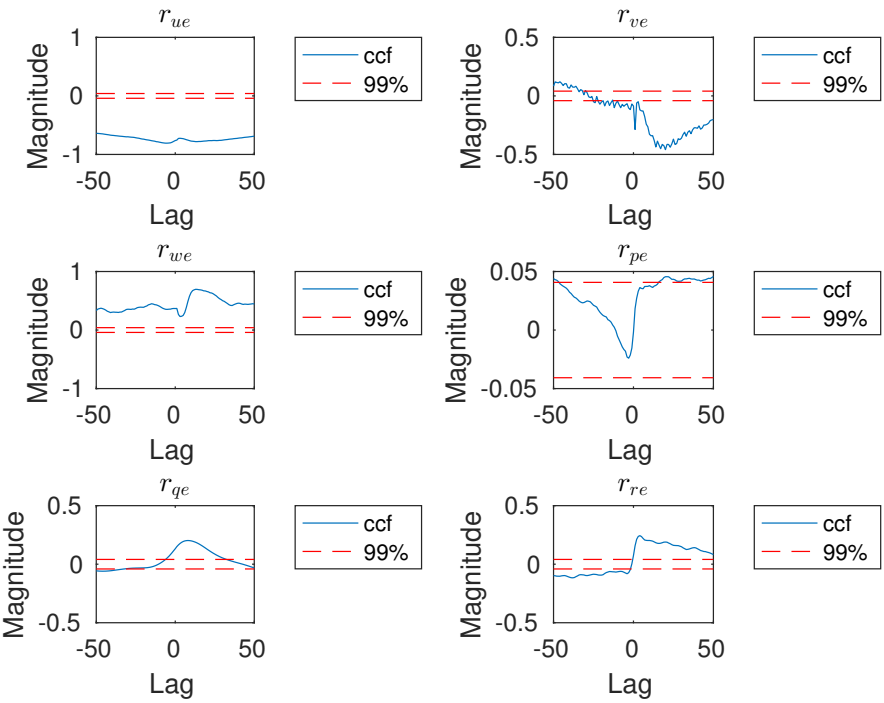

Figure 4.26 Estimated cross correlations between input and error from the different freedom degrees, using predictions based on a diagonal LPV model estimated using the sub-space based Matlab function n4sid.

4.5 Coupled Dynamics

Parameter Estimation

The matrices presented were obtained for the LPV grid variable $u = 3.0$ knts. The structure of the added mass matrix was found by investigating the coherence spectra in Appendix 7.2. The estimated add matrix was found to be

$$M_{KF} = 10^5 \cdot \begin{pmatrix} 0.3437 & 0 & -0.4223 & 0 & 0.1433 & 0 \\ 0 & 0.2183 & 0 & -0.0014 & 0 & -0.0386 \\ 0.1496 & 0 & -.6774 & 0 & 0.0186 & 0 \\ 0 & -0.0514 & 0 & -0.0301 & 0 & 0.0091 \\ -0.3544 & 0 & 1.0199 & 0 & 0.0111 & 0 \\ 0 & -0.0074 & 0 & 0 & 0 & 0.2979 \end{pmatrix} \begin{pmatrix} kg \\ kg \\ kg \\ kgm^2 \\ kgm^2 \\ kgm^2 \end{pmatrix}$$

and combined damping and Coriolis matrix

$$D_{KF} = 10^4 \cdot \begin{pmatrix} 0.4239 & 0 & -1.1815 & 0 & 0.9776 & 0 \\ 0 & 0.6001 & 0 & -0.0064 & 0 & -0.0154 \\ -0.0303 & 0 & -1.9059 & 0 & 0.3370 & 0 \\ 0 & -0.3641 & 0 & -0.0275 & 0 & 0.0036 \\ -0.5384 & 0 & 2.877 & 0 & -0.705 & 0 \\ 0 & -0.0465 & 0 & 0.0002 & 0 & 0.4986 \end{pmatrix} \begin{pmatrix} kg/s \\ kg/s \\ kg/s \\ kgm^2/s \\ kgm^2/s \\ kgm^2/s \end{pmatrix}$$

Validation

The coupled LPV model was evaluated on the validation set, similarly to the validation methods used for the uncoupled LPV models. In the following, the results of the residual analysis will be presented.

Residual Analysis of Kalman filter Estimated System The model evaluated here is a diagonal system obtained through the method described in Sec. 2.5. One-step predictions of the identified system on 4000 samples of the validation data can be seen in Fig. 4.27. In Figs 4.28-4.30, the estimated autocorrelation functions for some of the prediction error sequences are shown, together with (approximative) 99% confidence interval for a zero mean Normal Distribution. Norm plots of the innovation sequence are also provided. In Fig. 4.31, the estimated cross correlation functions of input signals and error sequences are provided. The NRMSE of the diagonal Kalman filter on the 4000 sample sequence of validation data is

$$\text{NRMSE}_{KF} = \begin{pmatrix} \text{fit}_u \\ \text{fit}_v \\ \text{fit}_w \\ \text{fit}_p \\ \text{fit}_q \\ \text{fit}_r \end{pmatrix} = \begin{pmatrix} 0.8971 \\ 0.9575 \\ 0.9615 \\ 0.8473 \\ 0.9207 \\ 0.8816 \end{pmatrix} \tag{4.11}$$

As a further measure of the model accuracy, the number of prediction error sequence zero crossings are calculated. This data may be used as a test of normality of the prediction error, but also give a clue about persistent offsets in predictions. For the diagonal Kalman filter estimation technique, the number of zero crossings were

$$\mathrm{nz}_{KF} = \begin{pmatrix} 123 \\ 848 \\ 886 \\ 1316 \\ 1591 \\ 1165 \end{pmatrix} \tag{4.12}$$

These results show that the coupled LPV model generate predictions that render in even less prediction error zero crossings than the uncoupled LPV models. Also, the NRMSE score of the coupled LPV model in the longitudinal degree of freedom is lower. To test whether the estimated model is capable of performing k-step predictions for longer time horizons (which is important for an MPC controller), predictions using $k = 10$ was performed. The resulting predictions and the corresponding autocorrelations of the prediction errors can be reviewed in Figs. 4.32-4.35. As can be seen in Fig. 4.36, the coupled LPV model is actually producing predictions that are not just delayed versions of the state vector.

As a further measure of the aptitude of the estimated model, simulations using a known input signal were carried out. For the distinction between this approach and k-step predictions, please refer to Sec. 2.6. The results of the simulations are shown in Figs. 4.37-4.38. As in the case of the uncoupled LPV model, the coupled model is struggling with the high-frequency content of the angular velocity states. However, the coupled LPV model is performing better considering the linear velocities. In particular, the simulations of the lateral and vertical velocities capture the shapes of the corresponding recorded outputs.

To give the reader an idea of how the Kalman filter estimations converge, the filter evolution for two of the experiments are provided. In Fig. 4.39, the parameter estimates for an experiment in forward velocity (when $u =$) are shown as a function of time. The estimated parameter variances and the input signals to the Kalman filter are also shown. Figure 4.40 show the results for an experiment in roll (when u = 3.5 knts).

Noise Model Simulations

In Figs. 4.41 to 4.43, the results of a simulation using the estimated noise model are presented. As discussed in Sec. 1.3, the noise models obtained through the use of the identification algorithms were used to obtain the simulation results.

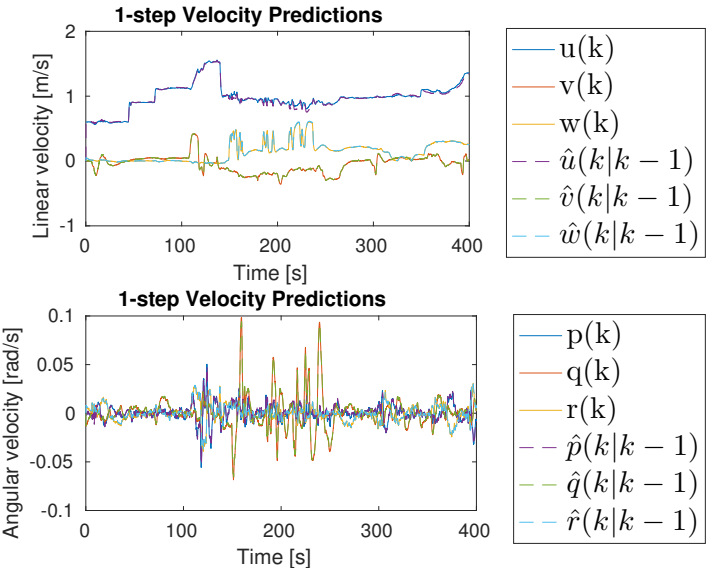

Figure 4.27 One-step predictions for the model estimated from the dynamic tests carried out on the SROV. Parameters estimated using a Kalman filter and coupled dynamics, and a discretization time of $0.1s$. The predictions are carried out using the full LPV model and the interpolation scheme described in the method section.

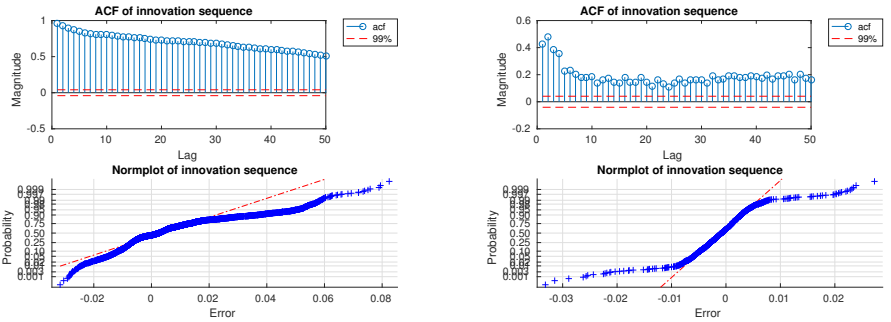

(a) Forward (b) Lateral

Figure 4.28 Estimated autocorrelation functions of innovation sequence in forward and lateral velocity when using a coupled LPV model to obtain predictions. The norm plots of the innovation sequences are also provided.

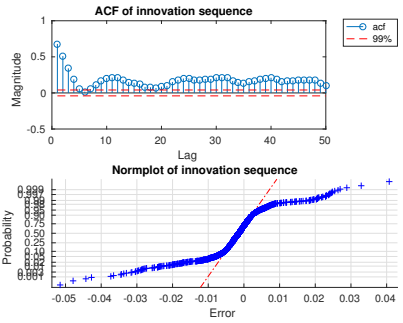

(a) Vertical

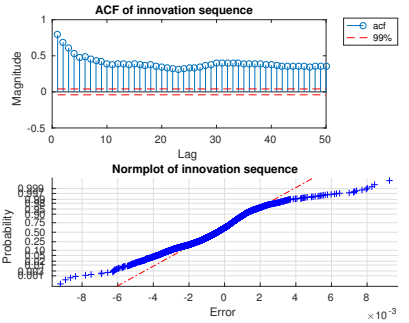

(b) Roll

Figure 4.29 Estimated autocorrelation functions of innovation sequence in vertical and roll velocity when using a coupled LPV model to obtain predictions. The norm plots of the innovation sequences are also provided.

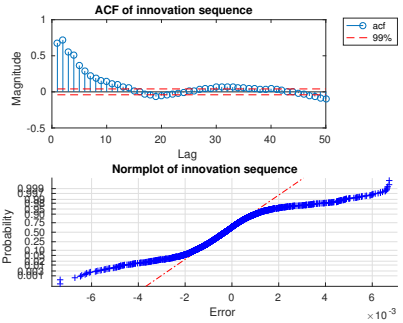

(a) Pitch

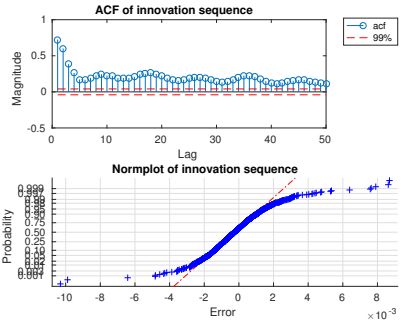

(b) Yaw

Figure 4.30 Estimated autocorrelation functions of innovation sequence in pitch and yaw velocity when using a coupled LPV model to obtain predictions. The norm plots of the innovation sequences are also provided.

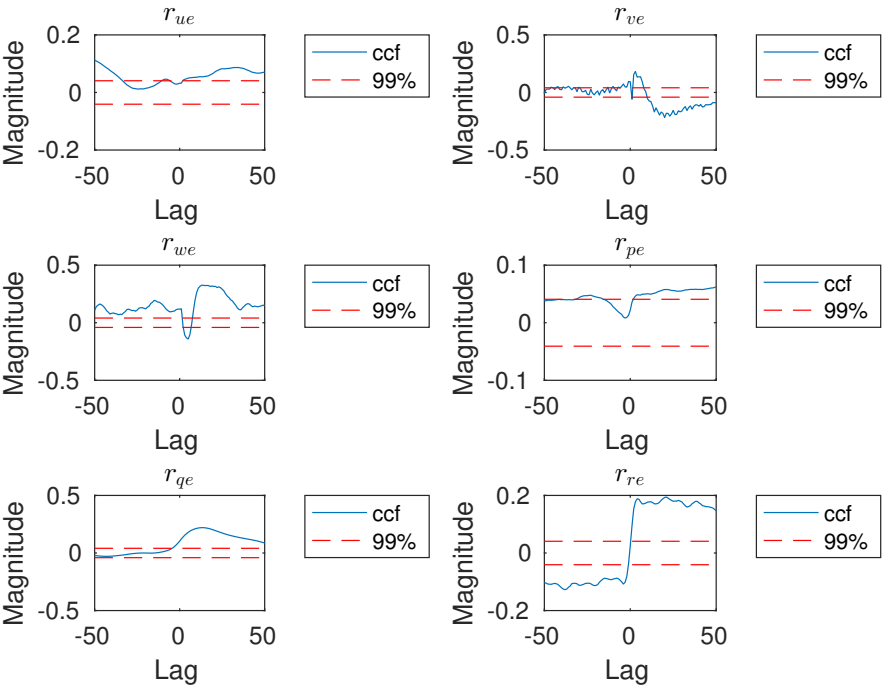

Figure 4.31 Estimated cross correlations between input and innovation from the different freedom degrees, using predictions based on a coupled LPV model estimated using a Kalman filter.

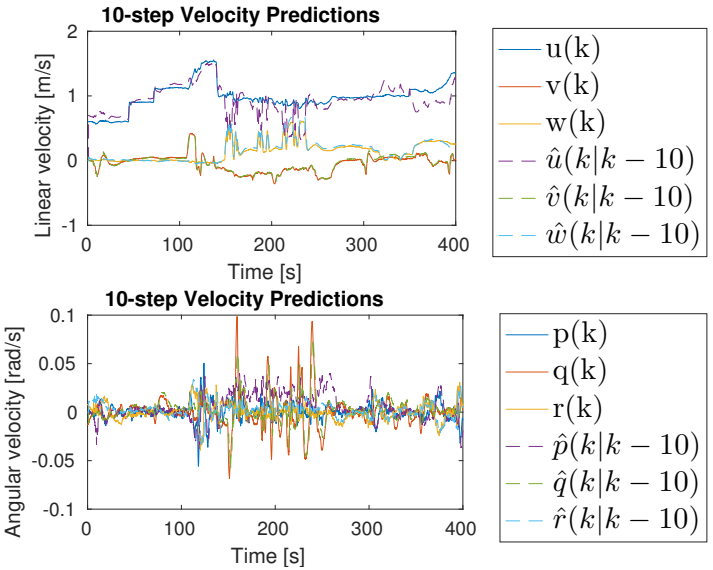

Figure 4.32 10-step predictions for the model estimated from the dynamic tests carried out on the SROV. Parameters estimated using a Kalman filter and coupled dynamics, and a discretization time of $0.1s$. The predictions were carried out using the full LPV model and the interpolation scheme described in the method section.

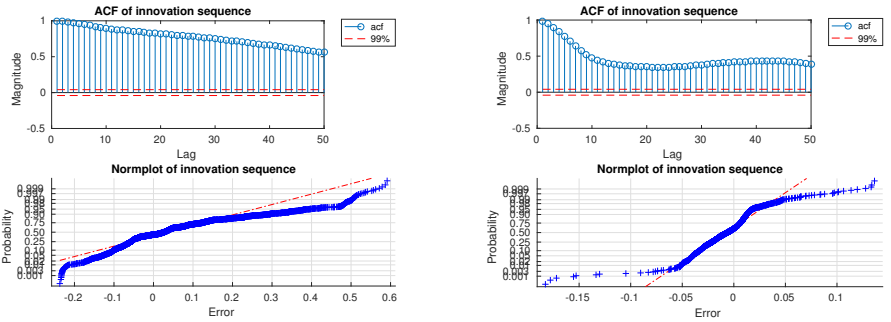

(a) Forward (b) Lateral

Figure 4.33 Estimated autocorrelation functions of innovation sequence in forward and lateral velocity for 10-step predictions when using a coupled LPV model to obtain predictions. The norm plots of the innovation sequences are also provided.

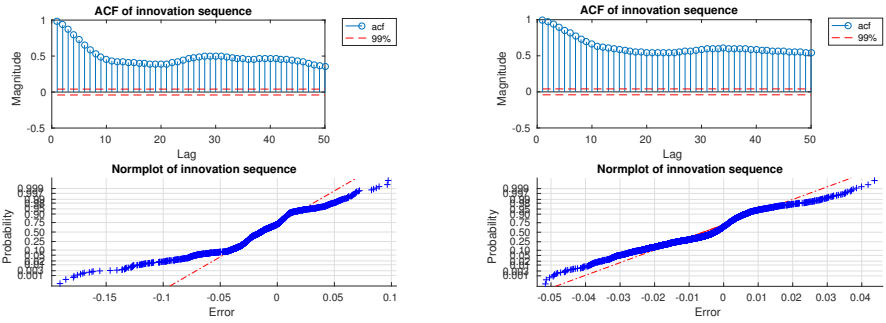

(a) Vertical (b) Roll

Figure 4.34 Estimated autocorrelation functions of innovation sequence in vertical and roll velocity for 10-step predictions when using a coupled LPV model to obtain predictions. The norm plots of the innovation sequences are also provided.

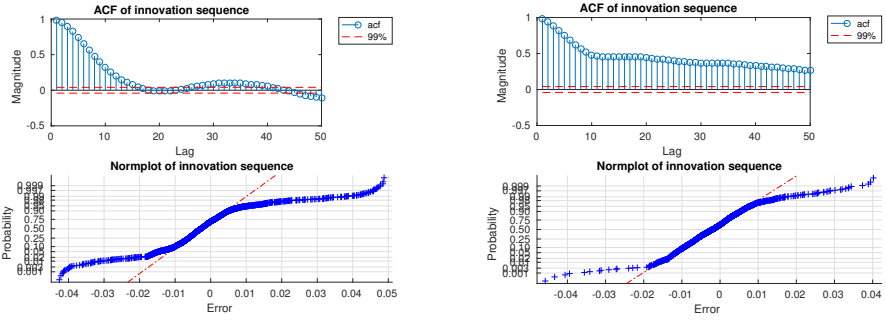

(a) Pitch (b) Yaw

Figure 4.35 Estimated autocorrelation functions of innovation sequence in pitch and yaw velocity for 10-step predictions when using a coupled LPV model to obtain predictions. The norm plots of the innovation sequences are also provided.

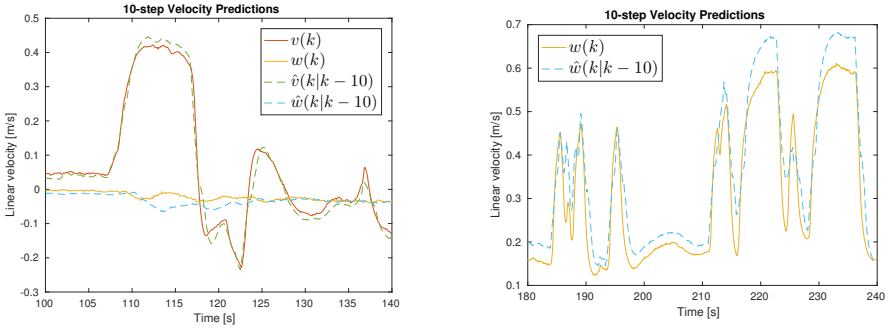

(a) Lateral (b) Vertical

Figure 4.36 Zoomed-in plots of the 10-step predictions carried out using the coupled LPV model.

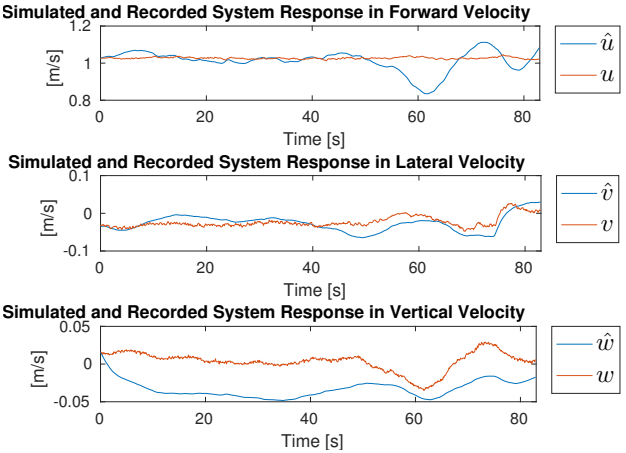

Figure 4.37 Simulated system response using the coupled LPV model estimated using a Kalman filter. The simulated linear velocities are presented. The discretization time of the continuous-time models was set to 0.1 s. The simulated stated were found using the interpolation scheme described in the method section. The data record used was collected during the trials, and was not used for the parameter estimations.

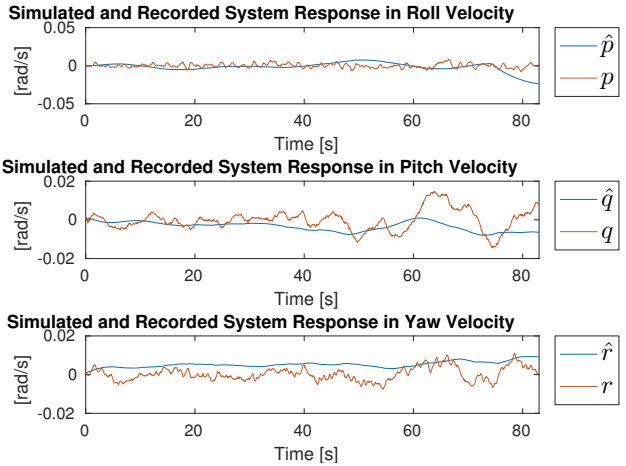

Figure 4.38 Simulated system response using the coupled LPV model estimated using a Kalman filter. The simulated angular velocities are presented. The discretization time of the continuous-time models was set to 0.1 s. The simulated stated were found using the interpolation scheme described in the method section. The data record used was collected during the trials, and was not used for the parameter estimations.

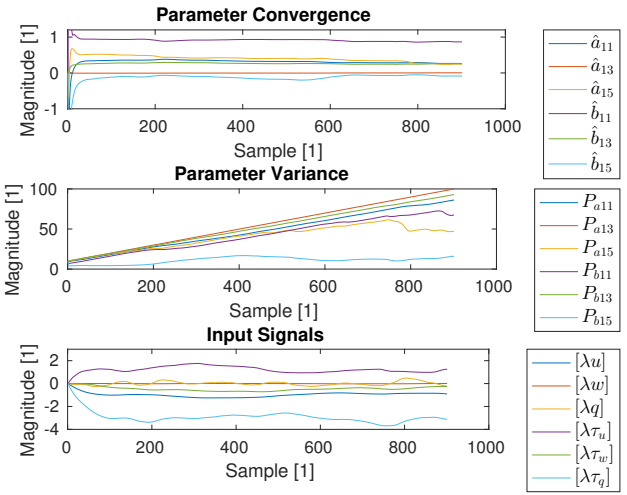

Figure 4.39 Parameter estimates as a function of time, where the estimates were produced using a Kalman filter. The data was obtained as the dynamic experiment in the longitudinal degree of freedom for u= 2.0 knts.

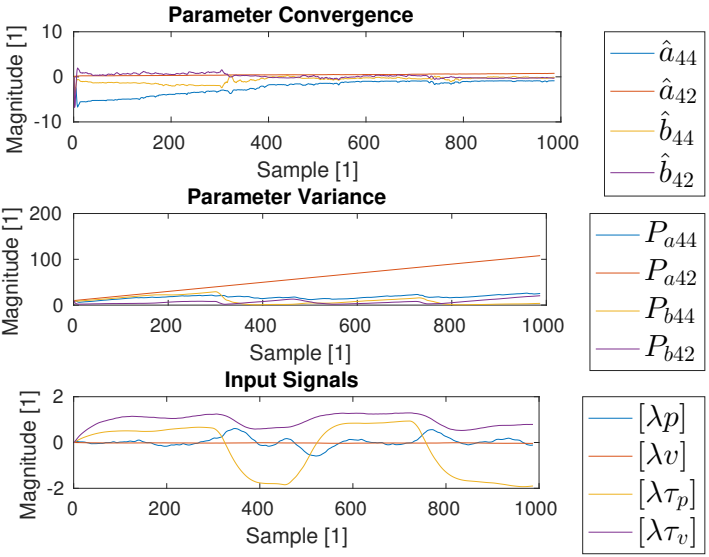

Figure 4.40 Parameter estimates as a function of time, where the estimates were produced using a Kalman filter. The data was obtained as the dynamic experiment in the roll degree of freedom for u= 3.5 knts.

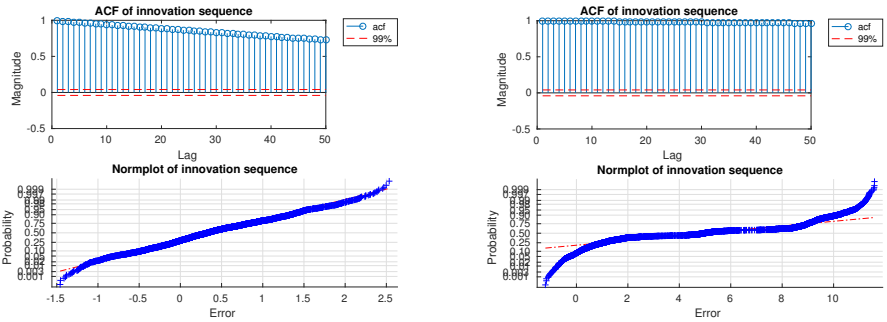

(a) Longitudinal (b) Lateral

Figure 4.41 Estimated autocorrelation function of simulated noise sequence in forward and lateral velocity. The norm plot of the innovation sequence is also provided.

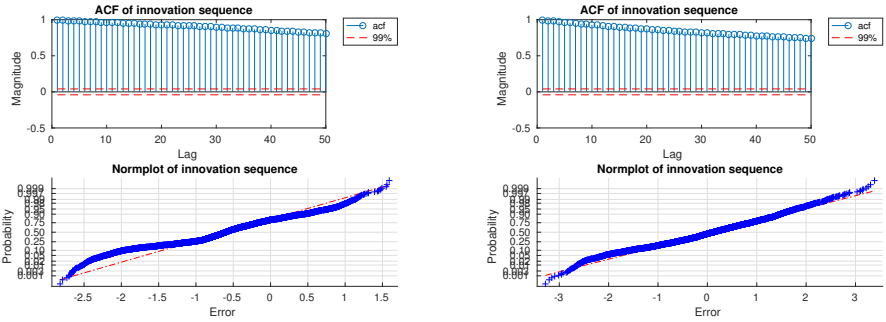

(a) Vertical (b) Roll

Figure 4.42 Estimated autocorrelation functions of simulated noise sequence in vertical and roll velocity. The norm plots of the innovation sequences are also provided.

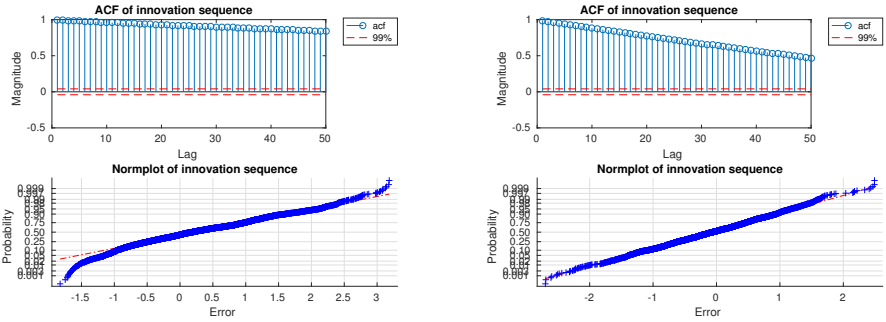

(a) Pitch (b) Yaw

Figure 4.43 Estimated autocorrelation functions of simulated noise sequence in pitch and yaw velocity. The norm plots of the innovation sequences are also provided.

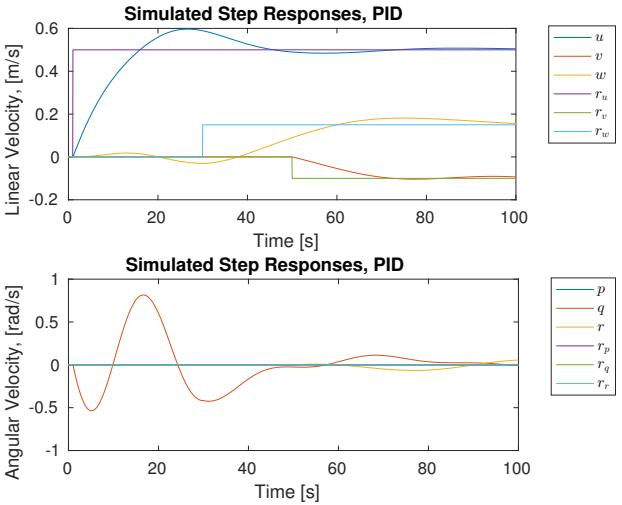

Figure 4.44 Simulated step responses using a PI controller and no measurement noise. Sample time used for the simulation was $h = 0.05$ s.

4.6 Controller Simulations

Note that all simulations described in this section assumes that the effect of the restoring forces and moments vector $g(\eta)$ has been canceled out by a feed-forward controller.

Simulations of closed-loop system responses for two controller structures have been carried out. The closed-loop response of one of the LPV sub-models (corresponding to $u = 2.0$ knts) when controlled using a set of parallel SISO PID regulators are displayed in Figs. 4.44-4.45. When noise was added, the system went unstable.

Figures 4.46-4.47 show the simulated system response for a simulation length of $t = 100$ s. It should be noted that the MPC controller is able to attenuate deviations from the issued angular velocity commands (all being 0 rad/s) effectively.

In the current SROV design, there are two front vertical thruster, but only one aft vertical thruster. By adding an additional aft vertical thruster (all four vertical thrusters symmetrically located around the Center Of Mass), better performance may be achievable. Figures 4.48 and 4.49 show simulation results using the same conditions as before, with the only exception that an additional aft vertical thruster has been added.

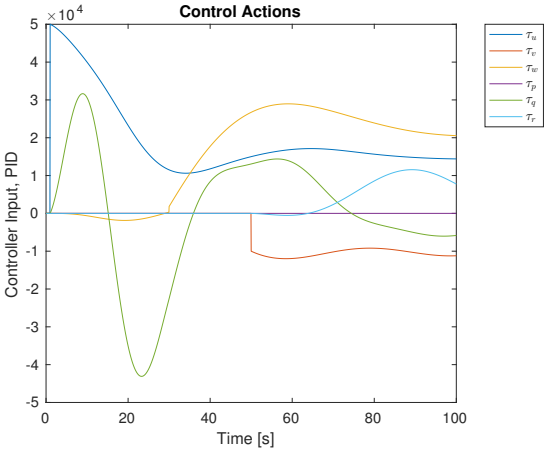

Figure 4.45 Control actions given by the PI controller, no measurement noise present. Sample time used for the simulation was $h = 0.05$ s.

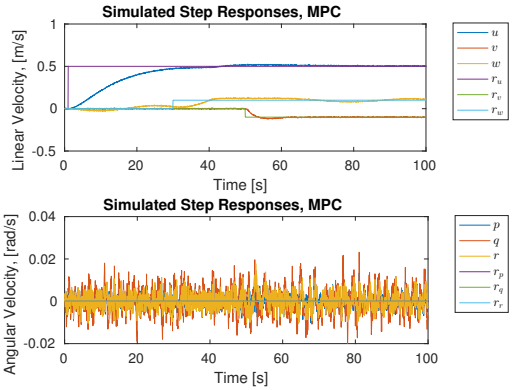

Figure 4.46 Simulated step responses using an MPC controller and measurement noise (zero mean, variance corresponding to that obtained in the experimental data). Prediction horizon was set to $H_p = 20$, and control horizon was set to $H_u = 14$ samples. The system was simulated using a sample period of $h = 0.05$ s. The constraints on the control inputs have been set to mirror the real constraints imposed by the SROV thruster models.

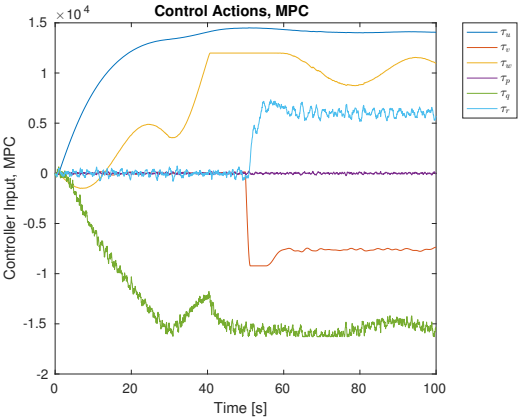

Figure 4.47 Simulated step responses using an MPC controller and measurement noise (zero mean, variance corresponding to that obtained in the experimental data). Prediction horizon was set to $H_p = 20$, and control horizon was set to $H_u = 14$ samples. The system was simulated using a sample period of $h = 0.05$ s. The constraints on the control inputs have been set to mirror the real constraints imposed by the SROV thruster model.

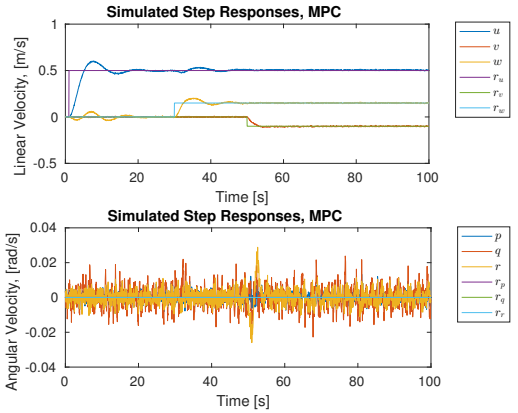

Figure 4.48 Simulated step responses using an MPC controller and measurement noise (zero mean, variance corresponding to that obtained in the experimental data). Prediction horizon was set to $H_p = 20$, and control horizon was set to $H_u = 14$ samples. The system was simulated using a sample period of $h = 0.05$ s. The constraints on the control inputs reflect the situation when an additional vertical thruster is being used.

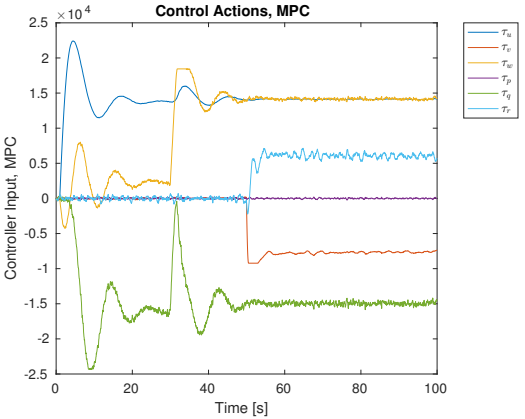

Figure 4.49 Simulated step responses using an MPC controller and measurement noise (zero mean, variance corresponding to that obtained in the experimental data). Prediction horizon was set to $H_p = 20$, and control horizon was set to $H_u = 14$ samples. The system was simulated using a sample period of $h = 0.05$ s. The constraints on the control inputs reflect the situation when an additional vertical thruster is being used.

5

Discussion

5.1 Modeling Results

The first approach pursued in this thesis research, was to use the very rough approximation that the LPV sub-models could be considered decoupled. The resulting NRMSE scores and the number of zero crossings were quite promising. A weakness of the diagonal LPV model was that the predictions produced were only delayed versions of the measured states. In other words, the predictions were (more or less) given by

$$\hat{v}(k+1) = v(k) \tag{5.1}$$

This type of model is clearly inferior for many purposes, including MPC control. The reason that this type of predictions were being produced, is the quite large values populating the added mass matrix M. As discussed in Sec. 2.5, the input signal τ affects the system states through the inverse of M. Thus, a diagonal matrix M with large entries will suppress any input supplied to the system.

The observation that the diagonal LPV models were inferior was further supported by the plots of the autocorrelation functions of the prediction errors. These clearly indicated that there was still some structure in the residual data. Ultimately, the model should take this structure into consideration. Even when one considered that the residuals were not normally distributed (as was clear from the norm plots provided), and that the confidence intervals may because of this be too tight, there is still structure in the prediction errors. It is also clear from some of the experiment data that coupling between some of the states were present. All of these facts implied that a coupled model may achieve better than an uncoupled LPV. Thus, the order of the LPV model was increased by allowing off-diagonal entries in the system matrices.

When the coupled LPV model was evaluated, quite different results were obtained. First of all, the magnitudes of the estimated entries of the LPV model matrices were significantly smaller. This, in turn, rendered in a model better suited to actually predict changes in the states. However, the NRMSE scores were generally slightly lower than in the case of an uncoupled system. Noticeably, the decrease in

fit_u was about 0.1 units. Also, the number of zero crossings were drastically lower in the case of the coupled LPV model. When zooming in on the predictions and the actual states, it is clear that a small offset is present in some of the degrees of freedom. The prediction errors are in other words not zero mean. This may be for several reasons. One possibility is that the experiment durations may have been too short. This would not allow the parameter estimates to converge. A couple of the plotted parameter evolutions (see Figs. 4.39-4.40) suggest that convergence is perhaps not an issue, but that system excitation is a large problem. Parameter covariances increase linearly, indicating bad excitation. Yet another issue is of course that the state dependency of the combined Coriolis and damping matrix is so strong, that the LPV approximation fails for that reason.

The question why the statistic validation methods fail remains unanswered. A few proposals follow. It may be that the SROV dynamics are too non-linear for the proposed LPV structure to be able to approximate the system. As the literature suggests that ROVs are generally highly non-linear systems, it is not a too far fetched thought that also the SROV will be a highly non-linear system. This assumption is also (at least partly) indicated by the weak coherence between inputs and outputs to the system. If this is the case, a possible approach would be to use a finer scheduling grid. This would, however, demand more experiments to be run. There is no guarantee that this approach would work. Another plausible explanation to the poor statistical results, is that some of the collected input-output data is badly corrupted by measurement noise. This is unlikely, as the INS of the SROV is quite accurate. According to the data-sheet of the INS, it should be able to give measurements with an accuracy of 10^{-3} m/s for linear velocities and 10^{-3} rad/s for angular velocities, rendering in a good signal-to-noise ratio. The most likely explanation to the poor statistical results, is that the underlying noise distribution is actually not a white process. As a matter of fact, it is quite likely that the noise and disturbances are non-white. The environment in which the SROV is operating, can be assumed to be affected by ocean currents. These may, in turn, be modeled as slowly varying random walks [Fossen, 1994]. Thus, the prediction errors should not be white but follow the statistics of a random walk. The simulations presented in Figs. 4.41-4.43 show the obtained results when performing simulations as described in Eq. (1.16). These autocorrelations actually resemble those obtained in some of the degrees of freedom using a coupled LPV model, which might indicate a good model fit. In any case, it seems as if the coupled LPV model approximates the behavior of the SROV in a more suitable way than the diagonal LPV models, as these produce inferior predictions.

The SROV control system is updating the control signal at 20Hz. However, the software recording all control actions during the trials had a fixed sample rate of 10Hz. The sampling frequency could not be changed. This means that the control signals observed satisfy

$$\tau(k)_{obs} = \tau(2k)_{real},\ 0,1,\cdots,N \tag{5.2}$$

where N denote the length of the recorded sequence. Of course, this will affect the identification of the system dynamics pursued in this report. First of all, the control actions will change between the entries in the sequence of recorded control actions. This is a problem both in terms of parameter estimation and in terms of predictions. The parameter estimation will suffer from increased levels of uncertainty as the system is responding to input signals unknown to the estimation algorithm. Hopefully, this is not too severe a problem as the system response to high-frequency content is attenuated. This is indicated by the recorded time series and by the transfer function estimates in Appendix 7.4, as these show a roll-off for frequencies above approximately 1Hz. Only low-frequency content of the input signals will have a large effect on the system outputs, and thus the unknown control signals that are actually giving a noticeable effect on the system states might not differ very much from the recorded signals.

When performing predictions of future states, a zero-order-hold approximation has been used. This approximation is violated by the system generating the validation data, as the control actions change in between the samples known to the validation algorithm. It is fair to assume that the prediction results would be more accurate if the intermediate control actions were also known. If for no other reason, the LPV models would have a finer sampled representation of the system states, and the prediction algorithms described in Eqs. (2.14) and (2.16) would have to predict the states a shorter distance into the future. For this reason, the results of the project would likely improve if the sampling frequency of the system was to be increased.

A further issue with the lower than necessary sampling rate, is that the frequency content which the model can be expected to cover is affected. According to the famous Shannon sampling theorem [Johansson, 2017], continuous-time signals sampled using a sample rate F_s will admit a unique frequency representation up to $F_s/2$. Signals at higher frequencies than $F_s/2$ may alias into the frequency region of interest, distorting the frequency content of the discrete-time signal. The proper way of handling aliasing in practice is to incorporate an anti-aliasing filter (which is a low-pass filter). It has in this thesis research been assumed that the ROV dynamics are of low-pass character. This assumption is supported by most of the estimated transfer functions in Appendix 7.4, as discussed above. Thus, the system itself is in a sense a low-pass filter which may alleviate aliasing problems. However, an increased sampling frequency would most likely not hurt the results in terms of aliasing either.

All in all, the under-sampling of the SROV is an error source that has to be considered in this project. If the sampling frequency of the control action logging software was to be increased in the future, it is likely that better results could be obtained. As a final note on the discussion of the sampling rates, one also need to keep in mind that when the sampling time is decreased, the prediction and control horizons of the MPC algorithm need to be modified.

Error Sources

A number of assumptions and uncertainties, that may have effected the results of the project, have been identified. A possibly large source of error, is the fact that the thrusters are being run in open loop. There is, in other words, no way of knowing what the actual control actuation acting on the SROV is. In the project, the control input has been calculated using the thruster data sheets, which provide typical input-output curves. However, this will not alleviate the problems caused by the open-loop operation. Since all estimates are based on the calculated input signals, uncertainties in the parameter estimates will be inevitable. A further issue on the same note, is that predictions are based on the open-loop control signals. As these need not be the actual input signals, prediction errors (affecting the validation process) may arise.

5.2 Controller Simulations

It is very clear that controlling the system described by the identified coupled model is extremely hard when using PID controllers. This is further verified by the currently implemented SROV controller, which is gain scheduled on forward and lateral speeds using a very fine scheduling grid (and consequently many controller parameters). The SROV can, obviously, be stabilized using a gain scheduled PID controller. Little time was for this reason spent on finding suitable controller parameters. However, the results in Sec. 4.6 show what typical limits may be expected by a parallel SISO PID controller structure. First of all, the control signals are discontinuous, and change at very high rates. The hydraulic system of the SROV would not be able to follow such a reference, as changing the differential pressure over a thruster involves moving hydraulic fluid. This takes time, and can't be done in the way suggested in Fig. 4.45. Further on, the PID regulator does not consider limits on the magnitude of the control input. It is thus quite possible that the PID regulated system saturates, which is undesirable for many reasons. This problem has been noted on numerous occasions during survey operations with the SROV. Lastly, the fact SISO PID controllers are unable to suppress the coupling of the identified SROV model is clear from Fig. 4.44. At $t = 1$ s, a reference step in forward velocity is applied. This causes large deviations in pitch angular velocity, and small deviations in vertical velocity. There is no way of handling this coupling, other than by tuning the controller parameters. This is a cumbersome task, and is made even more difficult when measurement noise and load disturbances are considered.

An MPC approach is able to handle all of the shortcomings of the PID structure. Limits on the control signals and their derivatives may be included in the controller description. By using the weight matrices described in Sec. 1.4, it is possible to tune the closed-loop responses based on what states are deemed more important. The MPC structure can also handle the coupled states of the SROV, and noise models may be incorporated in the structure. It is also possible, as shown in the simulation results, to augment the MPC with integral states in order to avoid stationary errors.

The main challenge of using an MPC design, is to obtain the actual model on which the controller is based.

A brief discussion on the simulated closed-loop responses using an MPC follows. The responses in some of the degrees of freedom exhibit damped oscillations when the set-point is changed. This problem may be alleviated by tuning the weights on state errors and control inputs further. One could also try to change the prediction and control horizons. However, a fundamental limit to the actuation of the SROV is posed by the limited actuation capabilities in the vertical direction.

5.3 Future Work

During the course of the thesis research, some scopes have been left out. The reasons have been multiple. Sometimes, time consumption of an extended scope has made such endeavors infeasible. On other occasions, limits have been imposed by the existing technology. In any case, some topics have been identified as possible future work, which would most likely improve on the results already achieved in the current project.

Thruster Actuation

The most obvious limitation to the current project, is the fact that all actuation of the SROV is being run in open-loop. That is, the control system outputs a signal to each thruster, but does not make sure that the output is what it should be. This, of course, poses a number of difficulties both in the case of control and that of identification. Ultimately, the thrusters themselves should be considered a control system, and should be operated in closed loop (taking as reference signal the output from the SROV control system). In order to do this, it would probably be a good idea to build models of the thrusters. It is of course possible to operate the thrusters in closed loop without any knowledge of a mathematical model, but it is quite likely that performance is increased by modeling the thrusters. This is not a new idea, and has been shown to work in [Natarajan et al., 2012][Fossen, 1994]. Once a thruster model is obtained, a cascaded control system with thrusters operating in an inner control loop at higher sampling rates is likely to increase the overall performance.

Another possible improvement to the current thruster actuation, is to reconsider how the actions for each thruster are being decided upon by the controller. Currently, for each thruster, each automatic function has its' own controller. The sum of all outputs of all controllers for each thruster is calculated and output to the thruster. An alternative approach would be to calculate the total command in each freedom degree (this signal is calculated already), and distribute the control action on the thrusters based on the thruster map. This allows for optimisation, as discussed in [Fossen, 1994]. On the same note, it may be a good idea to investigate the thruster map (see Eq. (1.7)) thoroughly.

Additional States

Some assumptions were made at an early stage of the project. After the interview with the control engineer at Kystdesign, it was decided that the effect of the tether should be kept as constant as possible by keeping θ_{TA} constant, and by having a constant amount of tether in the water (θ_{TA} is described in Fig. 1.5). This is a very limiting assumption, as normal survey conditions include operation at various depths and with the SROV moving in relation to the vessel. A possible generalization of the identified LPV model, is to include θ_{TA} in the LPV model. This would of course require additional sensors to be fitted to the SROV, and new identification experiments would have to be carried out.

Changes to the Control System

The simulations of the MPC structure, show that a lot of additional performance may be gained if one vertical thruster is added to the current thruster configuration. The additional thruster would be placed in the aft, and the already existing moved such that all four vertical thrusters are symmetrically positioned around the COG. This change would increase the available control action in the vertical direction, as well as in roll and in pitch. The current design is limited by the non-symmetric vertical thruster configuration. If the vertical velocity is to be changed, only half of the available power of the front thrusters may be used, as a moment around the y-axis would otherwise be generated. Similarly, only some of the available front thruster power may be be used to create a roll moment. This problem is alleviated by the proposed design change, and better closed-loop performance can be achieved as shown in Sec. 4.6.

For high forward velocities, it gets increasingly hard to actuate some of the degrees of freedom using the thrusters. It would in that case be advisable to use rudders rather than the thruster for actuation. One could, in that case, use a penalty on the use of thrusters to force the control system to use the rudders. This would further relieve the hydraulic system, which currently risks saturating.

6

Conclusions

A model with potential of describing the SROV has been identified. Two different approaches to the problem of estimating the parameters of the model were proposed. Experiments to facilitate the two approaches were consequently designed. One of the schemes turned out to be infeasible in real life, as it was difficult to obtain certain behavior assumed by the experiment plan. The experiments for the other approach, could partly be performed.

Model parameters have been estimated using input-output data obtained during a trial on Stril Explorer. Due to the implementation of the actuation of the system, coherence is sometimes weak. This may explain some of the difficulties that the LPV model experiences. The efforts to approximate the SROV as a decoupled system showed that this approach is infeasible. The resulting predictions were only delayed versions of the actual states. This conclusion holds true regardless of what estimation technique is being used, implying that the approximation of a decoupled system is too crude.

As a continuation of the modeling efforts, a coupled LPV model was estimated. The properties of this model were promising, but not perfect. The coupled model was superior when following changing states, but a slight bias made some of the scores go down.

Using the identified LPV model as the the plant, and a perturbed version of the LPV model to initialize an MPC controller, gave promising results in simulation. The MPC controller was able to follow reference changes under the influence of noise and load disturbances. Deviations from the yaw velocity set point could be attenuated, which was one of the aims of the project.

Bibliography

Chou, C., M. Verhaegen, and R. Johansson (1999). "Continuous-time identification of siso systems using laguerre functions". *IEEE Transactions on Signal Processing*, pp. 349–362.

Feng, Z.-p. and R. Allen (2010). "H-infinity autopilot design for autonomous underwater vehicles". *Journal of Shanghai Jiaotong university (Science)* **15** (2), pp. 194–198. URL: https://doi.org/10.1007/s12204-010-9528-1.

Fossen, T. (1994). *Guidance and Control of Ocean Vehicles*. John Wiley & Sons, Chichester.

Hayatolgheibi, M. and A. Mazinan (2017). "Heading angle and depth control of micro-rovs using adaptive minimum-degree pole placement (mdpp) approach." *Marine Systems and Ocean Technology* **12** (13), pp. 13–28. URL: https://link.springer.com/journal/40868/12/1/page/1.

Jakobsson, A. (2015). *An Introduction to Time Series Modeling*. Studentlitteratur, Malmö.

Johansson, R (1994). "Identification of continuous-time models". *IEEE Transactions on Signal Processing* **42** (4), pp. 887–897.

Johansson, R., M. Verhaegen, and C. Chou (1999). "Stochastic theory of continuous-time state-space identification". *IEEE Transactions on Signal Processing* **47**, pp. 41–51.

Johansson, R. (2015). *Predictive and Adaptive Control*. Department of Automatic Control, Faculty of Engineering, Lund University, Lund.

Johansson, R. (2017). *System Modeling & Identification*. Prentice Hall, Englewood Cliffs, NJ.

Ljung, L. (1987). *System Identification: Theory for the User*. Prentice Hall, Englewood Cliffs, NJ.

Ljung, L. (2009). *Continuous-time gray-box identification of mechanical systems using subspace-based identification methods*. URL: http://www.control.isy.liu.se/research/reports/2009/2907.pdf.

Natarajan, S., C. Gaudig, and M. Hildebrandt (2012). "Offline experimental parameter identification using on-board sensors for an autonomous underwater vehicle." In: *2012 Oceans*. IEEE, pp. 1–8. URL: ieeexplore.ieee.org/document/6404905.

Olofsson, B., O. Sörnmo, A. Robertsson, and R. Johansson (2014). "Continuous-time gray-box identification of mechanical systems using subspace-based identification methods". In: *[Host publication title missing]*. IEEE–Institute of Electrical and Electronics Engineers Inc., pp. 327–333.

Rao, G. and H. Unbehauen (2006). "Identification of continuous-time systems". *IEEE Proceedings – Control Theory & Applications* **153** (2), pp. 185–220.

Sangrok, J., K. Jihoon, K. Jong-Won, B. JangHo, B. Jeongae, K. Jongwon, and S. TaeWon (2015). "Back-stepping control design for an underwater robot with tilting thrusters." In: *2015 International Conference on Advanced Robotics (ICAR)*. IEEE, pp. 1–8. URL: ieeexplore.ieee.org/document/7251425.

Tiano, A., R. Sutton, A. Lozowicki, and W Naeem (2007). "Observer kalman filter identification of an autonomous underwater vehicle". *Control Engineering Practice* **15** (6), pp. 727–739. URL: https://www.sciencedirect.com/science/article/pii/S0967066106001304.

You, H., M. Kwong, M. Chitre, and M. Kien (2016). "Online system identification of an autonomous underwater vehicle via in-field experiments". *IEEE Journal of Oceanic Engineering* **41** (1), pp. 5–17. URL: http://ieeexplore.ieee.org/document/7054571/.

Åkesson, J. (2018). URL: www.control.lth.se/Research/tools/mpctools.html.

7

Appendicies

7.1 Transformation Derivation

Given is a state-space model on the form

$$\dot{x}(t) = Ax(t) + Bu(t) \tag{7.1}$$

A Laplace tranform (ignoring initial conditions) give

$$sX(s) = AX(s) + BU(s) \tag{7.2}$$

The transform

$$\lambda(s) = \frac{1}{1+sT},\ T > 0 \tag{7.3}$$

may be reformulated as

$$s = \frac{1}{T}\frac{1-\lambda(s)}{\lambda(s)} \tag{7.4}$$

By substituting Eq. (7.4) into Eq. (7.2), one obtains

$$\frac{1}{T}\frac{1-\lambda(s)}{\lambda(s)}X(s) = AX(s) + BU(s) \tag{7.5}$$

$$\Leftrightarrow \tag{7.6}$$

$$X(s) = TA[\lambda X(s)] + TB[\lambda U(S)] + [\lambda X(s)] \tag{7.7}$$

$$\Leftrightarrow \tag{7.8}$$

$$X(s) = (I + TA)[\lambda X(s)] + TB[\lambda U(s)] \tag{7.9}$$

$$= A_\lambda[\lambda X(s)] + B_\lambda[\lambda U(s)] \tag{7.10}$$

Thus, the original matrices A and B may be obtained using the relation

$$A = (A_\lambda - I)/T \tag{7.11}$$

$$B = B_\lambda/T \tag{7.12}$$

since Eq. (7.3) requires $T > 0$.

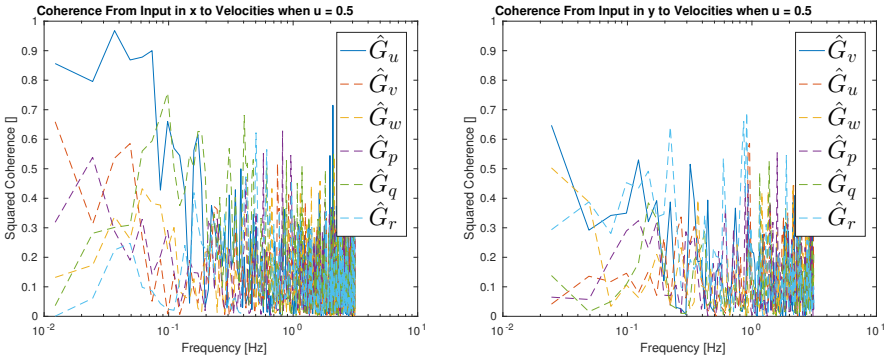

Figure 7.1 Figures showing coherence for different input-output configurations when $u = 0.5$ knts.

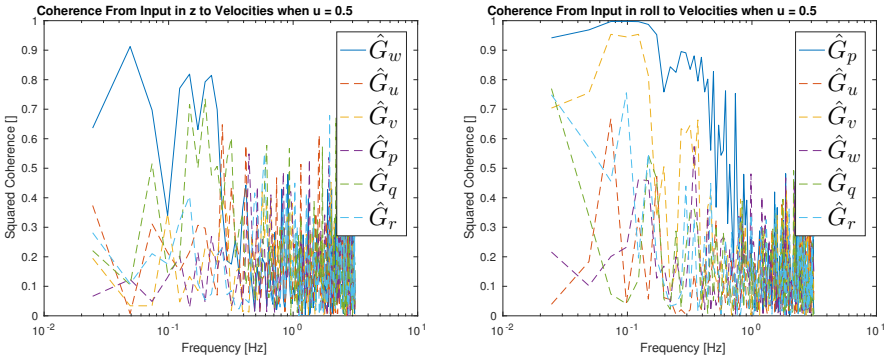

Figure 7.2 Figures showing coherence for different input-output configurations when $u = 0.5$ knts.

7.2 Coherence Spectra

In this appendix, the coherence spectra obtained as a result of the input-output data validation are presented. Note that the subscripts in the legend of the diagrams indicate what output data was considered. For instance, the left diagram of Fig. 7.1 shows the resulting coherence from input in forward velocity (as indicated in the title of the figure, as well as in the sub caption) to all measured output velocities. The legend $\hat{G}_v$ thus denotes the estimated squared coherence from input u to output v (i.e., measured lateral velocity). All other legends should be interpreted similarly.

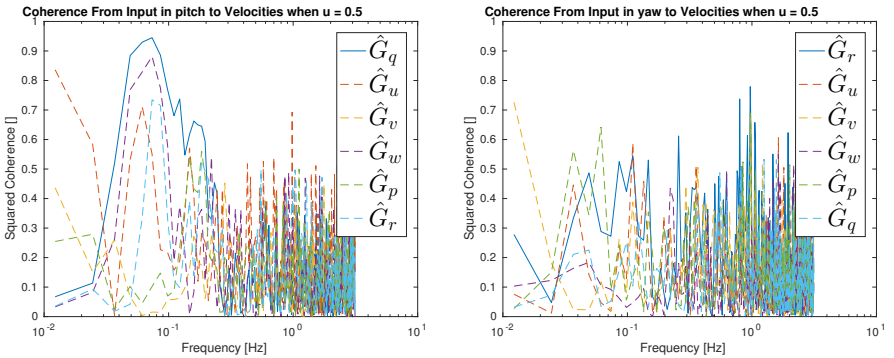

Figure 7.3 Figures showing coherence for different input-output configurations when $u = 0.5$ knts.

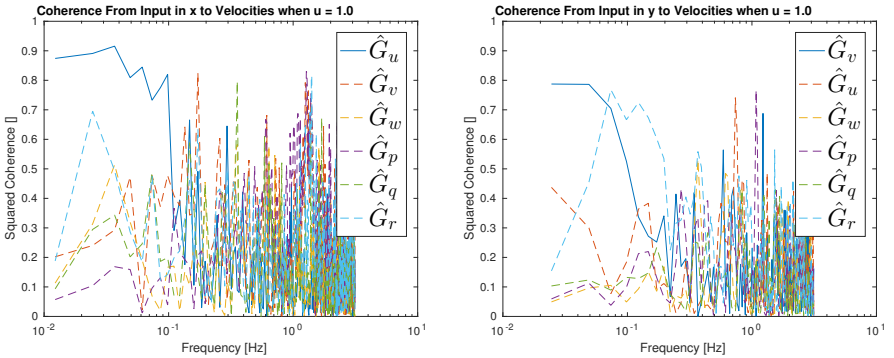

Figure 7.4 Figures showing coherence for different input-output configurations when $u = 1.0$ knts.

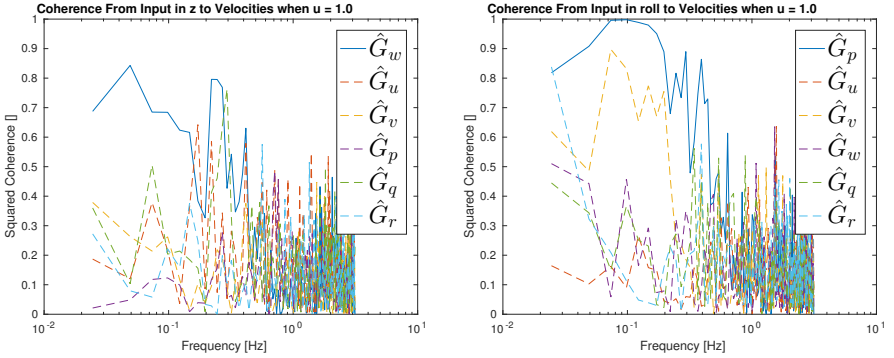

Figure 7.5 Figures showing coherence for different input-output configurations when $u = 1.0$ knts.

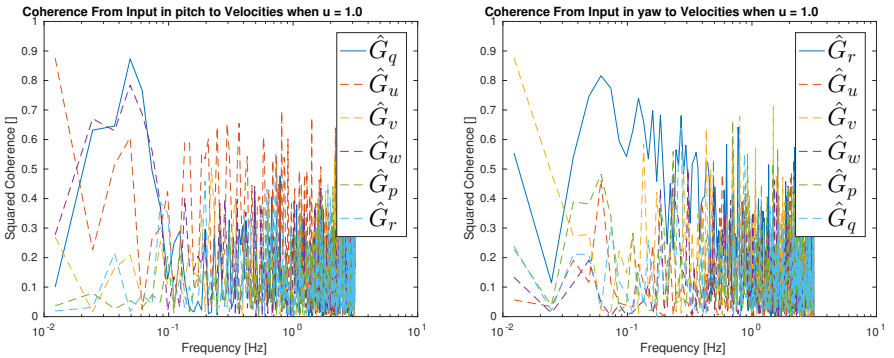

Figure 7.6 Figures showing coherence for different input-output configurations when $u = 1.0$ knts.

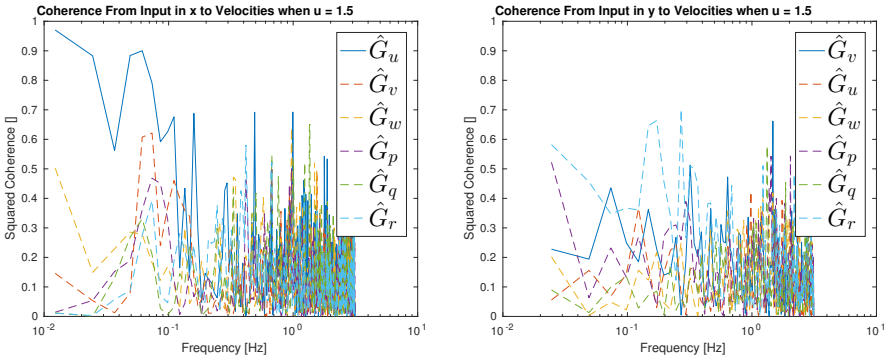

Figure 7.7 Figures showing coherence for different input-output configurations when $u = 1.5$ knts.

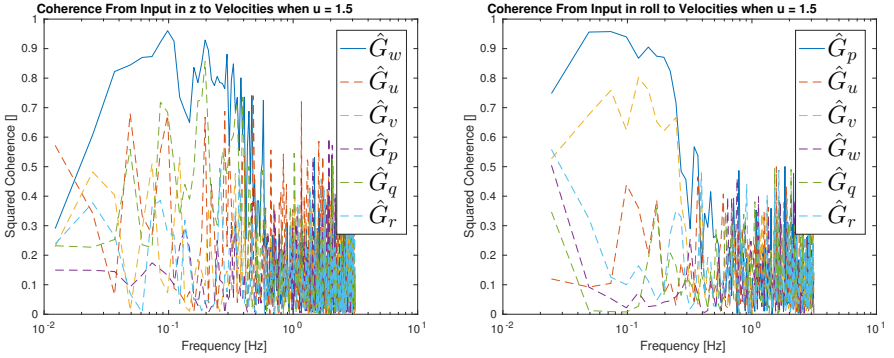

Figure 7.8 Figures showing coherence for different input-output configurations when $u = 1.5$ knts.

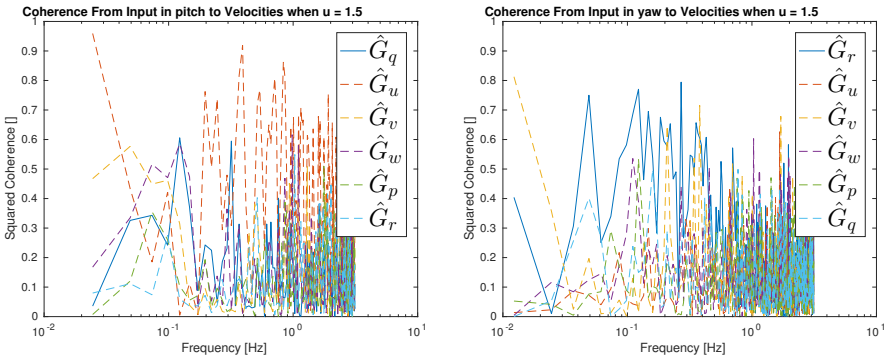

Figure 7.9 Figures showing coherence for different input-output configurations when $u = 1.5$ knts.

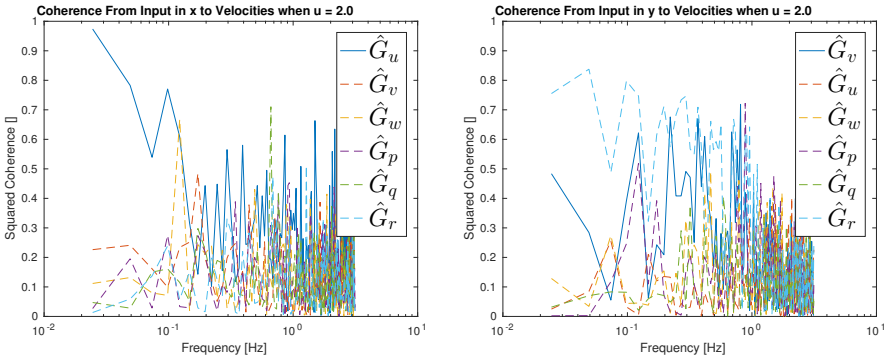

Figure 7.10 Figures showing coherence for different input-output configurations when $u = 2.0$ knts.

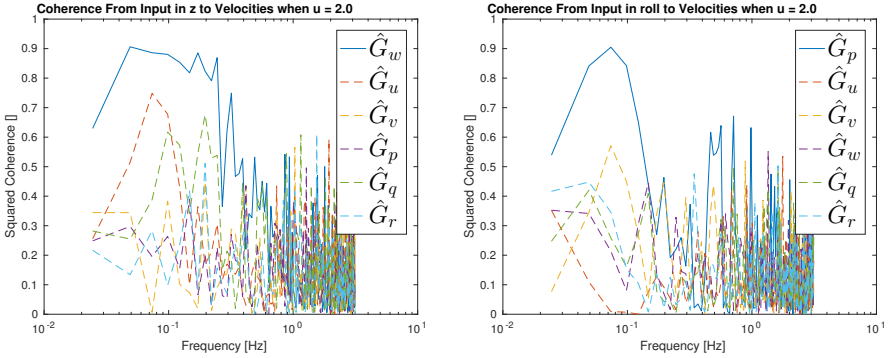

Figure 7.11 Figures showing coherence for different input-output configurations when $u = 2.0$ knts.

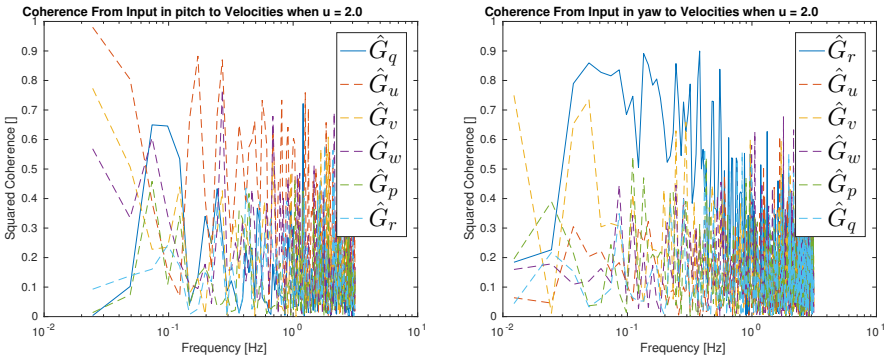

Figure 7.12 Figures showing coherence for different input-output configurations when $u = 2.0$ knts.

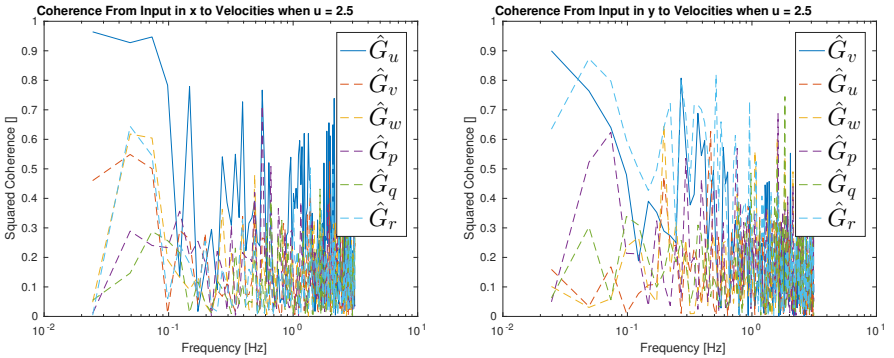

Figure 7.13 Figures showing coherence for different input-output configurations when $u = 2.5$ knts.

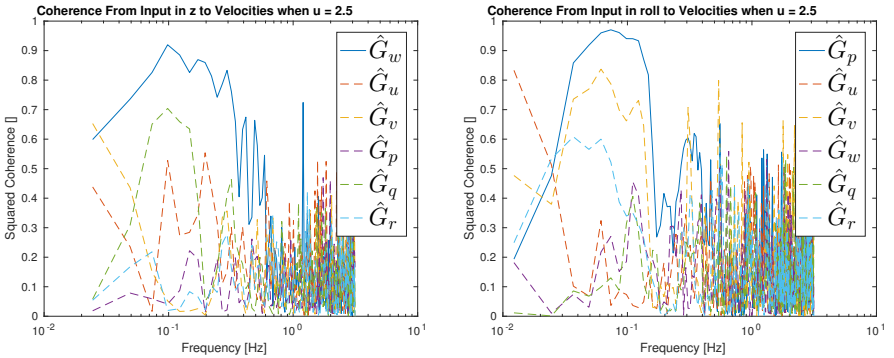

Figure 7.14 Figures showing coherence for different input-output configurations when $u = 2.5$ knts.

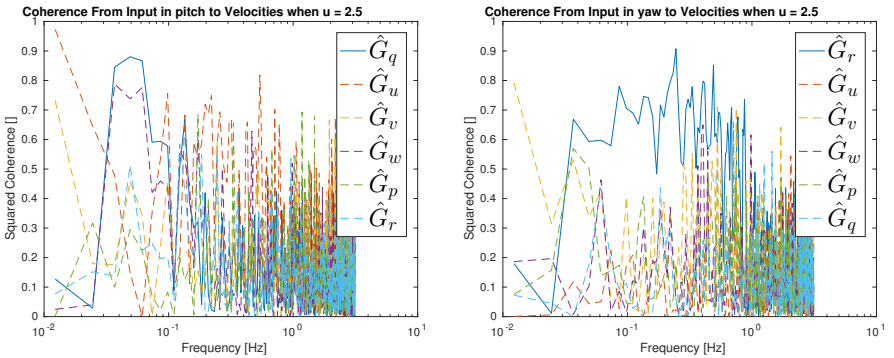

Figure 7.15 Figures showing coherence for different input-output configurations when $u = 2.5$ knts.

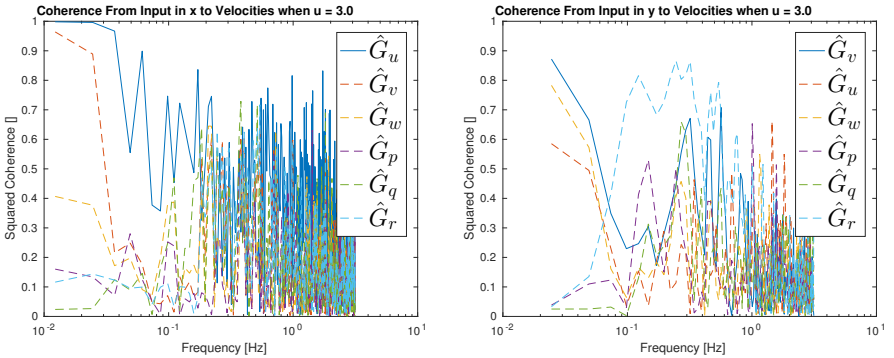

Figure 7.16 Figures showing coherence for different input-output configurations when $u = 3.0$ knts.

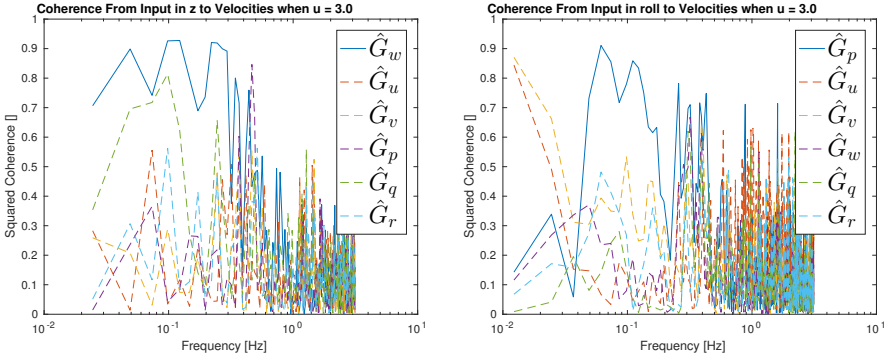

Figure 7.17 Figures showing coherence for different input-output configurations when $u = 3.0$ knts.

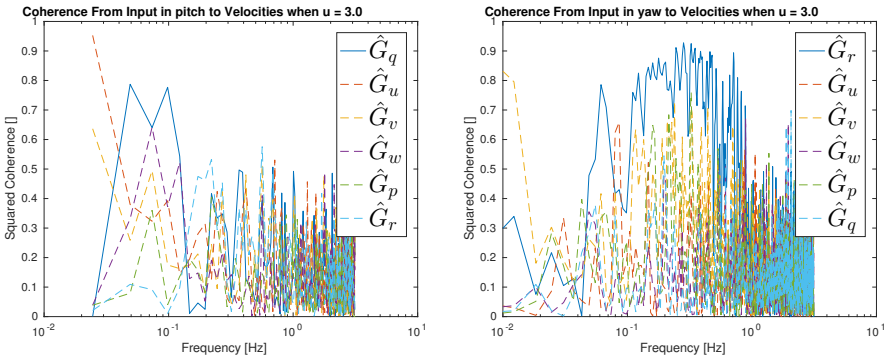

Figure 7.18 Figures showing coherence for different input-output configurations when $u = 3.0$ knts.

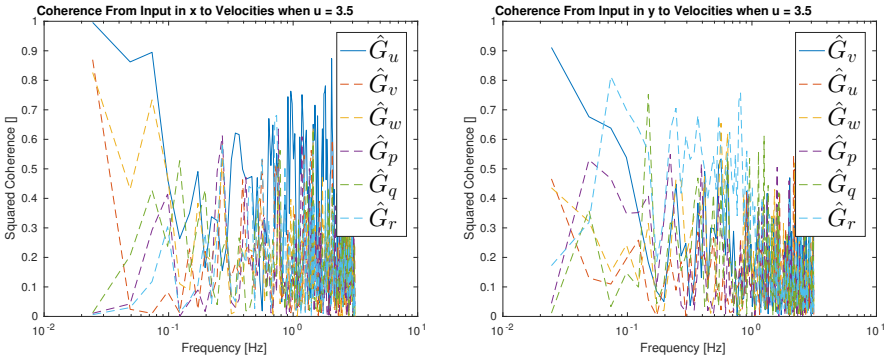

Figure 7.19 Figures showing coherence for different input-output configurations when $u = 3.5$ knts.

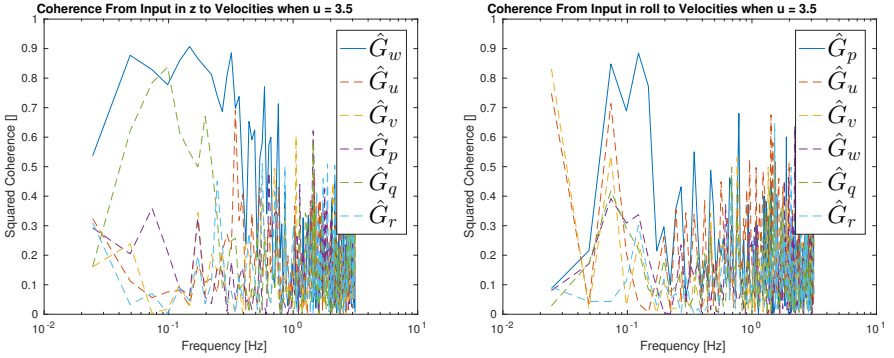

Figure 7.20 Figures showing coherence for different input-output configurations when $u = 3.5$ knts.

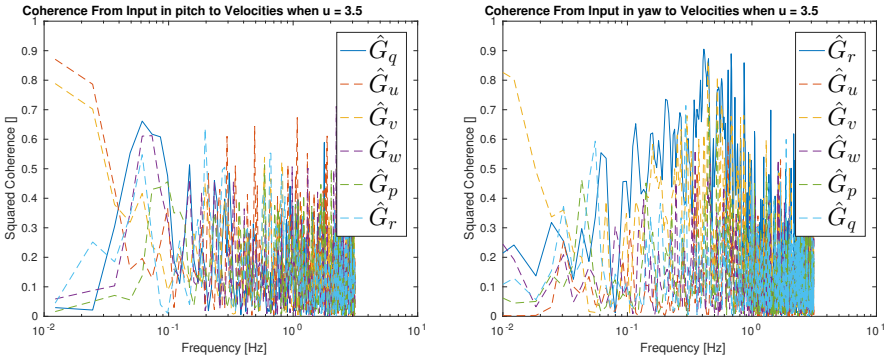

Figure 7.21 Figures showing coherence for different input-output configurations when $u = 3.5$ knts.

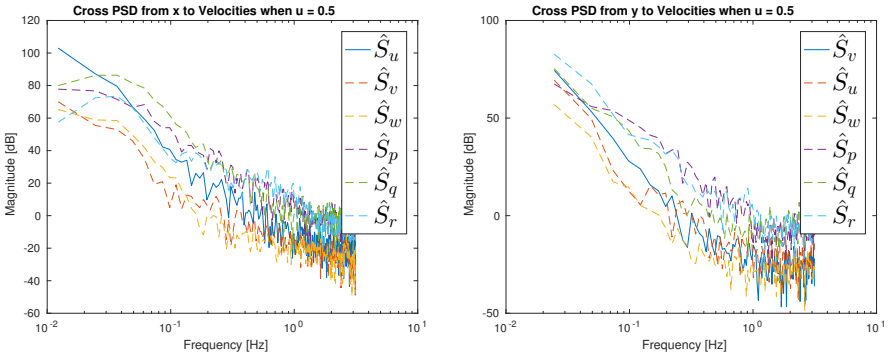

Figure 7.22 Figures showing PSD for different input-output configurations when $u = 0.5$ knts.

7.3 Cross PSD

In this appendix, the PSD spectra obtained as a result of the input-output data validation are presented. Note that the subscripts in the legend of the diagrams indicate what output data was considered. For instance, the left diagram of Fig. 7.22 shows the resulting PSD from input in forward velocity (as indicated in the title of the figure, as well as in the subcaption) to all measured output velocities. The legend $\hat{S}_v$ thus denotes the estimated squared PSD from input u to output v (i.e., measured lateral velocity). All other legends should be interpreted similarly.

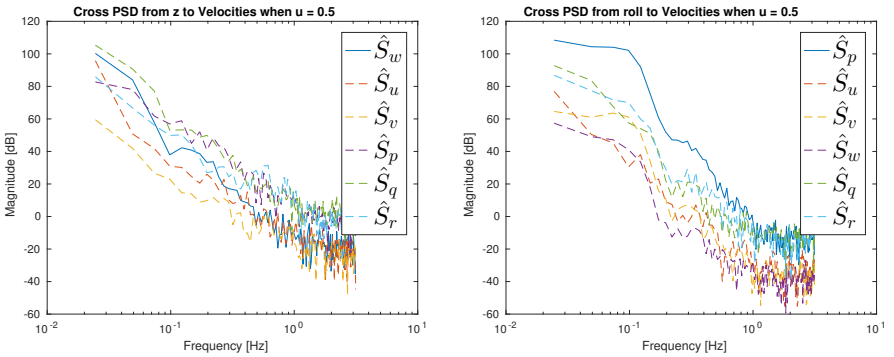

Figure 7.23 Figures showing PSD for different input-output configurations when $u = 0.5$ knts.

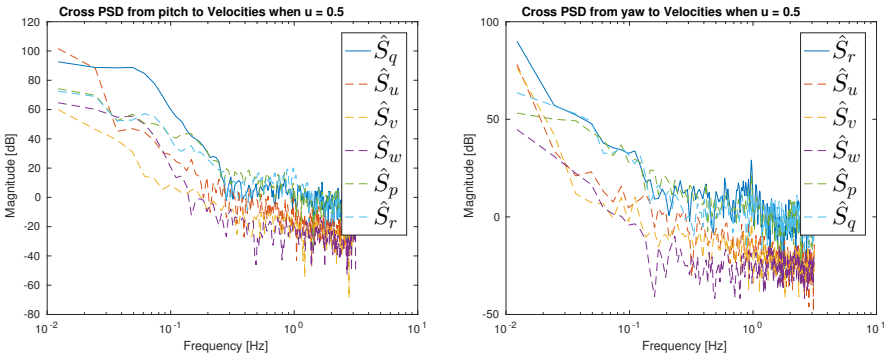

Figure 7.24 Figures showing PSD for different input-output configurations when $u = 0.5$ knts.

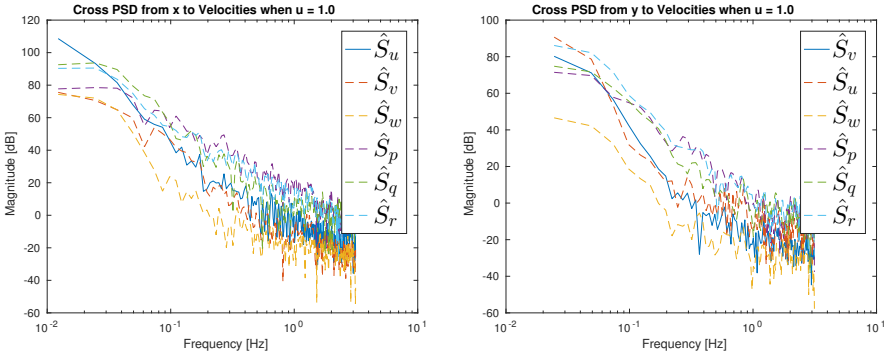

Figure 7.25 Figures showing PSD for different input-output configurations when $u = 1.0$ knts.

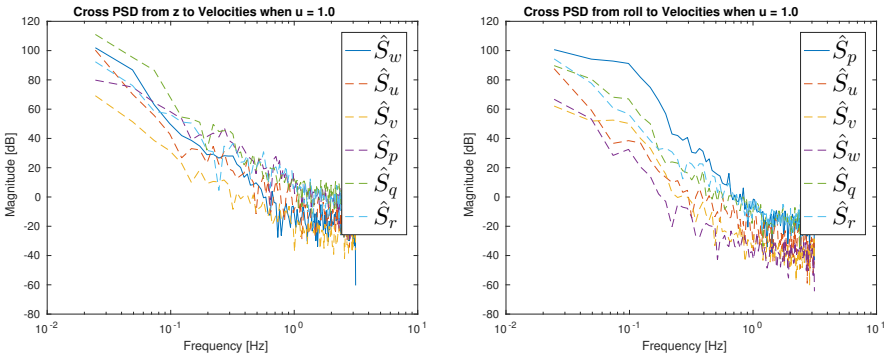

Figure 7.26 Figures showing PSD for different input-output configurations when $u = 1.0$ knts.

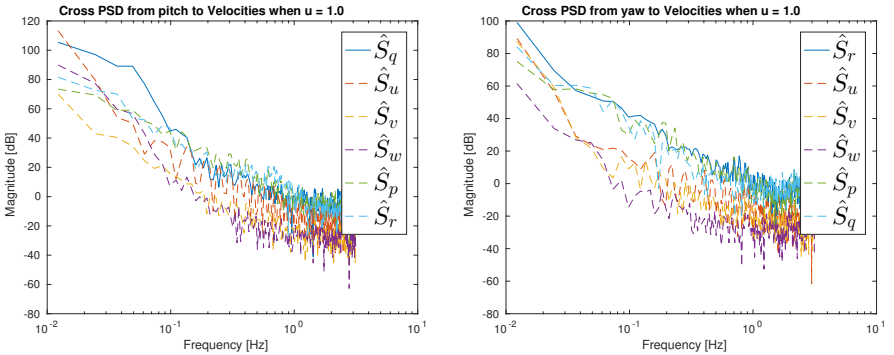

Figure 7.27 Figures showing PSD for different input-output configurations when $u = 1.0$ knts.

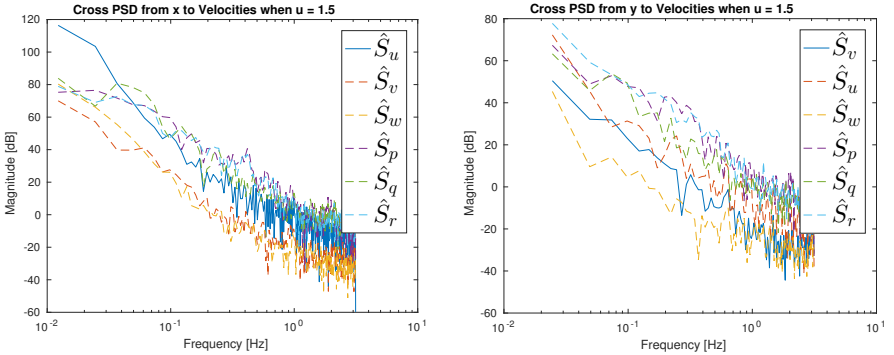

Figure 7.28 Figures showing PSD for different input-output configurations when $u = 1.5$ knts.

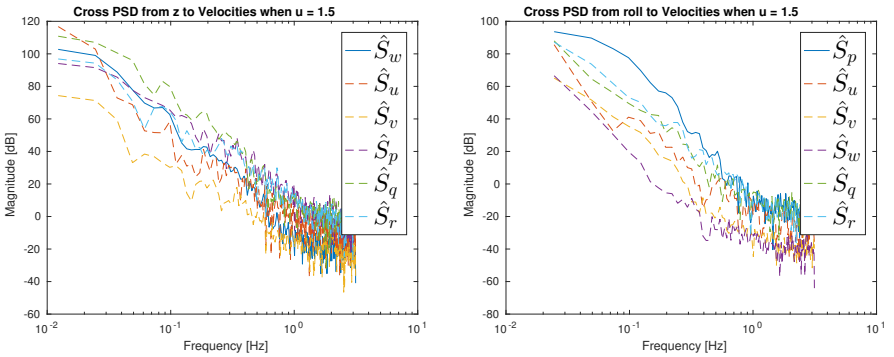

Figure 7.29 Figures showing PSD for different input-output configurations when $u = 1.5$ knts.

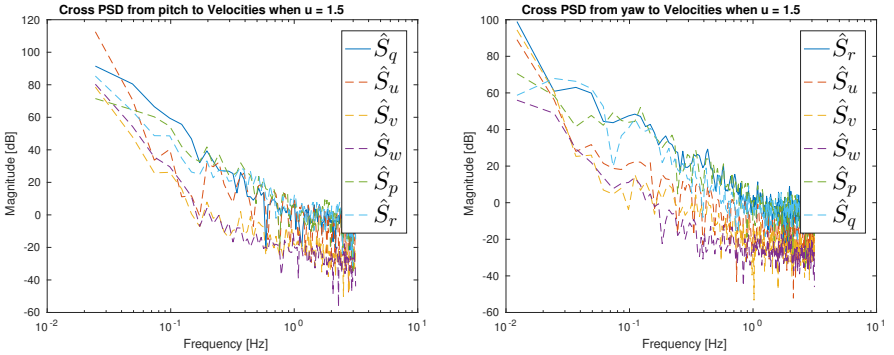

Figure 7.30 Figures showing PSD for different input-output configurations when $u = 1.5$ knts.

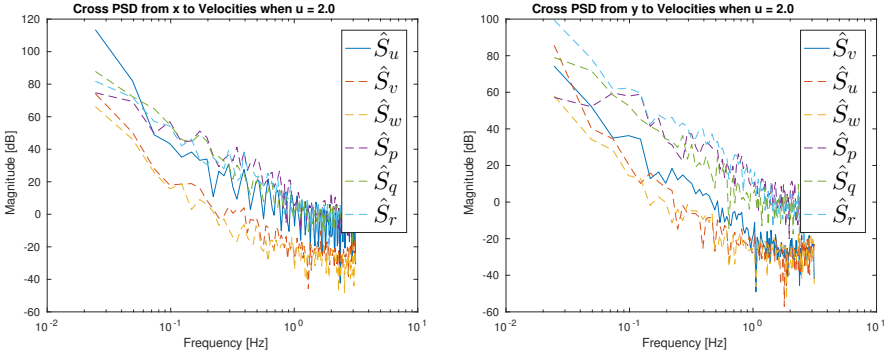

Figure 7.31 Figures showing PSD for different input-output configurations when $u = 2.0$ knts.

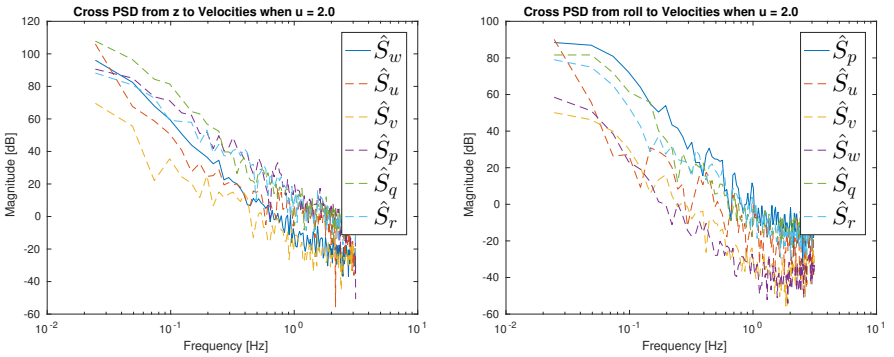

Figure 7.32 Figures showing PSD for different input-output configurations when $u = 2.0$ knts.

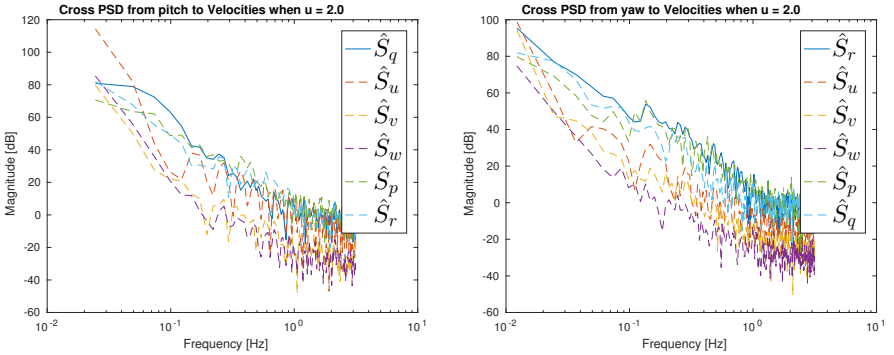

Figure 7.33 Figures showing PSD for different input-output configurations when $u = 2.0$ knts.

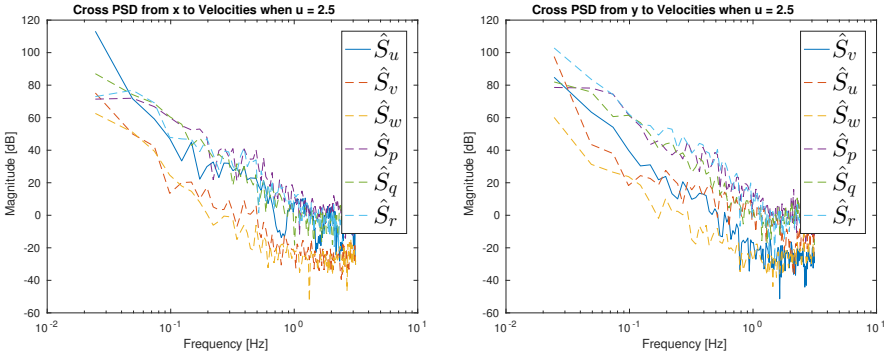

Figure 7.34 Figures showing PSD for different input-output configurations when $u = 2.5$ knts.

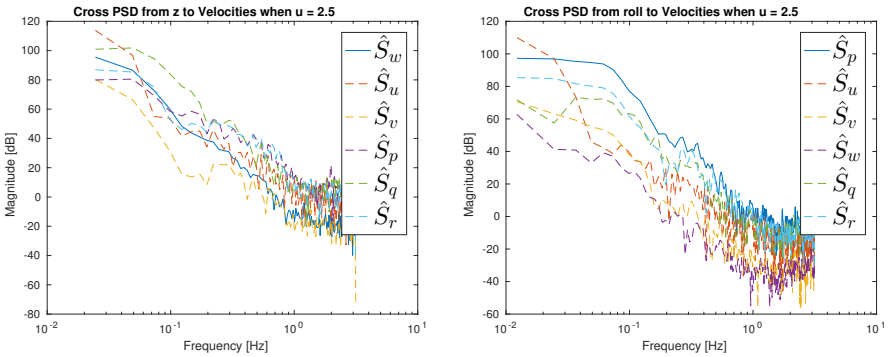

Figure 7.35 Figures showing PSD for different input-output configurations when $u = 2.5$ knts.

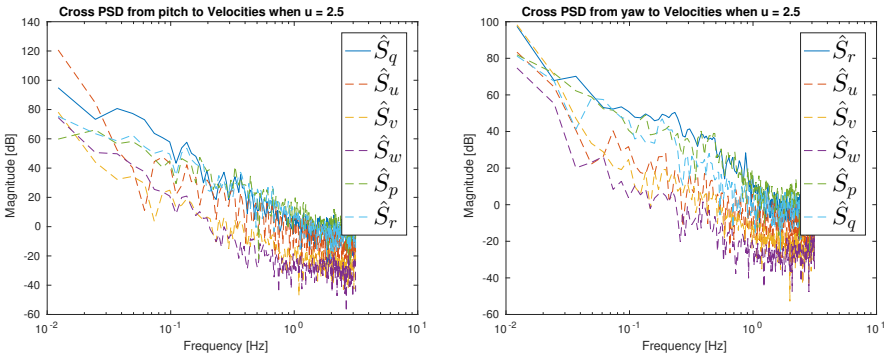

Figure 7.36 Figures showing PSD for different input-output configurations when $u = 2.5$ knts.

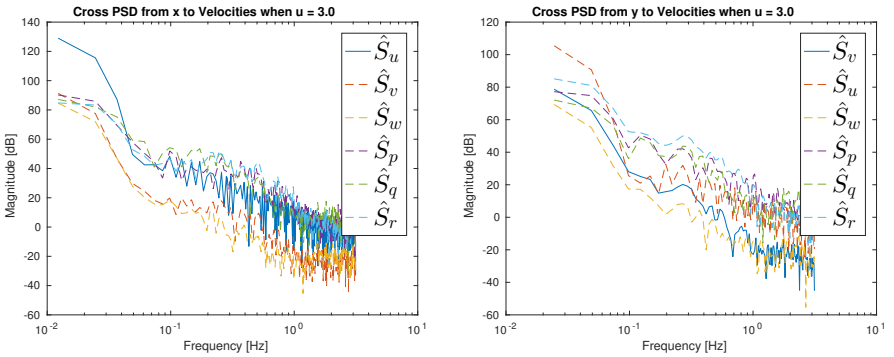

Figure 7.37 Figures showing PSD for different input-output configurations when $u = 3.0$ knts.

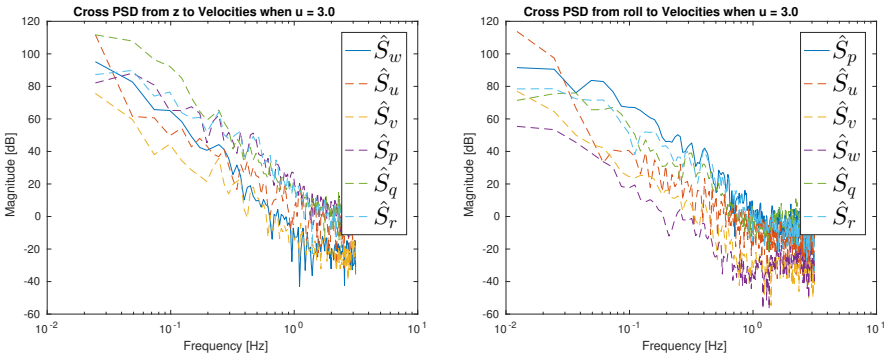

Figure 7.38 Figures showing PSD for different input-output configurations when $u = 3.0$ knts.

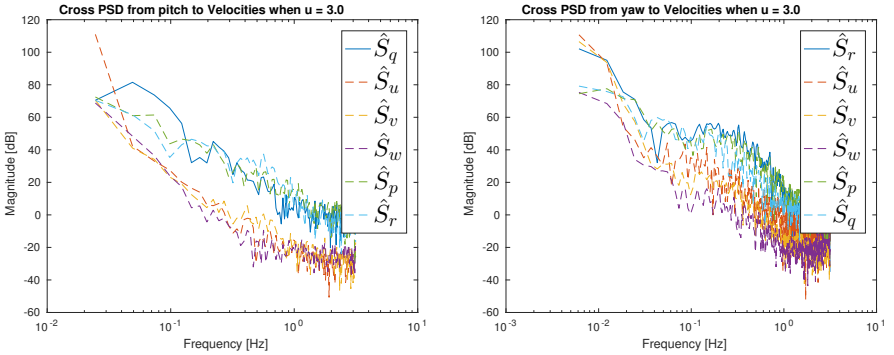

Figure 7.39 Figures showing PSD for different input-output configurations when $u = 3.0$ knts.

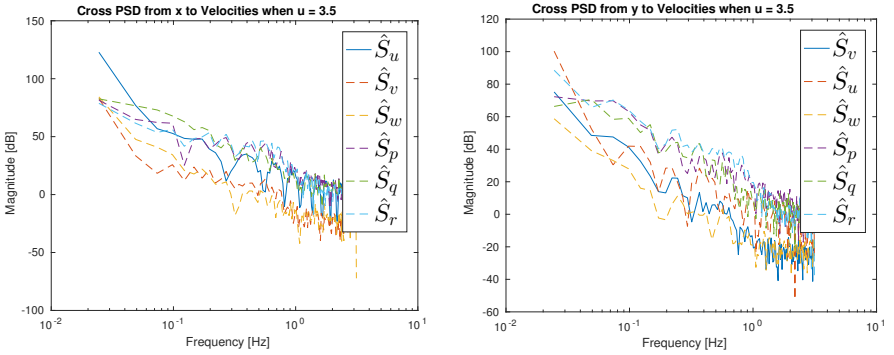

Figure 7.40 Figures showing PSD for different input-output configurations when $u = 3.5$ knts.

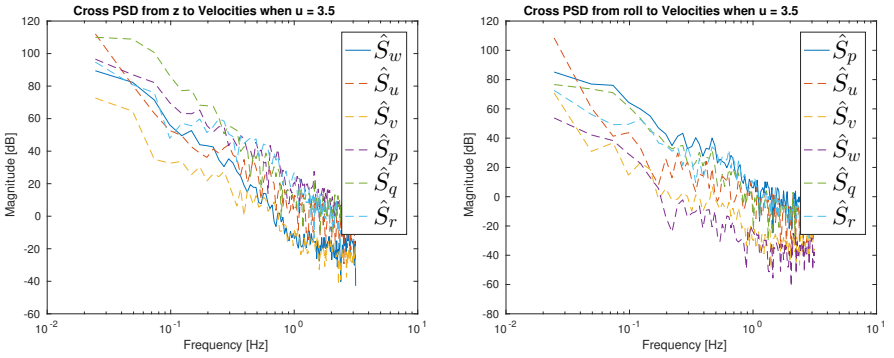

Figure 7.41 Figures showing PSD for different input-output configurations when $u = 3.5$ knts.

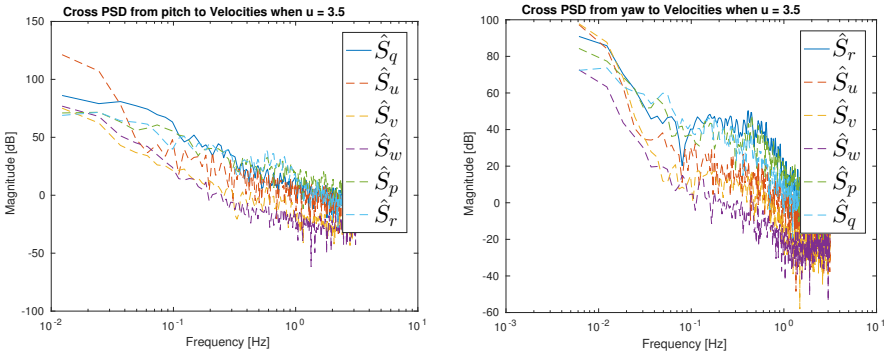

Figure 7.42 Figures showing PSD for different input-output configurations when $u = 3.5$ knts.

7.4 Transfer Functions

In this appendix, the estimated transfer functions obtained as a result of the input-output data validation are presented. Note that the subscripts in the legend of the diagrams indicate what output data was considered. For instance, the left diagram of Fig. 7.43 shows the resulting TF from input in forward velocity (as indicated in the title of the figure, as well as in the subcaption) to all measured output velocities. The legend $\hat{H}_v$ thus denotes the estimated squared TF from input u to output v (i.e., measured lateral velocity). All other legends should be interpreted similarly.

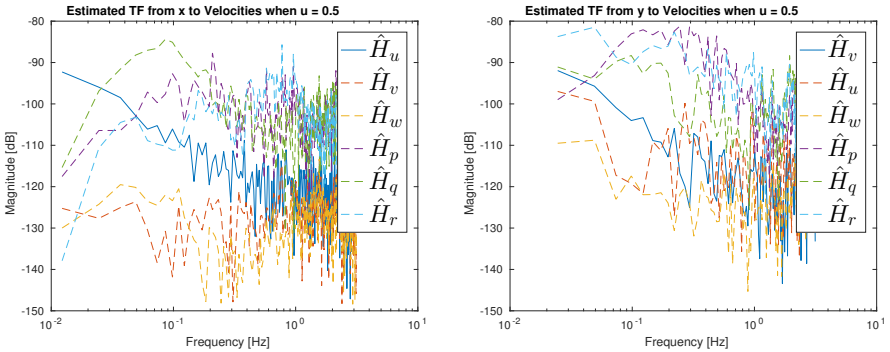

Figure 7.43 Figures showing TF for different input-output configurations when $u = 0.5$ knts.

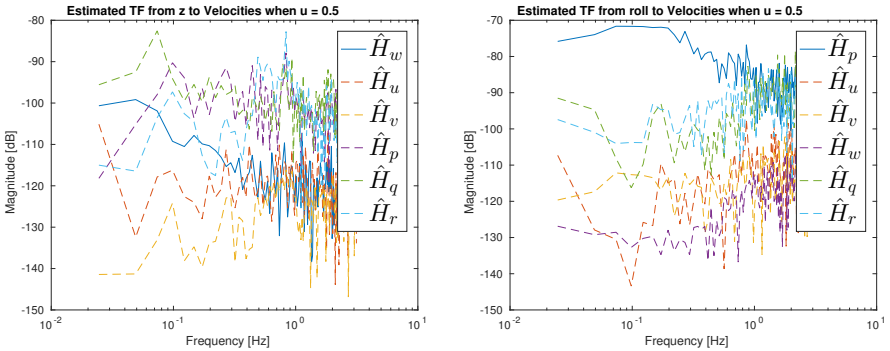

Figure 7.44 Figures showing TF for different input-output configurations when $u = 0.5$ knts.

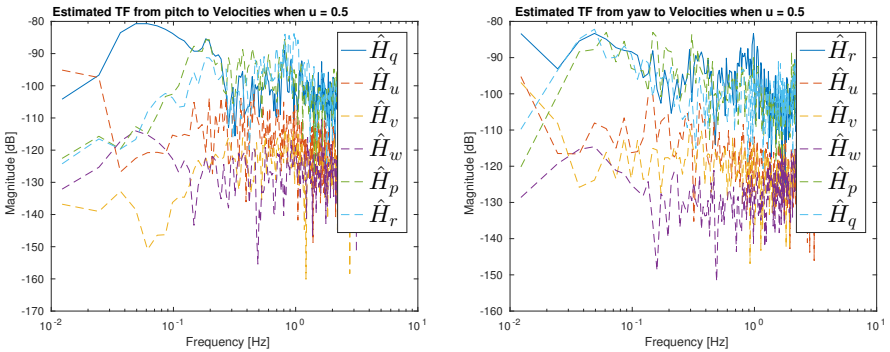

Figure 7.45 Figures showing TF for different input-output configurations when $u = 0.5$ knts.

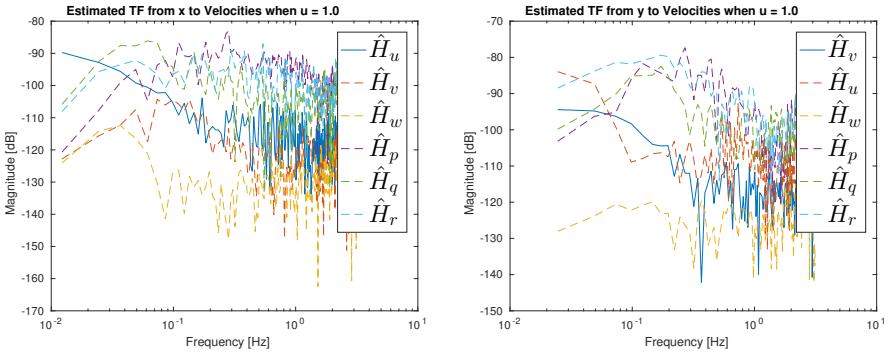

Figure 7.46 Figures showing TF for different input-output configurations when $u = 1.0$ knts.

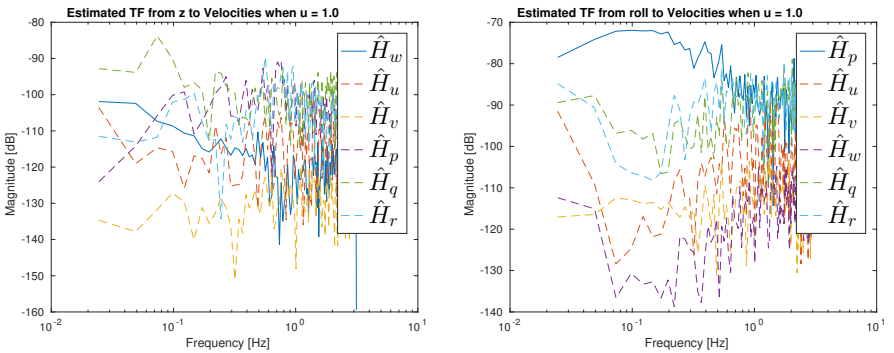

Figure 7.47 Figures showing TF for different input-output configurations when $u = 1.0$ knts.

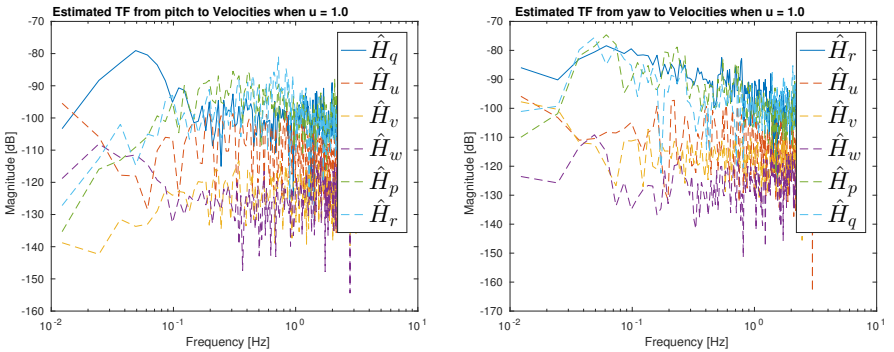

Figure 7.48 Figures showing TF for different input-output configurations when $u = 1.0$ knts.

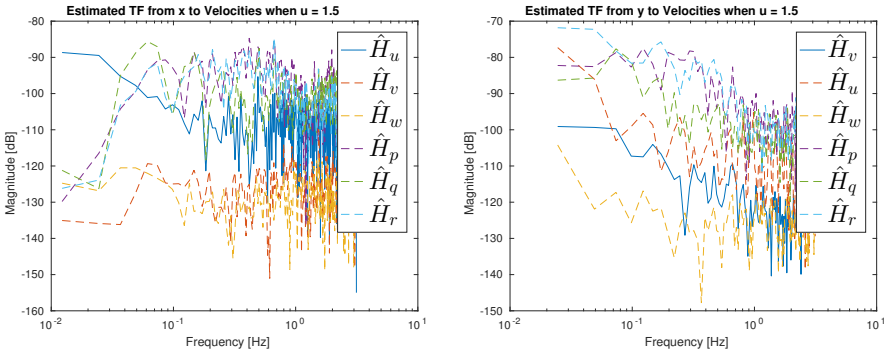

Figure 7.49 Figures showing TF for different input-output configurations when $u = 1.5$ knts.

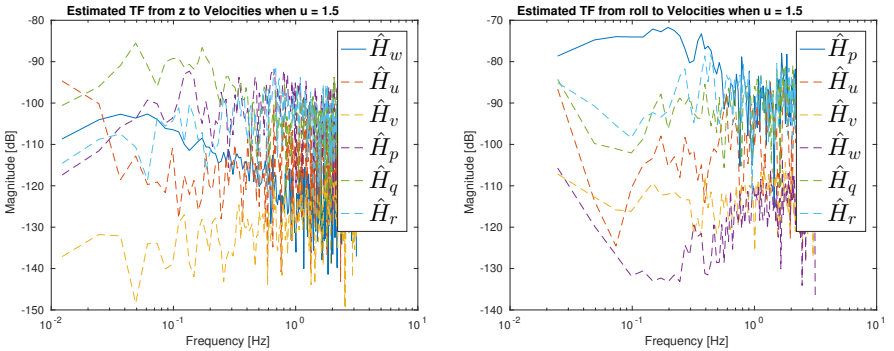

Figure 7.50 Figures showing TF for different input-output configurations when $u = 1.5$ knts.

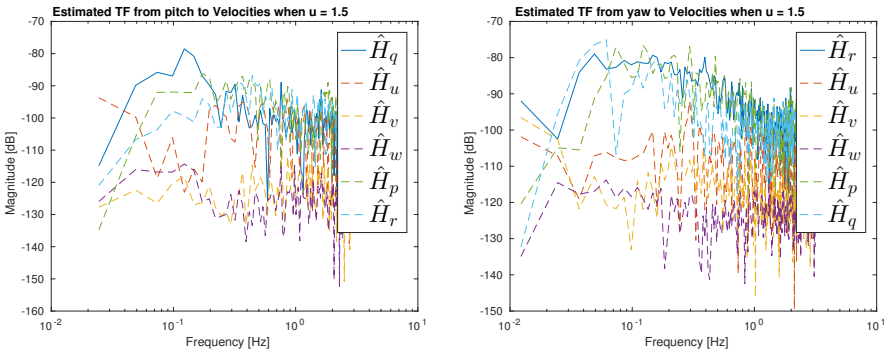

Figure 7.51 Figures showing TF for different input-output configurations when $u = 1.5$ knts.

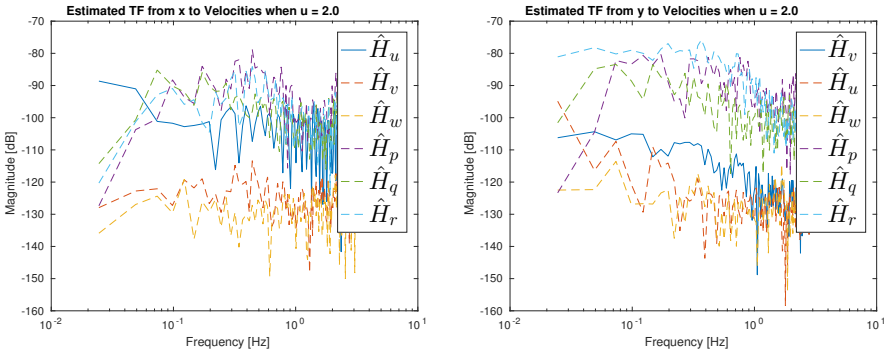

Figure 7.52 Figures showing TF for different input-output configurations when $u = 2.0$ knts.

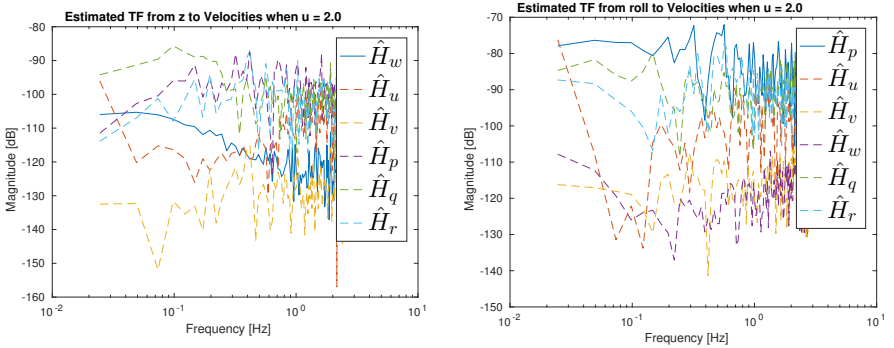

Figure 7.53 Figures showing TF for different input-output configurations when $u = 2.0$ knts.

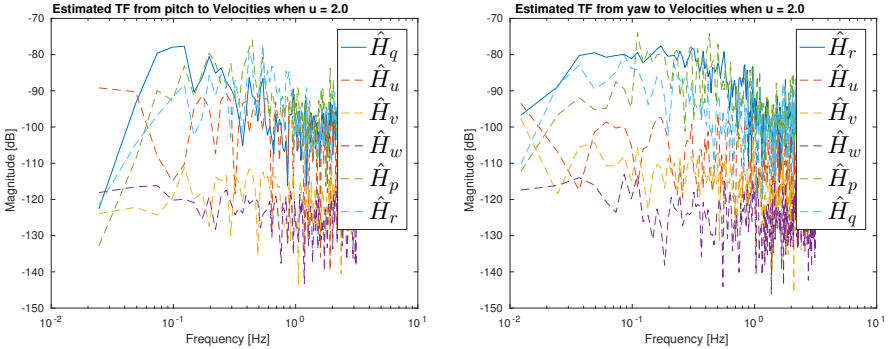

Figure 7.54 Figures showing TF for different input-output configurations when $u = 2.0$ knts.

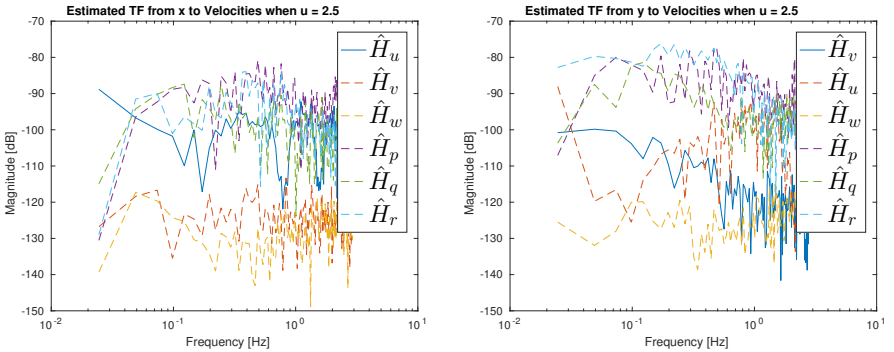

Figure 7.55 Figures showing TF for different input-output configurations when $u = 2.5$ knts.

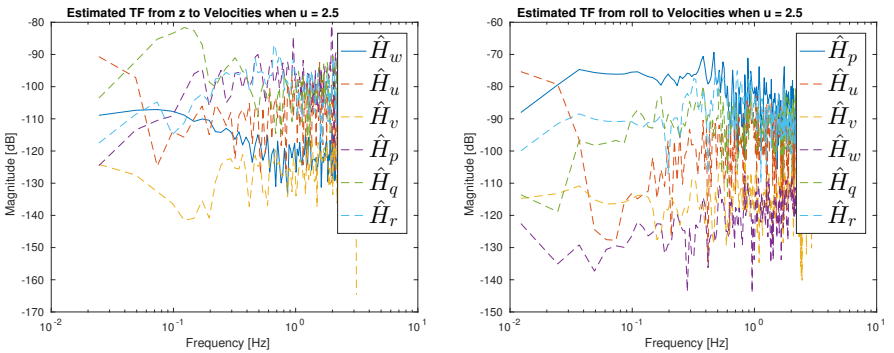

Figure 7.56 Figures showing TF for different input-output configurations when $u = 2.5$ knts.

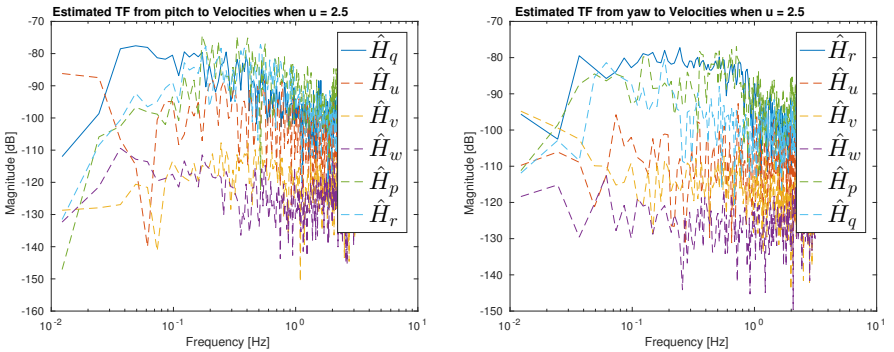

Figure 7.57 Figures showing TF for different input-output configurations when $u = 2.5$ knts.

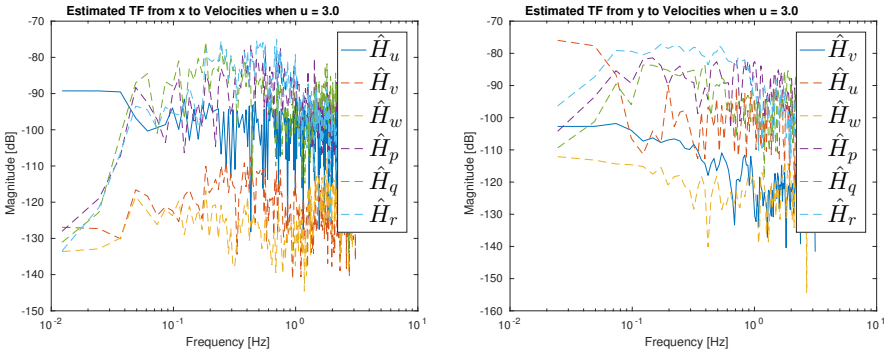

Figure 7.58 Figures showing TF for different input-output configurations when $u = 3.0$ knts.

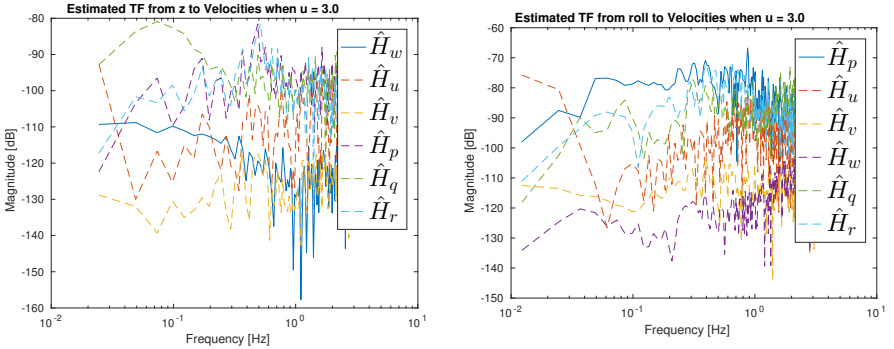

Figure 7.59 Figures showing TF for different input-output configurations when $u = 3.0$ knts.

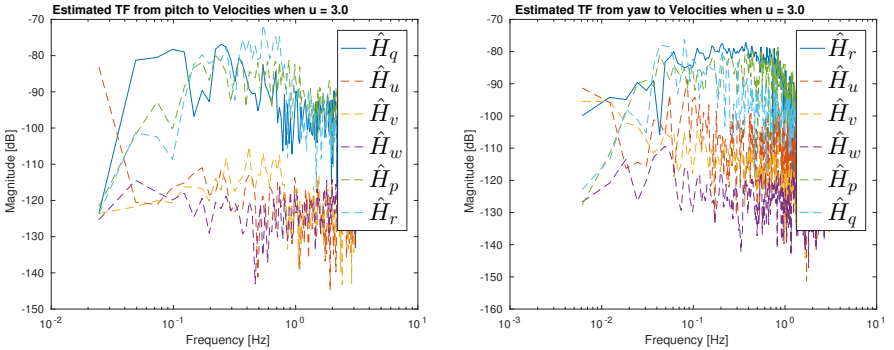

Figure 7.60 Figures showing TF for different input-output configurations when $u = 3.0$ knts.

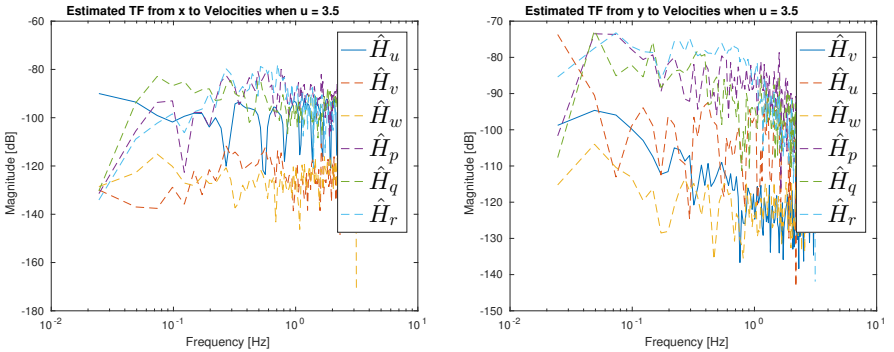

Figure 7.61 Figures showing TF for different input-output configurations when $u = 3.5$ knts.

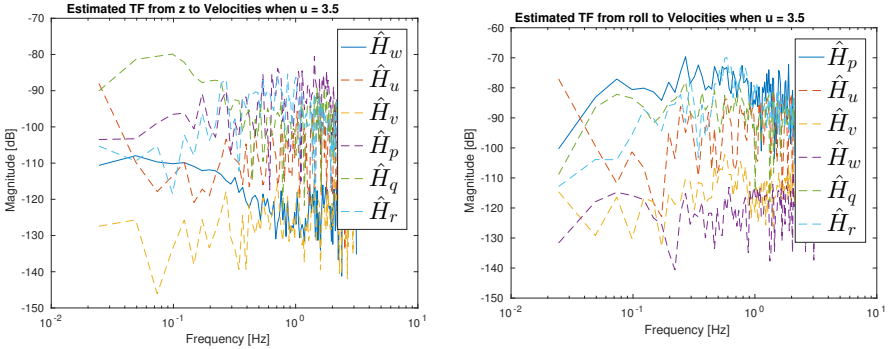

Figure 7.62 Figures showing TF for different input-output configurations when $u = 3.5$ knts.

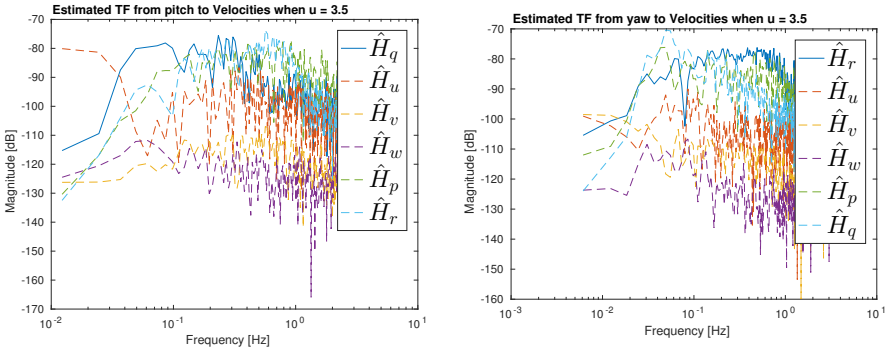

Figure 7.63 Figures showing TF for different input-output configurations when $u = 3.5$ knts.

Lund University
Department of Automatic Control
Box 118
SE-221 00 Lund Sweden

Document name
MASTER'S THESIS

Date of issue
April 2018

Document Number
TFRT-6049

Author(s)
Olle Ferling

Supervisor
Jonas Andersson, MMT Sweden AB
Rolf Johansson, Dept. of Automatic Control, Lund University, Sweden
Bo Bernhardsson, Dept. of Automatic Control, Lund University, Sweden (examiner)

Title and subtitle
Modeling, Analysis and Control of Underwater Vehicle SROV

Abstract

A new type of Remotely Operated Vehicle (ROV) has been designed by Marin Mätteknik (MMT) in cooperation with Reach Subsea and Kystdesign AS; the Surveyor ROV. Although MMT is successfully using the SROV in day-to-day operations, no mathematical model describing the system has previously been derived. In this thesis project, a mathematical model describing the SROV is developed through system identification techniques. Experiments to facilitate parameter estimation of the model are designed and consequently performed. The gathered data sets are investigated to determine how well they are suited for parameter estimation. Estimation of the continuous-time model parameters are carried out using a Kalman filter running on the input-output data obtained through the experiments. Comparisons between this method and results obtained through a subspace-based identification Matlab method are performed. Model validation is carried out using numerous performance measures. The thesis has shown that a coupled LPV model may be a feasible approach to the modeling problem, and also makes suggestions that could possiblyimprove on the results.
As an alternative to the current control system, simulations of closed-loop responses of the identified system model using a Model Predictive Control (MPC) structure are undertaken and presented. The simulations show that good performance is achievable using the MPC algorithm. Noticeably, the current control system has difficulties attenuating deviations from angular velocity set points. The MPC scheme has been shown to effectively suppress such control errors in simulations.

Keywords

Classification system and/or index terms (if any)

Supplementary bibliographical information

ISSN and key title
0280-5316

ISBN

Language
English

Number of pages
1-100

Recipient's notes

Security classification

http://www.control.lth.se/publications/